

584

LOW SPECIFIC IMPULSE ION ENGINE

BY

H. J. KING AND R. L. POESCHEL
HUGHES RESEARCH LABORATORIES

PREPARED FOR

NATIONAL AERONAUTICS AND SPACE ADMINISTRATION

CONTRACT NAS 3-11523

J. S. SOVEY, PROJECT MANAGER



FACILITY FORM 602

N70-28290
(ACCESSION NUMBER)

(THRU)

162
(PAGES)

(CODE)

CR-72677
(NASA CR OR TMX OR AD NUMBER)

28
(CATEGORY)



162 p8

NOTICE

This report was prepared as an account of Government-sponsored work. Neither the United States, nor the National Aeronautics and Space Administration (NASA), nor any person acting on behalf of NASA:

- A.) Makes any warranty or representation, expressed or implied, with respect to the accuracy, completeness, or usefulness of the information contained in this report, or that the use of any information, apparatus, method, or process disclosed in this report may not infringe privately-owned rights; or
- B.) Assumes any liabilities with respect to the use of, or for damages resulting from the use of, any information, apparatus, method or process disclosed in this report.

As used above, "person acting on behalf of NASA" includes any employee or contractor of NASA, or employee of such contractor, to the extent that such employee or contractor of NASA or employee of such contractor prepares, disseminates, or provides access to any information pursuant to his employment or contract with NASA, or his employment with such contractor.

NASA CR-72677

FINAL REPORT

LOW SPECIFIC IMPULSE ION ENGINE

by

H.J. King and R.L. Poeschel

HUGHES RESEARCH LABORATORIES
A Division of Hughes Aircraft Company
3011 Malibu Canyon Road
Malibu, California

prepared for

NATIONAL AERONAUTICS AND SPACE ADMINISTRATION

February 1970

CONTRACT NAS 3-11523

NASA Lewis Research Center
Cleveland, Ohio

J.S. Sovey, Project Manager

Details of illustrations in
this document may be better
studied on microfiche

PRECEDING PAGE BLANK NOT FILMED.

FOREWORD

The work described herein was done in the Ion Device Physics Department of the Research Laboratories of the Hughes Aircraft Company in Malibu, California. This department is managed by Mr. J.H. Molitor. The work was performed under Contract NAS 3-11523, managed by Mr. J.S. Sovey of NASA Lewis Research Center. Major technical contributors to this effort were:

H.J. King	Project Manager, ion optics design and evaluation
R.L. Poeschel	Assistant Project Manager, thruster optimization
S. Kami	mechanical design
J.W. Ward	thruster testing, analytical studies
C.R. Collett	thruster evaluation and life testing
W. Lent, L. Gates	ceramic coating development.

Preceding page blank

PRECEDING PAGE BLANK NOT FILMED.

TABLE OF CONTENTS

	LIST OF ILLUSTRATIONS	vii
	LIST OF TABLES	xi
	ABSTRACT	xiii
I.	SUMMARY	1
II.	INTRODUCTION	5
III.	THRUSTER DEVELOPMENT	7
	A. High Specific Impulse 30 cm Thruster	7
	B. Low Specific Impulse Optimization and Test	32
	C. Deliverable Hardware	114
IV.	SUMMARY OF RESULTS AND CONCLUSIONS	125
	REFERENCES	127
	APPENDIX	129

Preceding page blank

LIST OF ILLUSTRATIONS

Fig. 1.	2-1/2 kW low I_{sp} ion thruster.	10
Fig. 2.	Magnetic field plot showing critical field line	11
Fig. 3.	Effect of magnetic field shape on thruster performance	13
Fig. 4.	Field shapes with varying ratios of axial to radial magnets	15
Fig. 5.	Conceptual thruster model	17
Fig. 6.	Comparison of 30 cm thruster performance with scaled 15 cm values	19
Fig. 7.	Baffle configurations	20
Fig. 8.	HRL 30 cm thruster performance for two disc baffles and 0.63 cm thick conical baffle	21
Fig. 9.	Typical beam profiles taken on Task I thruster	23
Fig. 10.	Schematic of 30 cm Task I thruster	24
Fig. 11.	Circuit diagram	26
Fig. 12.	Measured depth of accel groove erosion in line with neutralizer axis	30
Fig. 13.	Comparison of experimental and computer calculated perveance with Child's law value	36
Fig. 14.	Perveance/hole requirements for 1.85 A beam from 30 cm thruster	38
Fig. 15.	Temperature distributions used for thermal buckling analysis.	41
Fig. 16.	Effect of support placement, no radial constraint, temperature profile "A".	41

Preceding page blank

Fig. 17.	Effect of electrode thickness; center support and at (0.1 cm dish) 22.5 cm	44
Fig. 18.	(a) Effect of initial shape on thermal distortion. (b) Effect of radial clamping on plate distortion	46
Fig. 19.	Experimentally measured thermal distortion of thin plate	49
Fig. 20.	Nomograph to estimate effect of charge exchange sputtering on electrode lifetime . . .	52
Fig. 21.	Perveance data for 15 cm conventional optics	53
Fig. 22.	30 cm high perveance conventional ion optics system	55
Fig. 23.	Perveance data for 15 cm insulated optics . . .	57
Fig. 24.	30 cm insulated ion optics design	63
Fig. 25.	Photographs of finished insulated ion optical system	65
Fig. 26.	Photograph of insulated ion optics after operation, showing plasma attachment	66
Fig. 27.	Perveance of 30 cm optics listed in Table VI	70
Fig. 28.	Discharge chamber performance with ion optical systems listed in Table VI	71
Fig. 29.	30 cm thruster configuration showing variable magnetic baffle geometry	75
Fig. 30.	Discharge chamber performance for several baffle and optic geometries	76
Fig. 31.	Tripod baffle mount for 30 cm diameter thruster	79
Fig. 32.	Comparison of discharge performance before and after installation of pre-formed baffle support and pole piece shaping ring . . .	80

Fig. 33.	Comparison of performance mappings for the 30 cm diameter variable magnetic baffle thruster and the optimized conventional baffle thruster	84
Fig. 34.	Comparison of performance mappings for thruster operation with 13 and 15 axial bar magnets and 8 radial bar magnets	85
Fig. 35.	Axial magnet field mapping for optimized magnetic configuration generated by 8 radial and 15 axial permanent magnets	86
Fig. 36.	30 cm diameter thruster optimized for operation at 2.5 kW power, 2750 sec specific impulse	88
Fig. 37.	Schematic diagram of diode configuration for hollow cathode tests	90
Fig. 38.	Cathode configurations	91
Fig. 39.	Cathode tip cross sections synthesized from plastic moldings	91
Fig. 40.	Profiles of hollow cathode orifice before and after 500 hours of testing	94
Fig. 41.	Initial electrical test system schematic	99
Fig. 42.	Electrical test system schematic showing modification required for stabilization during Task II 100 hour test	101
Fig. 43.	Electrical test system schematic showing modifications used for Task III and IV testing	102
Fig. 44.	Comparison of performance mapping for several stages of thruster development	106
Fig. 45.	Variable power operation characteristics for the 30 cm thruster chamber developed under this program	107
Fig. 46.	Probe configuration for measuring ion beam profiles	107

Fig. 47.	Beam profile 2.5 cm downstream of accel electrode.	108
Fig. 48.	Beam profile 1.52 cm downstream of accel electrode.	108
Fig. 49.	Effect of ion sputtering of insulating coating.	112
Fig. 50.	Task I 30 cm thruster delivered under contract	115
Fig. 51.	Task I 30 cm thruster delivered under contract	117
Fig. 52.	Task I 30 cm thruster delivered under contract	118
Fig. 53.	Task V 30 cm thruster delivered under contract	119
Fig. 54.	Task V 30 cm thruster delivered under contract	121
Fig. 55.	Task V 30 cm thruster delivered under contract	122
Fig. A-1.	Schematic of voltage breakdown test	138
Fig. A-2.	One layer of refractory subcoat viewed from back of grid.	143
Fig. A-3.	Grid coated with three layers of fused refractory subcoat	143
Fig. A-4.	Three fired refractory subcoats after filler glass fusion	144
Fig. A-5.	Surface of complete coating system after firing of MC-1 surface glass coating	144
Fig. A-6.	Cross section of grid web showing coating system contour	145

LIST OF TABLES

I.	Thruster Performance for each Task.	2
II.	Performance Summary	29
III.	Summary of Support Configurations	42
IV.	Change in Shell Depth for Different Initial Depths.	43
V.	Change in Shell Depth for Different Radial Constraints (0.125 cm thick; Center and Edge Support Temperature Profile "A").	45
VI.	Summary of Ion Optical System Per- formance.	69
VII.	Thruster Parameters for Figure 30	77
VIII.	Data for Figure 33.	82
IX.	Cathode Tests with Variations on Cath- ode Configuration	93
X.	Neutralizer Variations and Results.	96
XI.	Comparison of Representative Thruster Parameters for Tasks II, III, and IV.	105
XII.	Task IV 500 Hour Test Performance Summary	109
XIII.	Specifications for Deliverable Hardware	123
A-1.	Results of Metal Preparation Studies with MC-1 Glass	133
A-2.	Results of Commercial Glass Evaluation Using the Induction Furnace	135
A-3.	Optimum Firing Schedules for Selected Commercial Glasses on Molybdenum	137
A-4.	Effect of Mullite Substitutions in Re- fractory Subcoating	140
A-5.	Results of Coating System Study	141

ABSTRACT

A 30 cm diameter hollow cathode, mercury electron bombardment ion thruster meeting the general specifications required for prime solar electric propulsion has been developed and tested. The 2.5 kW module operates at an electrical efficiency of 77%, with a mass utilization of 90% (including the plasma bridge neutralizer) at a specific impulse of 2750 sec. The nominal thrust level is 27 mlb.

SECTION I

SUMMARY

This summary is organized along the same format as the tasks of the contract so that the contract goals and achievements may be directly related. The following sections of the report treat individual technological areas such as ion optical systems, discharge chamber, neutralizer development, etc.; effort was expended in many of these areas under several tasks throughout the contract period.

Task I involved the design and test of a 30 cm hollow cathode mercury thruster patterned generally after the 15 cm SERT-II design. Following demonstration of performance by a 100 hour test, two units identical to those tested were to be delivered to NASA LeRC for evaluation. The nominal characteristics set forth under this task, compared with those actually measured in the 100 hour test, are given in Table I.

The two thrusters built under this task were delivered to NASA in August 1969, along with the necessary quality control history record.

Task II had as a goal the design, fabrication, and test of at least two ion optical systems which would permit the scaled discharge chamber produced under Task I to be operated at 2.5 kW input power at a specific impulse of 2750 sec. This requires a beam current of 1.85 A at a set acceleration voltage of 1000 V. After an extensive analysis and design program, which included testing of prototype hardware on a 15 cm thruster, both a conventional two-grid ion optical system and an insulated electrode system were constructed in 30 cm size. Following a comparison of discharge chamber performance and perveance of each system, the insulated optic was selected for further development. The performance of the system during the 78 hour design verification test is shown in Table I.

Task III required that the performance of the system created by the coupling of the Task I 30 cm discharge chamber and the Task II low specific impulse ion optics be optimized to the levels specified in Table I. This required parametric studies of the discharge chamber and plasma bridge neutralizer, plus modification of the power conditioning and control circuitry to stabilize operation. The results of this optimization are presented in Table I. This test point was maintained for 71 hours, at which point the electrode would no

TABLE I
Thruster Performance for Each Task

	High Isp Thruster		L	
	Goals	Task I Test	Goals	2
Input Power, kW	3.5	3.43	2.5	
Electrical Efficiency, %	85	88.1	74	
Propellant Efficiency, %	85	82.2	87	
Over-All Efficiency, %	72	72.5	64	
Effective Specific Impulse, sec	4550	4500	2750	2
Acceleration Voltage, kV	3.0	3.0	1.0	
Thrust, lb	0.025	0.025	0.025	
Weight, lb	< 20	~ 14	< 20	

longer sustain the full acceleration voltage. This was attributed at least in part to a period of excessive arcing in the neutralizer wiring external to the thruster, which required that the test be stopped at the 57 hour point and the thruster removed from the vacuum.

Task IV was a 500 hour design verification test of the Task III thruster. As shown in Table I, minor discharge chamber modifications resulted in some improvement over the Task III thruster. This test, which was completed on schedule, verified the performance and lifetime of the hollow cathode and isolator. As a result of mechanical failure of the insulated electrodes after approximately 200 hours of operation, it was necessary to conduct the test in three segments. This is discussed in detail in the body of the report. As shown in Table I, all electrical performance goals set by the contract were exceeded during this test.

Task V was to fabricate and deliver two thrusters of the design used for the 500 hour Task IV test. This was completed by the end of the contract period. As specified in Task VI, the necessary quality control and reliability functions were performed and documents were prepared to assure that the deliverable hardware could be reproduced as required.

PRECEDING PAGE BLANK NOT FILMED.

SECTION II

INTRODUCTION

Several factors led to the work covered in this report. The first was the development and impending flight of SERT-II, a 15 cm hollow cathode mercury thruster.¹ This program, which was carried out at the NASA Lewis Research Center, produced a highly efficient ion thruster whose performance was thoroughly documented parametrically. This information was supplemented by a study contract at HRL² under which the discharge chamber was probed to determine the plasma characteristics. A discharge chamber model and set of scaling laws were then evolved. Finally, a number of mission analyses and system design studies were conducted³ which indicated that the most desirable thruster module was a 2.5 kW unit which would operate efficiently at approximately 2750 sec specific impulse. These three factors led naturally to the award of a contract to scale the SERT-II thruster to 2.5 kW at the desired specific impulse. A related effort at NASA LeRC has permitted a most useful exchange of information between the two groups during this program.

The scope of the work reported here was summarized in Section I. The effort has clearly demonstrated that the electrical parameters upon which the mission analyses were based can be achieved and in fact exceeded, and that the erosion of the hollow cathode is negligible. The hollow cathode plasma bridge neutralizer appears to introduce no serious accelerator erosion in the final design tested. The mercury vapor isolator performed without difficulty during all tests in which it was used, including the final 500 hour Test. The one major design goal that was not met was the demonstration of ion optical system lifetime compatible with proposed missions. Further work in this area is required, along with the development of a control system and verification that the mechanical design is flightworthy.

Because the desired design parameters were well known at the beginning of the current effort and this program was carefully tailored to include them, the current results are particularly relevant to the field of primary electric propulsion.

Preceding page blank

PRECEDING PAGE BLANK NOT FILMED.

SECTION III

THRUSTER DEVELOPMENT

A. HIGH SPECIFIC IMPULSE 30 CM THRUSTER

As outlined above, the program to develop a 30 cm thruster of nominal SERT-II design that will operate efficiently at a lower (2750 sec) specific impulse was approached in two steps. This section deals with scaling the 15 cm diameter SERT-II thruster to 30 cm without attempting to change the ion optical design from that used for SERT-II.

	<u>Screen</u>	<u>Accel</u>
Hole	0.40 cm (0.157 in.)	0.32 cm (0.128 in.)
Center-to-center spacing	0.45 cm (0.177 in.)	0.45 cm (0.117 in.)
Open area	72%	47%
Thickness	0.076 cm (0.030 in.)	0.25 cm (0.100 in.)

1. Discharge Chamber Scaling

a. Scaling Laws

A relatively comprehensive understanding of oxide cathode thruster discharge chamber operation was developed under a previous NASA supported study.⁴ The basic scaling laws derived from the discharge model developed under the above mentioned study have been applied to the design of a larger thruster which will operate at high efficiency. In order to preserve the performance characteristics of the 15 cm unit which served as the basis for the scaling study, the following criteria were applied:

1. The electron energy (discharge voltage) must not increase with thruster size.
2. The extracted ion current density (plasma density) should remain constant to permit the use of existing ion optical designs.

3. The propellant utilization should be independent of thruster size (therefore, the rate at which neutrals are ionized as they traverse the discharge chamber must be independent of thruster size).
4. The energy losses in the discharge per extracted ion (eV/ion) also should be independent of thruster size.

Because the extracted ion current increases with the square of the thruster diameter, and the current density and discharge voltage must both remain constant, the discharge current must also vary as the square of the thruster diameter. The resultant scaled thruster is predicted to have these properties if the discharge plasma length (discharge chamber length) is kept constant and if the product of the magnetic field strength and discharge chamber diameter is also held constant. In addition, the features of the SERT-II design which are considered essential to good performance can be summarized in the following design guidelines.

1. The magnetic field must be so shaped that "critical field lines" which originate close to the location on the cathode housing where electrons are injected into the discharge must extend to near the outer edge of the screen electrode.
2. The anode must be so located that it remains at a distance of at least one electron cyclotron diameter from the critical field lines.
3. The average plasma length, which is independent of thruster diameter, should be about 7 to 10 cm. Therefore the thruster length need not be increased over the 15 cm value.
4. The opening between the hollow cathode housing and the baffle must be so restrictive that discharge potentials on the order of 35 to 40 V are required to draw the required electron currents from the hollow cathode.
5. The ion optical system must possess a high transmission (on the order of 70%).

The coupling between the hollow cathode and the discharge plasma is known to depend critically on the cathode magnetic pole piece and baffle configuration. Unfortunately, the details of this coupling and its consequent effect on discharge performance were not understood sufficiently to permit a guideline for scaling the cathode pole-baffle structure; therefore, they had to be determined empirically, as described below.

The thruster designed in accordance with the above criteria is shown in Fig. 1. The construction techniques were intended to provide maximum flexibility for interchanging component parts to facilitate optimization. The thruster, which weighs 10 lb, is formed primarily from 0.02 cm stainless steel with 0.1 cm soft iron magnetic poles.

b. Magnetic Field

The shape and intensity of the magnetic field in the discharge chamber control the efficiency and stability of the thruster, as well as the radial plasma density and hence the ion beam profile. Figure 2 shows the intensity of the axial magnetic field at various locations in the discharge chamber of the SERT-II thruster, as well as the shape of the magnetic field lines determined by an iron filing magnetic field map. Note in particular the "critical field line" which leaves the tip of the anode near the screen electrode and crosses the discharge chamber to the cathode pole tip at a point very near the point where the electrons emerge between the pole tip and the baffle. Once electrons reach this critical field line, they are collected by the anode on their next traversal of the discharge chamber. As the distance between the point at which the electrons enter the discharge chamber and the critical field line and the strength of the magnetic field in this region increase, the discharge chamber impedance increases. Excessively high impedance forces the discharge voltage above the desired value or causes unstable discharge chamber performance.

Field line A of Fig. 3 shows the critical field line obtained by simply increasing the radius of a SERT-II thruster as suggested by the scaling relationships. Note that it does not follow the desired path between screen and cathode pole pieces. Thus the scaling requirements of a fixed discharge voltage, a magnetic field strength which varies inversely as the radius, and a discharge current which increases as the

M 7055

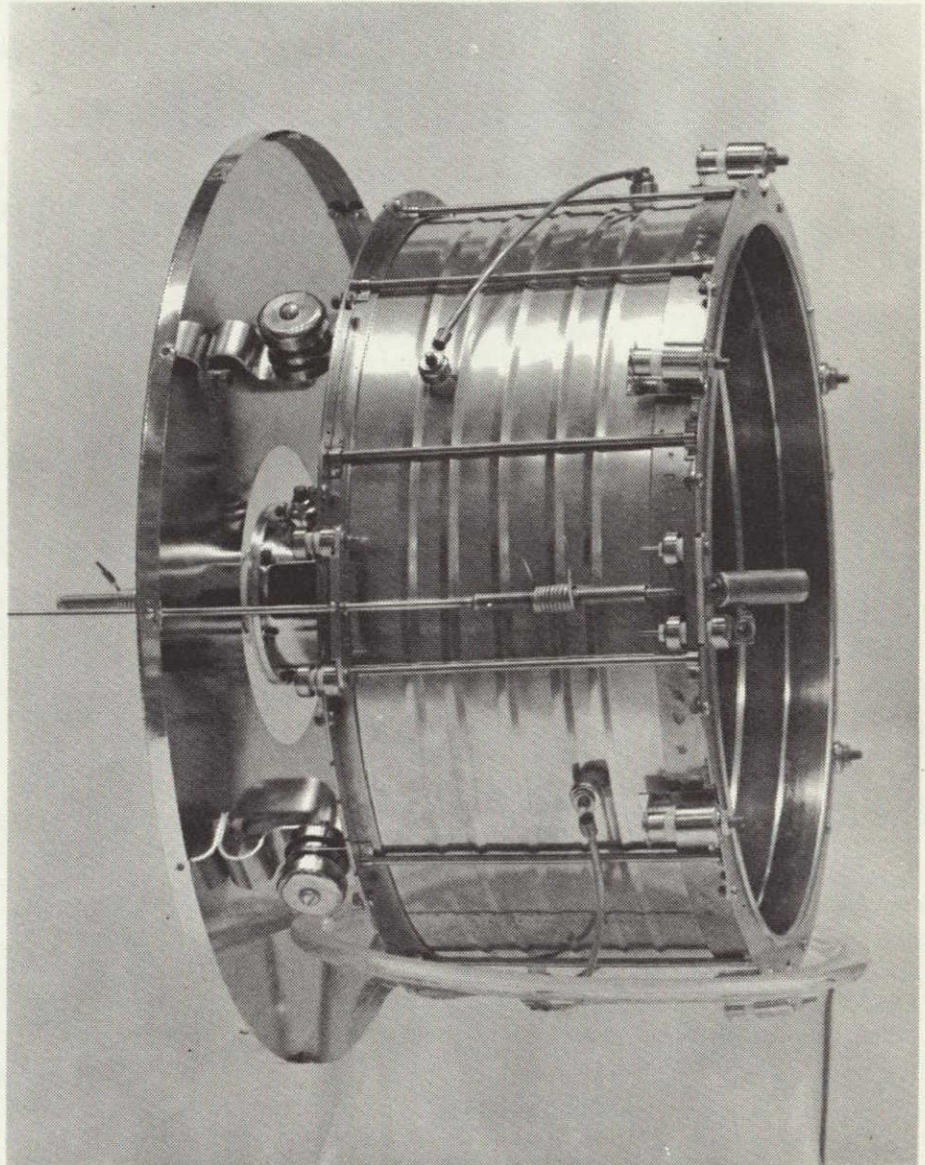


Fig. 1. 2-1/2 kW low I_{sp} ion thruster.

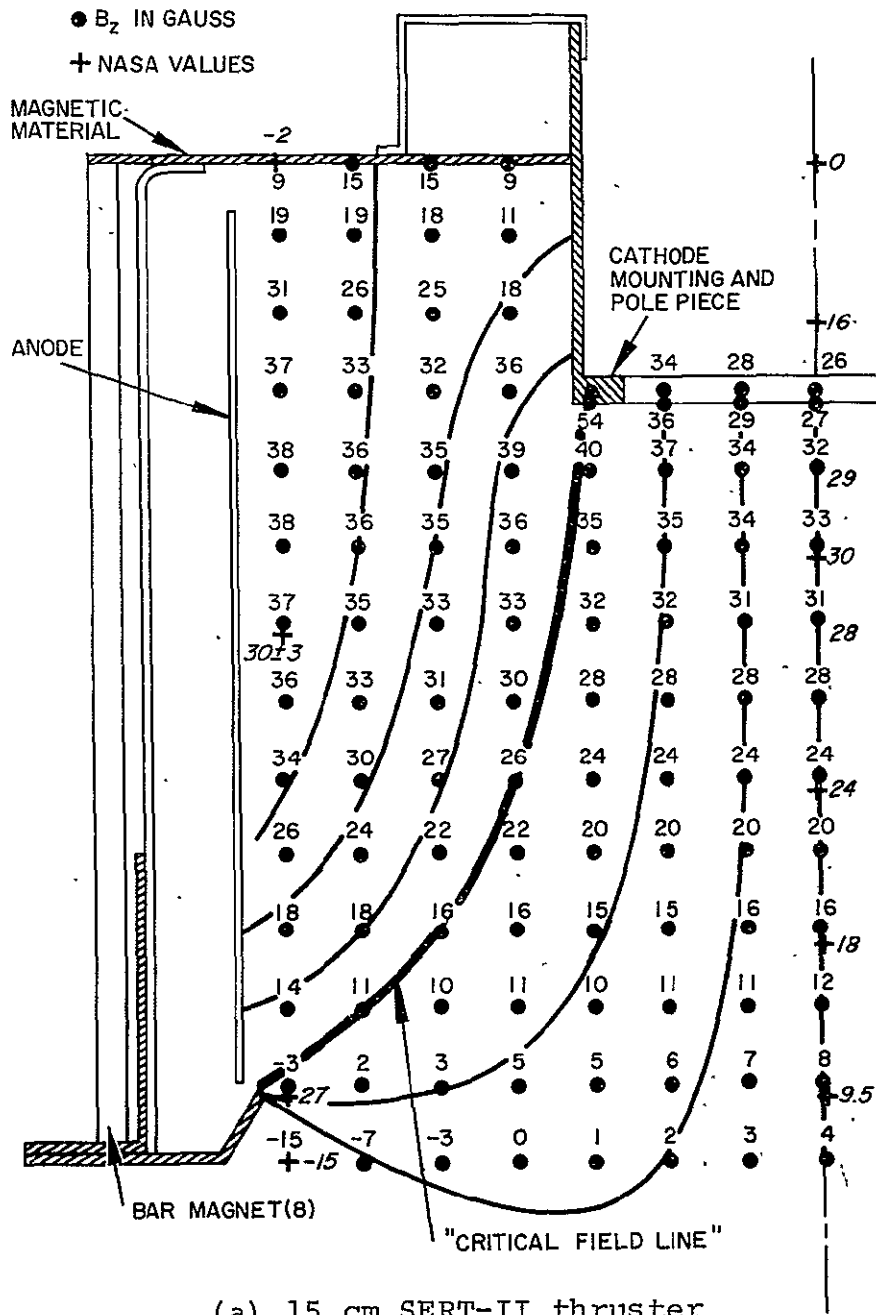
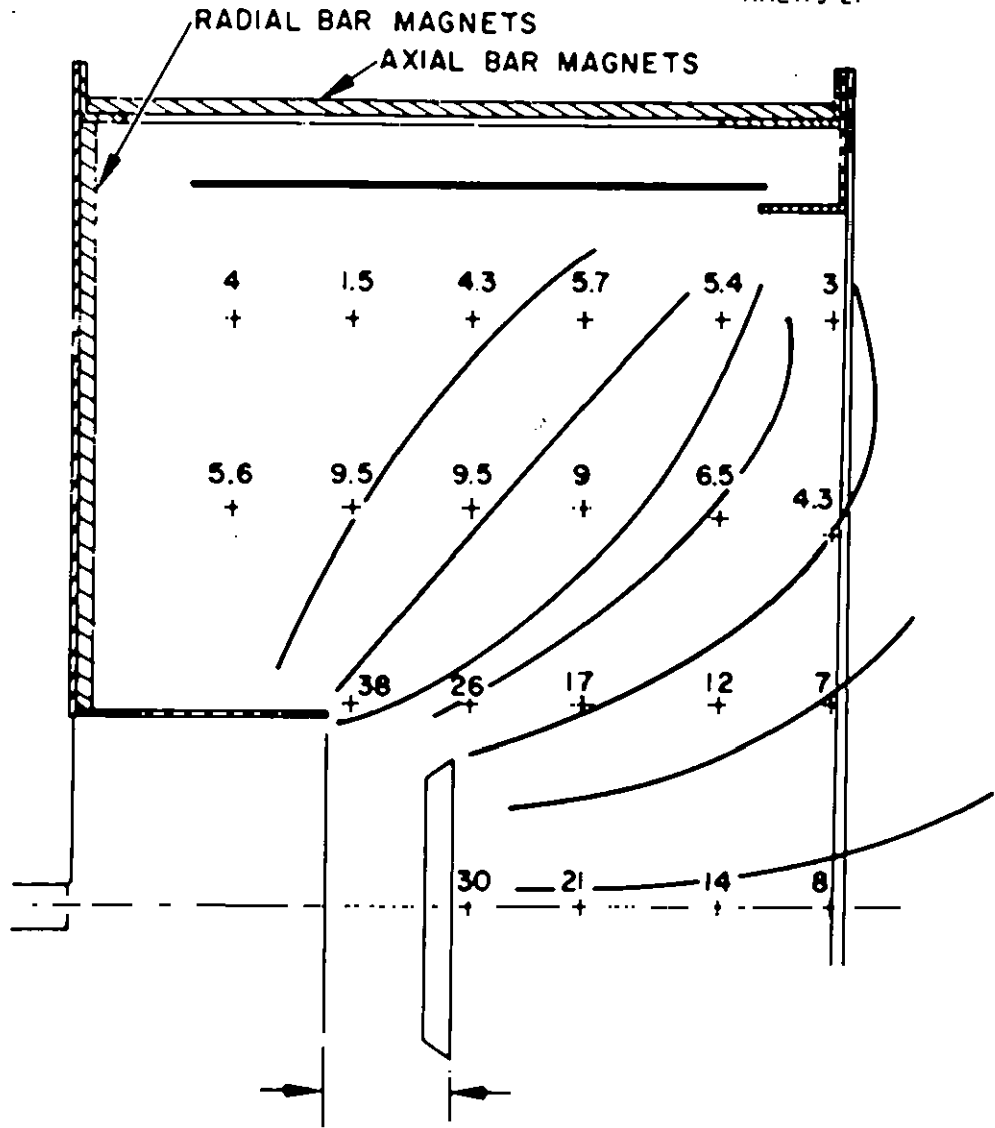
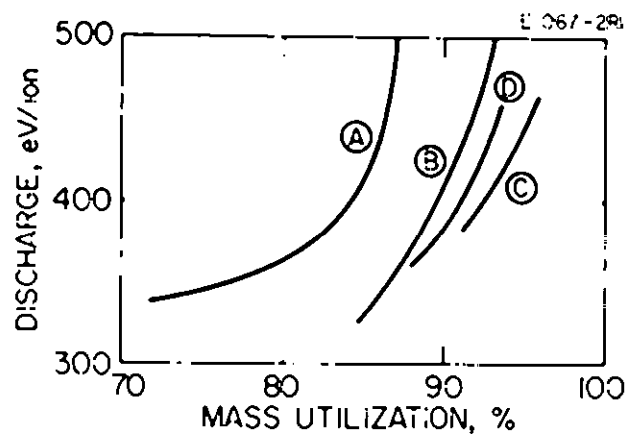
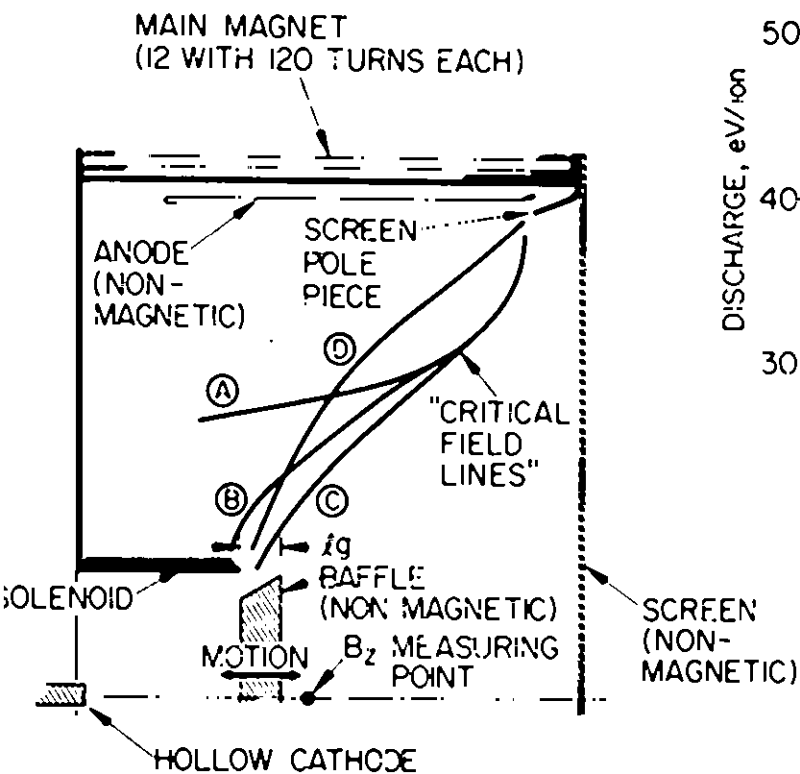


Fig. 2. Magnetic field plot showing critical field line.



(b) 30 cm thruster

Fig. 2. (continued).



CRITICAL FIELD LINE	AMPERE TURNS		B_z gauss
	SOLENOID	MAIN	
A	0	2880	4.5
B	100	2880	7.5
C	200	2880	13
D	200	1440	10

Fig. 3. Effect of magnetic field shape on thruster performance.

square of the radius cannot be achieved simultaneously with this configuration. The screen pole piece and collar, the cathode pole piece, and the baffle were all modified in both size and shape in order to improve the performance. After this series of experiments, typical performance was mass utilization of 75 to 80% at 350 eV/ion. Stable operation could not be maintained at magnetic fields greater than one quarter the scaled SERT-II value.

At this point it was decided that a basic change in the magnetic circuit was required, and a solenoid was wrapped around the cathode pole piece. Proper choice of the polarity of this solenoid with respect to the main discharge chamber field makes it possible to adjust the divergence of the magnetic field lines over a wide range. This is best shown in Fig. 3, where the shape of the critical field line is shown for several different current ratios in the main and solenoidal fields. Note in particular that the position of the critical field line may be moved from a position 5 cm outside the cathode pole piece to a point inside the pole, and that it may be pulled away from the screen electrode. The shape of the field lines does not change as the field intensity is varied, provided the ratio of the solenoid to main magnet currents is unchanged (because all parts of the magnetic circuit are designed not to saturate). With this additional variable it is now possible to optimize the thruster performance during operation by choosing the magnetic field shape as well as the intensity which gives the best performance.* One such set of data is presented in Fig. 3, which shows the thruster performance for different magnetic field shapes.

Because the final design was to be implemented with permanent magnets, a series of tests were conducted to establish the shape of the critical field line with various combinations of radial and axial bar magnets, as shown in Fig. 4. The radial magnets had a cross section of 0.35 cm by 0.94 cm, while the axial magnets were 0.70 cm square. As seen in Fig. 4, the combination of 8 axial and 12 radial magnets gives a critical field line very close to the optimum value shown in Fig. 3. While the above provided the proper field shape, the field strength was greater than desired for the best discharge chamber performance. The final design shown in Fig. 2(a) employs 8 radial magnets of the size listed above, plus 12 axial magnets of 0.35 cm diameter.

* This technique for thruster optimization was developed under Contract NAS 3-11523, NASA-Lewis Research Center.

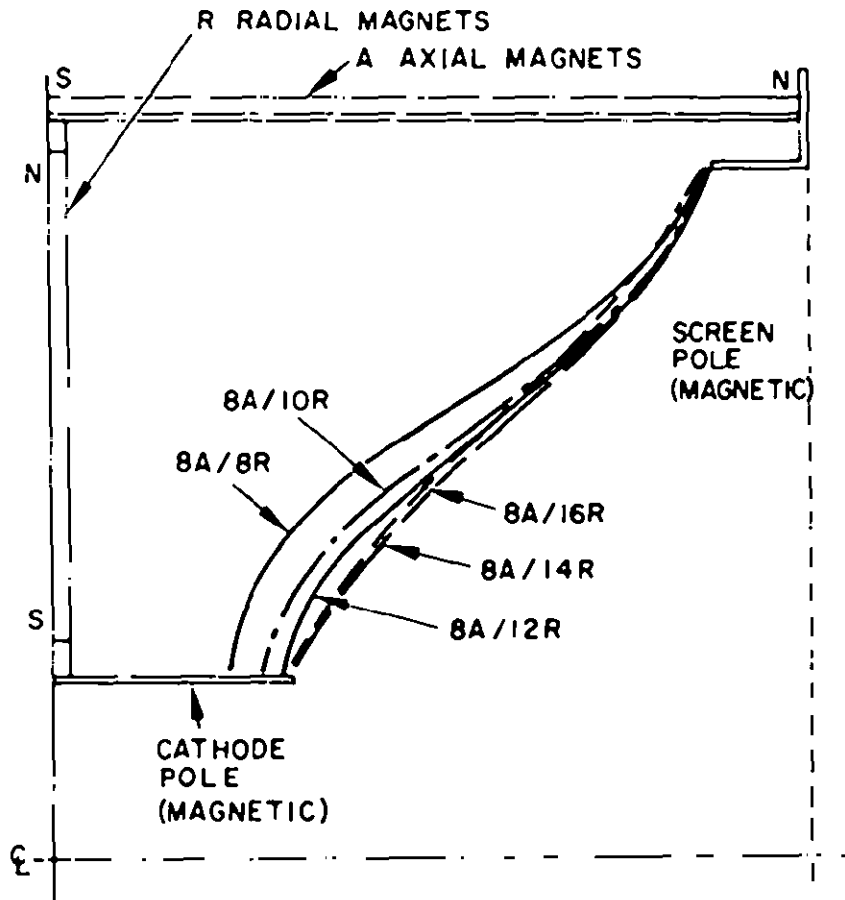


Fig. 4. Field shapes with varying ratios of axial to radial magnets.

c. Discharge Chamber Length-to-Diameter Ratio

The scaling laws indicate that the actual length of the discharge chamber, rather than the ratio of length to diameter, is the important parameter. As a result, the 30 cm diameter chamber was constructed with the same nominal length as the 15 cm SERT-II discharge chamber. Because the desired performance was achieved with this configuration, the chamber length was not varied. It is possible that scaling to diameters greater than 30 cm might require some increase in length to achieve the desired magnetic field shape.

d. Discharge Voltage

For an acceptable thruster design the discharge voltage must lie within a relatively narrow range. If it is too low the ionization efficiency suffers; if it is too high the cathode lifetime may be too short. Figure 5 is a conceptual thruster model which illustrates where voltage drops occur in the discharge chamber. There is a cathode sheath of approximately 10 V between the plasma immediately in front of the cathode and the cathode itself. Next there is a large voltage drop between the cathode plasma and the main discharge plasma which floats a few volts above anode potential. It is apparent that in order to design for a particular discharge voltage, it is necessary to control the voltage drop across the plasma sheath which separates the cathode and main discharge plasmas (i.e., the sheath in the baffle region). This voltage drop, which is nominally 25 V, is primarily a function of three variables.

The first is the neutral density. A relatively high neutral pressure in the baffle region lowers the discharge voltage (for a given discharge current) because the baffle is not as effective in restricting the flow of electrons from the hollow cathode plasma to the main discharge plasma when the neutral or plasma density is increased within the baffle-pole piece enclosure. Hence, more electrons can be drawn through the open area around the baffle for a given voltage. Furthermore, more ionization occurs directly downstream from the baffle, and the resultant low energy electrons diffuse more readily across field lines than do the primaries (which are accelerated through the baffle-pole gap). This neutral density is controlled primarily by the flow through the hollow cathode, and may thus be adjusted only over a range determined by the limits of the cathode operation.

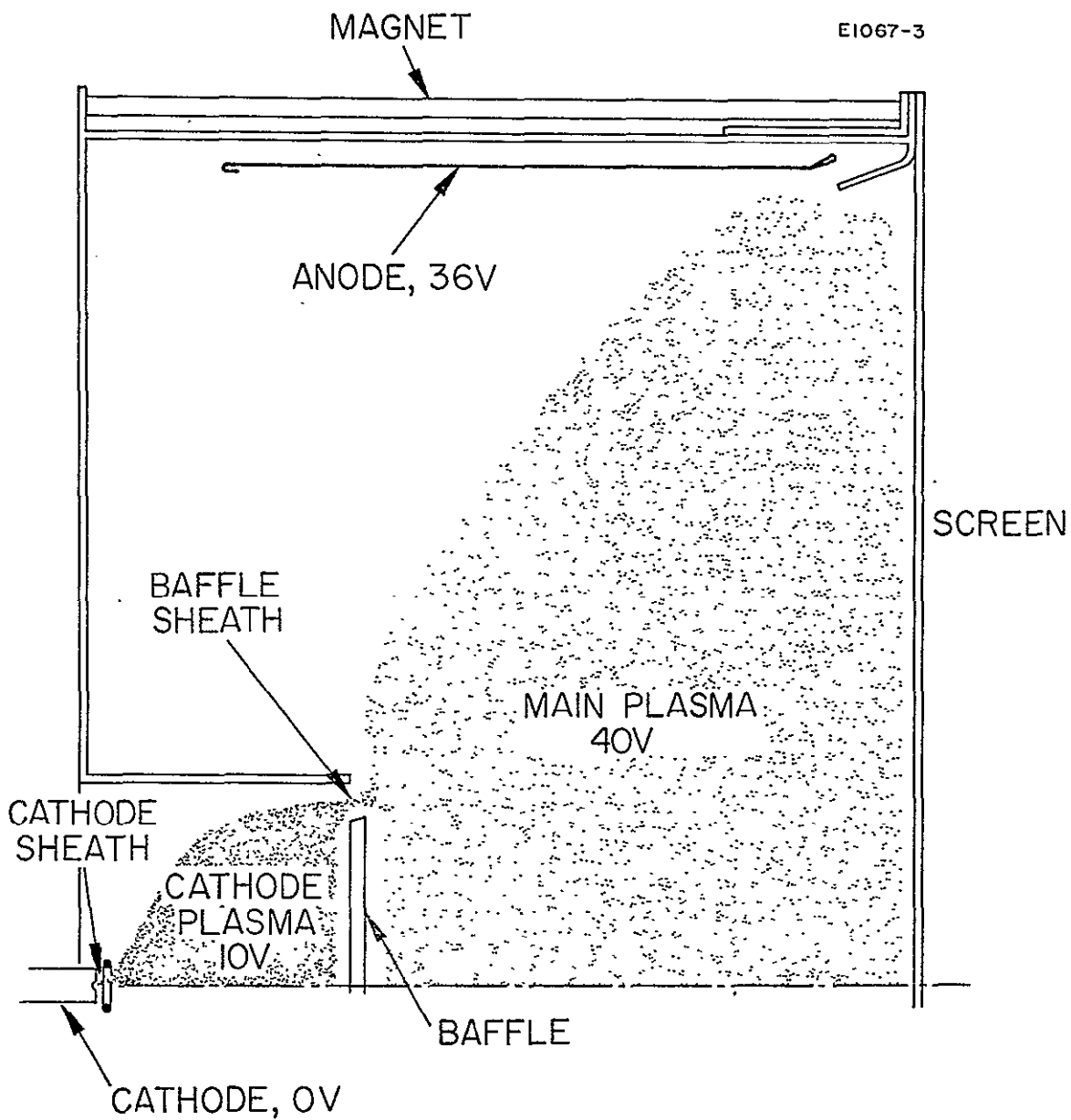


Fig. 5. Conceptual thruster model.

The second variable is the strength and shape of the magnetic field in the aperture between the baffle and the pole piece. A strong field transverse to the direction in which the electrons must diffuse provides a high impedance, thus increasing the voltage drop for a given discharge current. Some adjustment is possible, but it must be consistent with the general shape of the magnetic field within the main discharge chamber required for good thruster performance.

The third variable is the physical size and shape of the aperture between the baffle and the pole tip. This gap may be used to adjust the rate at which both electrons and neutrals pass from inside the pole piece to the main discharge chamber.

In order to examine the effect of the gap width, a conical baffle was fabricated and installed in the discharge chamber (Fig. 3) in such a manner that it could be moved axially back and forth while the thruster was operating. Because of the angle of the cone, this motion opened or closed the gap.

The data shown in Fig. 6 were taken with this arrangement. The 30 cm thruster was operated at a beam current of 1 A, which is four times SERT-II beam current. The propellant efficiency during the run was 83.5%. The data demonstrate how the critical variables behave as the baffle is repositioned to modify the discharge conditions. At a baffle position of 2.2 cm all the variables are in the range of the SERT-II values,* indicating the validity of the scaling relationships and the design procedures.

2. Discharge Chamber Performance

a. Performance Mapping

As discussed above, the discharge parameters were first adjusted with the movable conical baffle shown in Fig. 7(a). Dual feed systems and vaporizers were used for supplying propellant separately to the hollow cathode and to the discharge chamber, to provide separate flow control. It was found, however, that although the performance was satisfactory, the discharge could not be ignited while this baffle

* As reported in Ref. 5, for an early SERT-II configuration.

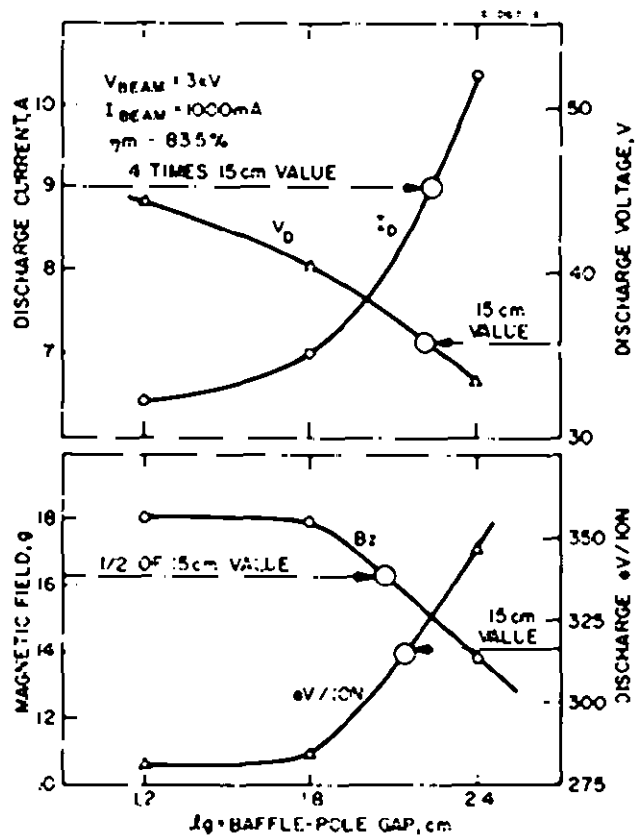


Fig. 6. Comparison of 30 cm thruster performance with scaled 15 cm values.

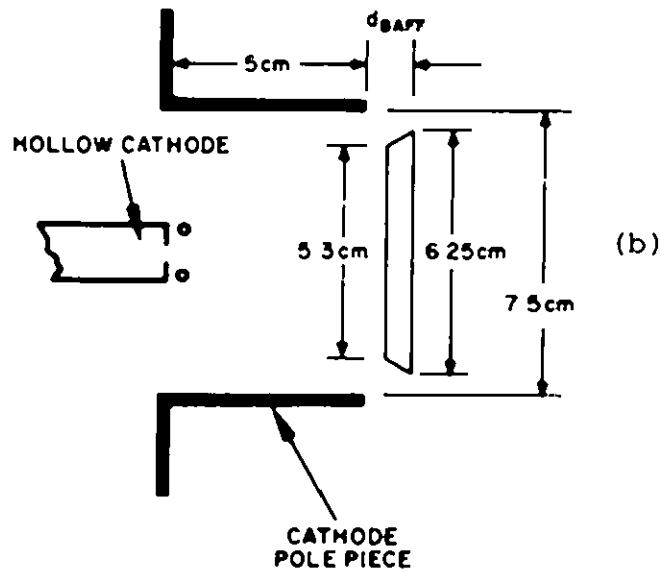
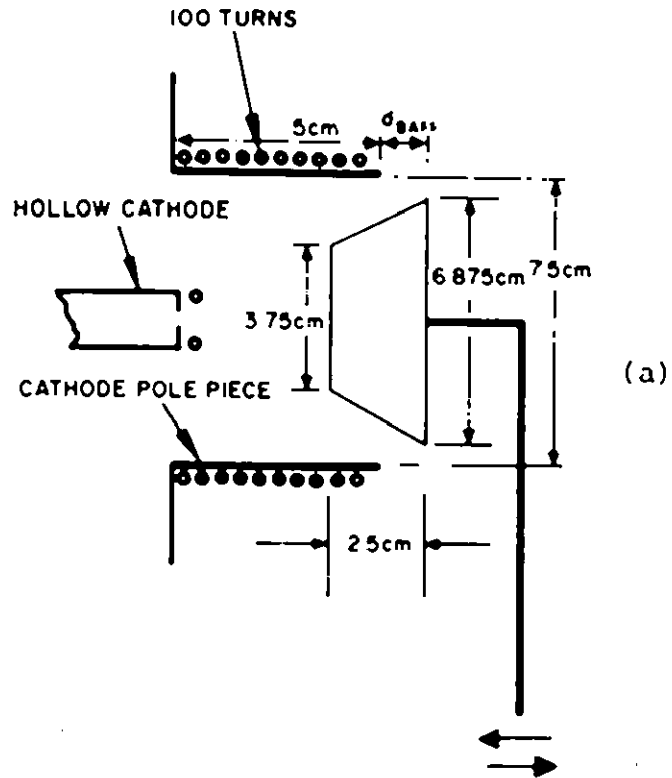


Fig. 7. Baffle configuration.

was in its optimum location because of the complete electrostatic shielding of the cathode from the anode voltage. Movable disc 5.4 and 4.5 cm baffles were substituted for the conical baffle. The ignition problem was eliminated, but the performance was not as good as with the conical baffle, as shown in Fig. 8. Finally the thinner conical baffle shown in Fig. 7(b) was substituted as a compromise. The performance with this final configuration, which was used in the 100 hour system test, is also shown in Fig. 8. Permanent magnets were then substituted for the axial solenoids with little, if any, change in performance.

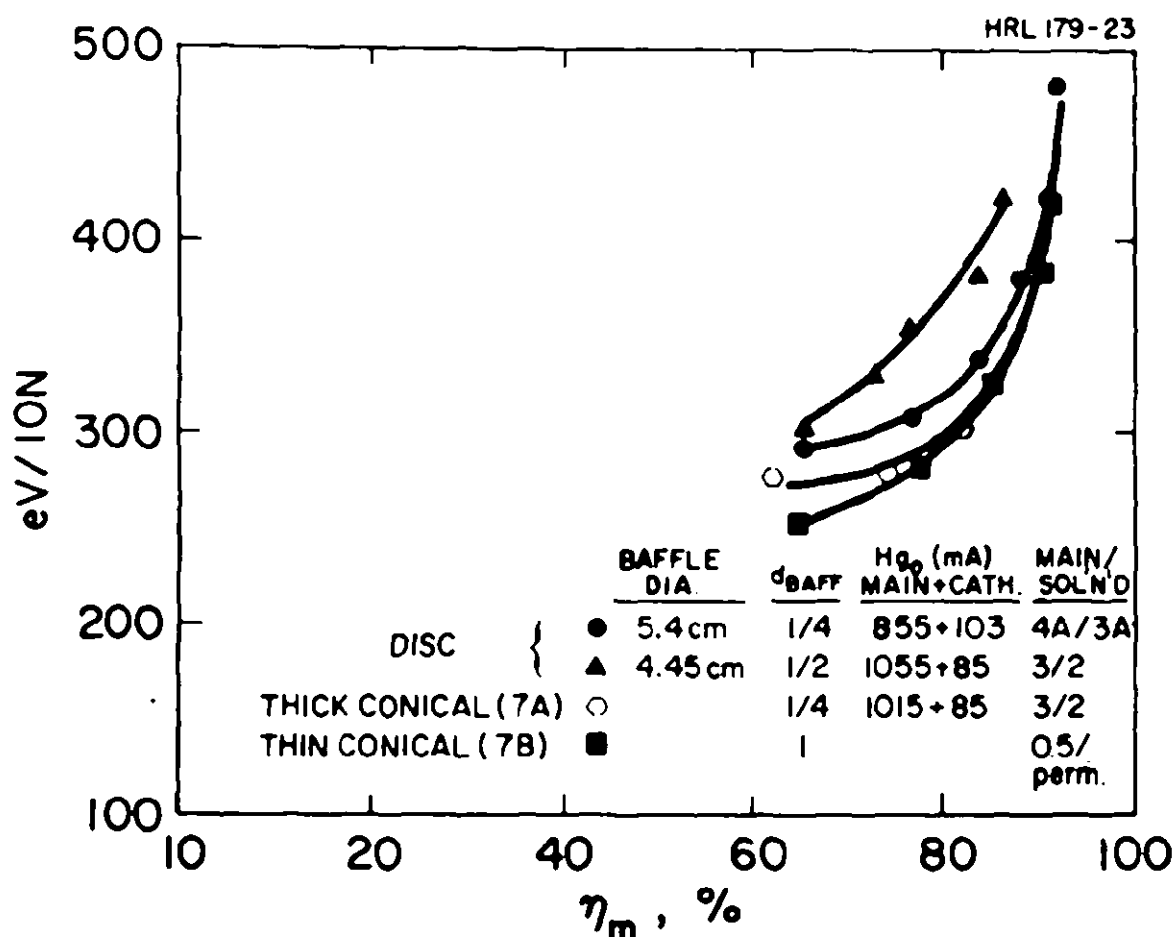


Fig. 8. HRL 30 cm thruster performance for two disc baffles and 0.63 cm thick conical baffle.

Typical beam profiles taken at two points downstream from the thruster are shown in Fig. 9. The one closest to the thruster shows a central dip due to the opaque center electrode support.

b. 100 Hour Test

An abbreviated version of the test report submitted at the conclusion of the 100 hour test is presented below:

TEST REPORT

100 Hour Test of 30 cm Thruster

May 21 to May 26, 1969

A. Thruster

A schematic of the 30 cm TASK-I thruster used for the 100 hour test is shown in Fig. 10. This permanent magnet thruster configuration is identical to that previously submitted to LeRC for design approval, except for the eight 0.35 cm by 0.66 cm bar magnets mounted radially in the rear of the discharge chamber. The magnetic field shape and strength is shown in Fig. 2(b). The fixed conical baffle (shown in Fig. 7(b)) was mounted 2.54 cm downstream from the cathode pole piece on three SERT-II type supports. The ion extraction system is a conventional grid system having a center support with a nominal gap spacing of 0.254 cm. The hole geometry is shown below:

	<u>Screen</u>	<u>Accel</u>
Hole diameter	0.38 cm	0.32 cm
Center-to-center spacing	0.44 cm	0.44 cm
Open area	72%	47%
Thickness	0.075 cm	0.254 cm

$V_+ = 3 \text{ kV}$, $V_- = 2 \text{ kV}$
 $I_+ = 1100 \text{ mA}$, $I_- = 13.2 \text{ mA}$
 $I_d = 7.5 \text{ A}$, $V_D = 40.2 \text{ V}$

HRL179-22

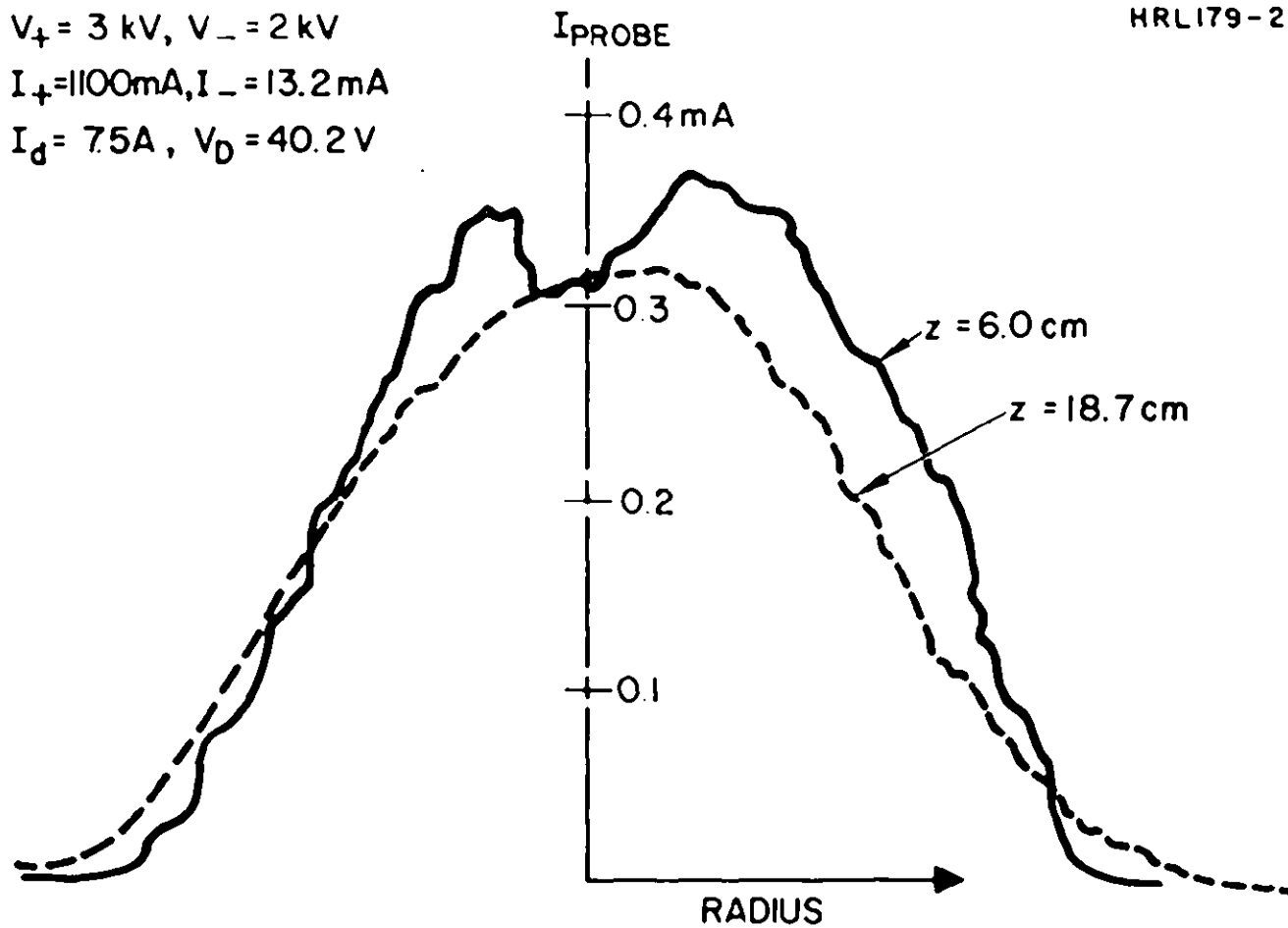


Fig. 9. Typical beam profiles taken on Task I thruster.

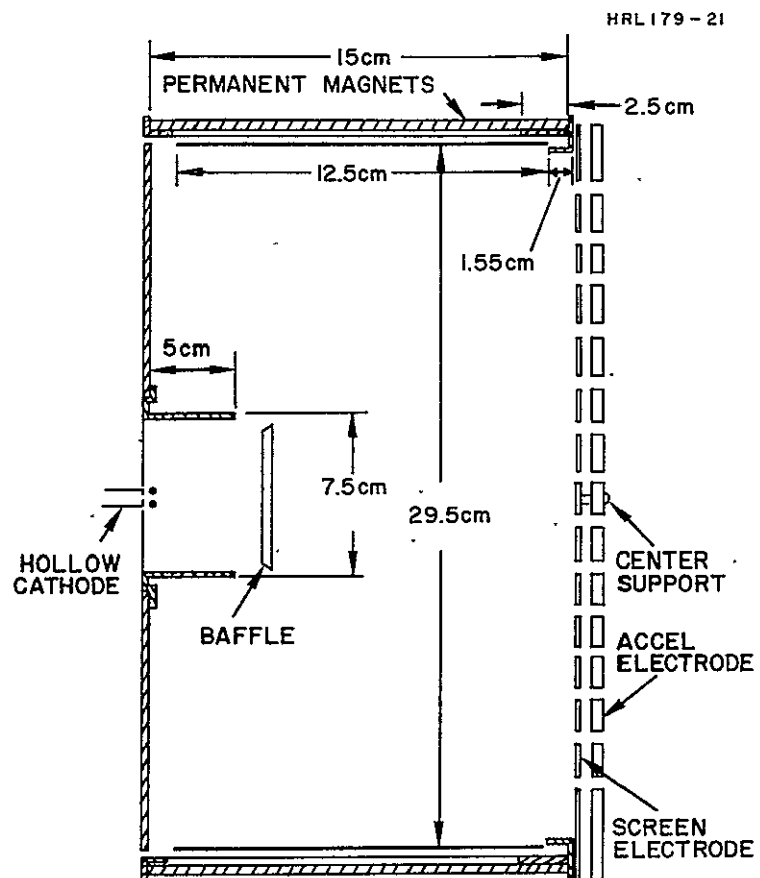


Fig. 10. Schematic of 30 cm Task I thruster.

Separate vaporizers for the 0.63 cm diameter hollow cathode and the main discharge feed system were used, with each having a precision bore glass capillary tube serving as reservoir.

B. Neutralizer

The neutralizer was a 0.32 cm diameter SERT-II type hollow cathode mounted slightly differently from the design drawing, with its orifice 2.54 cm downstream from the accel electrode and with the orifice at the anode radius. The neutralizer axis made a 30° angle with respect to the accel plane and was pointed toward the center of the ion beam. The neutralizer assembly was mounted on insulators off the thruster, and its feed system was heat shielded approximately 15.24 cm back from the cathode tip. The neutralizer had a vaporizer and capillary feed system similar to that used for the discharge hollow cathode.

C. Vacuum Facility

The test was conducted using the 3 m diameter by 6 m long vacuum facility with a typical background pressure of 3×10^{-6} Torr. This facility has a LN₂ cooled cryowall and a 2.4 m diameter water cooled collector mounted approximately 4.2 m from the thruster.

D. Instrumentation and Procedure

The circuit diagram used for this test is shown in Fig. 11. With this arrangement, the grounds for the main beam and accel high voltage supplies were made through a bank of gas filled voltage regulator tubes, limiting the thruster floating potential to -100 V if the neutralizer should fail. All the power supplies except the main beam and accel were unregulated variac type

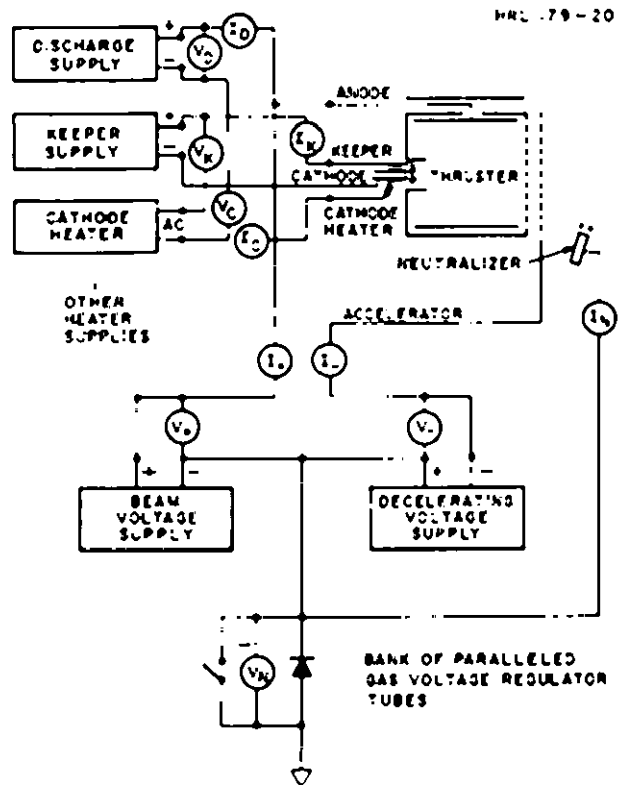


Fig. 11. Circuit diagram.

supplies.* The discharge voltage and current and beam and accel voltages and currents were read on 1% precision-calibrated meters. All the heater and keeper voltages and currents were monitored on standard 3% panel meters.

Every half hour throughout the test the electrical parameters and the mercury levels in the three capillary reservoirs were recorded. At the end of the test the amount of mercury by weight necessary to refill the feed systems to their original levels agreed to within $\sim 1.5\%$ with that computed by totaling the incremental volume amounts measured during the test.

A temperature controller, running at positive high voltage, was used to maintain a constant main vaporizer temperature during the first few hours of the test. However, it was found that this control circuit was sensitive to high voltage arcing and that the vaporizer temperature would change a few degrees after a high voltage arc, resulting in unacceptable excursions in beam current. As a result, nearly all the test was run with manual adjustment of the vaporizer powers. Typically adjustments of $< 5\%$ were made to maintain the nominal 1 A beam current with a discharge voltage of ~ 39 to 42 V.

After some experimentation prior to the test, it was found the neutralizer would automatically couple to the ion beam if the switch across the gas diodes was left open after a high voltage trip. Re-application of the high voltage would automatically strike the plasma bridge to the ion beam.

E. Results

The test was continuous except for a 3 hour period which occurred just after the ninth hour of the test. During this period the accel supply was repaired after a blower failure in this supply destroyed the high voltage output tube. After the repair the thruster ran continuously for the next 97 hours. The test was then terminated after a total run time of ~ 106 hours.

* These supplies were built recently, and replace the SCR type supplies used for all previous tests.

Variations in performance occurred as a result of the manual adjustment of vaporizer powers required because of line voltage variations. However, even averaging these less than optimum points, the over-all 106 hour average produced a total thruster efficiency of 72.5% and an electrical efficiency of 88.1%. A performance summary and breakdown of the various losses for the 105 hour average and a nine hour average is shown in Table II below.

Following the test the accelerator and the two cathodes were measured to determine the extent of erosion occurring during the test. Most of the erosion of the accel electrode was in two different regions adjacent to the neutralizer. The most severe erosion manifested itself as a saw-type cut which sliced through a 0.063 cm thick stainless annular ring mounted on the perimeter of the accel used to shield the downstream plasma from the positive potential of the screen electrode. This erosion also penetrated an additional 0.02 cm into the accel electrode. The cut was ~ 0.066 cm wide x 1.86 cm long, and appeared to have resulted from ions coming from the dense plasma between the neutralizer keeper and orifice. A second crescent shaped groove about 5 cm long and 0.025 cm deep appeared in back of the saw type cut. This could have resulted from ions originating from the plasma downstream from the keeper electrode. The crescent shape might have resulted from shadowing by the 2.54 cm diameter x 0.725 cm thick boron nitride cylinder from which the keeper electrode is mounted. An attempt will be made to control this type of erosion with a grounded shield placed so that the region adjacent to the neutralizer keeper will not see the negative high voltage.

The second type of accel erosion appeared to result from charge exchange ions coming from the plasma plume of the neutralizer. This resulted in groove type erosion pits connected to form closed hexagons around holes adjacent to the neutralizers. The deepest grooves were about 0.01 cm deep, and occurred about 5 cm from the neutralizer. Figure 12 shows the measured depth of these grooves as a function of distance from the neutralizer measured along a line with the neutralizer axis.

TABLE II
Performance Summary

	105 hour Average			9 hour Average
Beam Power	3 kV	1.008 A	3024 W	3015 W
Discharge	41.2 V	7.2 A	295	316
Accel			41 ^a	41 ^a
H.C. Heater	6.1 V	2 A	12.2	12.2
Neutralizer Heater	3.8 V	2 A	7.6	7.6
H.C. Keeper	10 V	0.28 A	2.8	2.8
Neutralizer Keeper	18 V	0.25 A	4.5	4.5
Main Vaporizer	3 V	2.4 A	7.2	7.2
H.C. Vaporizer	2 V	1.9 A	3.8	3.8
Neutralizer Vaporizer	1.8 V	2.0 A	3.6	3.6
Neutralizer Coupling	27 V	1 A	27 ^b	27 ^b
Total Power			3429	3441
Total Losses			405	426
Electrical Efficiency			88.1%	87.4%
Mass Efficiency			82.2%	86%
Total Efficiency			72.5%	73.5%
Thrust			25.2 mlb	25.1 mlb
I_{sp}			4500 sec	4700 sec
Power/Thrust			136 W/mlb	137 W/mlb

^a Because the accel current went from ~ 5 mA to ~ 13 mA when the neutralizer was turned on, we are estimating the accel power loss as (3 kV + 2 kV) 5 mA + (2 kV) 8 mA = 25 + 16 = 41 W. Note that $I_{+}V_{+} + I_{-}V_{-} = I_{B}V_{+} + P_{accel}$ where $I_{B} = I_{+}$ - direct interception, which in this case is 5 mA. This is a conservative estimate because a large fraction of the 5 mA is also charge exchange current.

^b Here we added an estimated beam potential of 12 V (taken from Ref. 6) to the -15 V thruster floating potential measured throughout this test, to arrive at a total coupling voltage = 12 + 15 = 27 V.

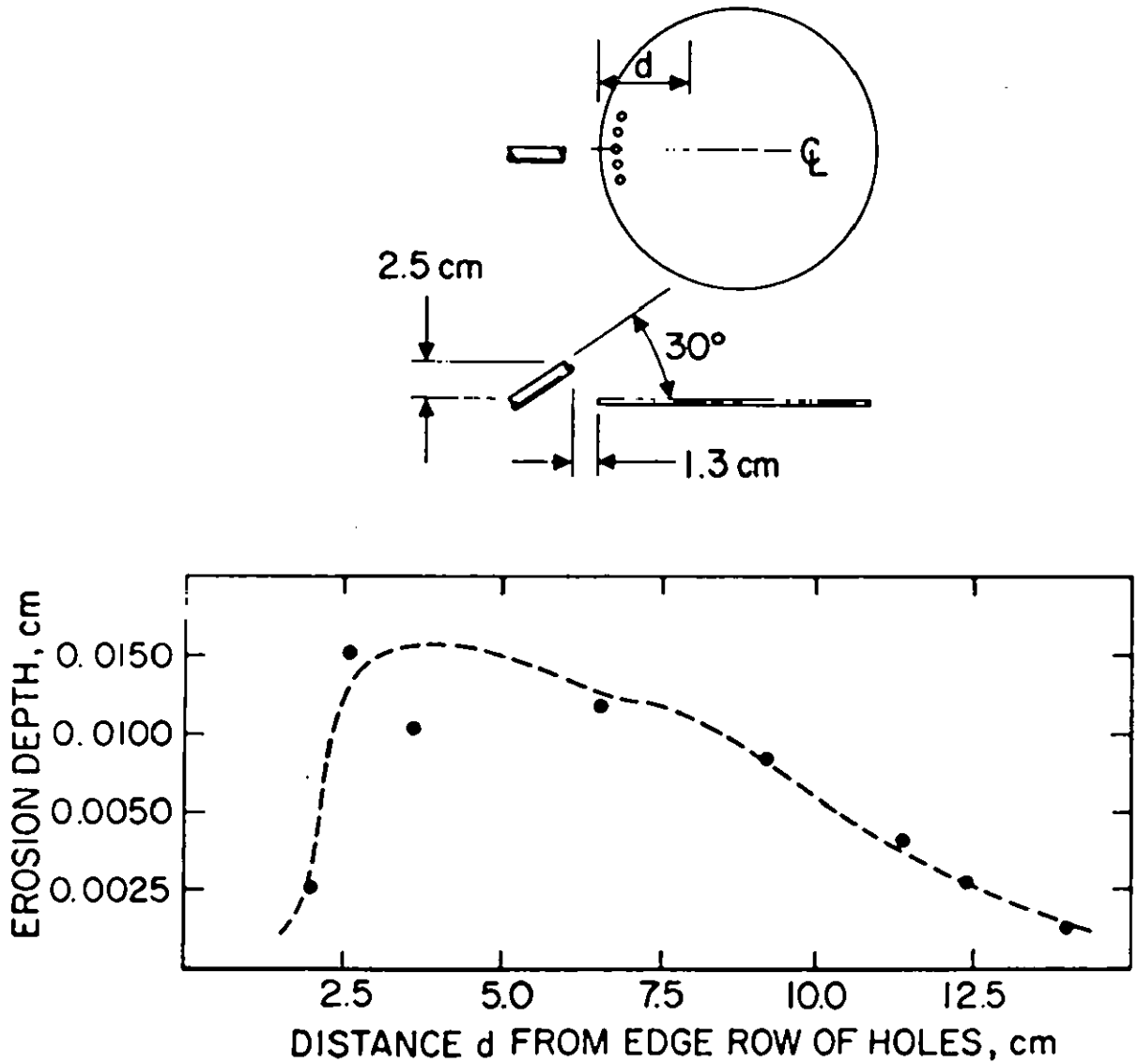


Fig. 12. Measured depth of accel groove erosion in line with neutralizer axis.

It may be possible to reduce this type of erosion by either pointing and/or moving the neutralizer farther downstream. The effect of these changes on the neutralizer coupling voltage was investigated in Tasks II and III.

In contrast to the cathode that had been used for several hundred hours in the experimental thruster during the configuration tests, the life test cathode in the main discharge chamber showed a sharply defined erosion pattern. The original 0.025 cm aperture was increased to 0.060 inch at the cathode face. The conical pit reached almost through the 0.15 cm cathode face. This anomalous result has not been explained.* A possible cause may be the large open area between the baffle and the cathode pole piece with the baffle in its optimum position. This permits more of the discharge plasma to "see" the cathode, and hence may permit more high velocity ions to strike the cathode surface. However, the sharply defined erosion pattern is difficult to reconcile with this model. Further tests are required to confirm and define this erosion pattern.

The neutralizer cathode showed no measurable erosion during the test.

3. Conclusions from Scaling Study

At the completion of this scaling study (the Task I contractual effort) the following conclusions could be drawn:

- a. The SERT-II hollow cathode thruster had been scaled to double its diameter without sacrificing efficiency or stability. This was most readily accomplished here by the addition of radial permanent magnets at the rear of the discharge chamber. This method of shaping the field of course is not unique and may be accomplished equally well by other choices of magnet location and pole piece shape.
- b. Significant cathode erosion was observed during the 100 hour test. As is shown later, this may be corrected by properly shaping the cathode aperture.

* See Section III-B-3-a for the improved cathode design which shows no erosion after testing.

- c. Accelerator erosion of two distinct types was observed during the 100 hour test. The first apparently originated from mercury ions generated in the plasma plume at the neutralizer cathode orifice. These are attracted to the negative accelerator electrode and erode narrow areas of this structure. It appears that some focusing action from the neutralizer keeper may affect the erosion patterns as well. The second type was an enhanced charge exchange erosion pattern on the downstream face of the accelerator. The observed pattern was consistent with that expected from a conical beam of neutral particles emanating from the hollow cathode neutralizer with a half angle of 45° . If this model is correct, pointing the neutralizer downstream at an angle greater than 45° should significantly reduce this erosion. Because all later tests were run at a much lower accelerator voltage (~ 500 V) where the sputtering coefficient is much lower, it was not possible to confirm this model in later tests.

B. LOW SPECIFIC IMPULSE OPTIMIZATION AND TEST

The purpose of Task II was to investigate methods of operating the 30 cm high specific impulse thruster described above at a power level of 2.5 kW and a specific impulse of 2750 sec (i.e., $V_{\text{beam}} = 1000$ V at $\eta_m = 87\%$). Using nominal values for the power losses, this means that the beam current must be 1.85 A.

Task III provided an opportunity to improve discharge chamber and neutralizer performance using the low specific impulse optic design as the test vehicle. Improvement was necessary to achieve the contractually specified performance, which required gains in both mass and power utilization over the Task I high specific impulse design. Fortunately, the insulated optics themselves helped to achieve this goal.

A series of design verification tests were scheduled - 100 hours at the end of each of Tasks II and III, and 500 hours at the conclusion of the program (Task IV). Because essentially the same facilities and procedures were used for each task, these tests are all reported in this section.

1. Ion Optical Design and Test

The reduction in beam voltage, coupled with the increase in beam current for low specific impulse operation, requires that the perveance of the ion extraction system be significantly increased. The various implications of this required increase in perveance are discussed in this section.

Two designs are presented: (1) a conventional design, and (2) a single grid system, insulated on the discharge chamber side with a composite high temperature glass and refractory coating.

During the study various structural elements and geometries were considered for each system. These included straight metal or ceramic bars, honeycomb, woven screen, and perforated ceramic plates. For various reasons, none of these were judged superior to the perforated molybdenum plates proposed for the designs.

The method of perforating the plates was considered carefully. For the reasons discussed below, the electrodes for the close spaced optics were drilled and those for the insulated optics were chemically milled.

As a result of a combined experimental and analytical thermomechanical analysis, the electrodes were mounted under radial tension. This mounting technique provides some stability against thermal warping, but is used primarily to assure that no radial clamping will occur that would buckle the electrodes.

Calculations indicate that the lifetime of the electrode system (as limited by erosion by charge exchange ions) should not represent a limitation on the design. A principal factor in this estimate is that the charge exchange ions which come from the downstream beam plasma have only a few hundred volts of energy because of the low decelerating voltage used (~ 500 V). Because of the low ion energy, the sputtering coefficient is reduced to the point where erosion is relatively small.

In order to implement the insulated optics design, an extensive program was required to devise a technique to apply the insulating coating. A unique two-component coating system has resulted which has proved both versatile and effective. This process is discussed in detail elsewhere in this report.

a. General Design Criteria

1. Design Trade-Offs - In the design of an ion optical system a number of electrical and mechanical parameters must be specified to assure that the system will function properly within the desired specifications. A number of these parameters were specified directly by the contract; others were at the discretion of the designer to fulfill the entire set of contractual obligations. The first category included

specific impulse I_{sp}	=	2750 sec
beam voltage V_B	=	1000 V
beam current I_B	=	1.85 A
electrode lifetime	=	10^4 hours
thruster size	=	30 cm
thruster efficiency	=	64%

Among the parameters to be chosen by the designer were

size, shape, and number of apertures

accel-decel ratio which defines the total available extraction voltage

electrode thickness

electrode spacing

method of mounting the electrodes to the thruster

methods of manufacturing (including the techniques used to fabricate the electrodes themselves and the tolerances required to assure proper performance).

These latter trade-offs are discussed in general in the following sections, and are then applied specifically to the design of conventional and insulated ion optical systems to fulfill the above goals.

2. Aperture Dimensions — The beam current and extraction voltage are related by

$$I_{\text{beam}} = N P_h V_T^{3/2} \quad (1)$$

where

$$\begin{aligned} I_b &\equiv I_{\text{beam}}, \text{ amperes} \\ N &\equiv \text{number of apertures} \\ P_h &\equiv \text{average perveance/hole} \\ V_T &\equiv \text{total extraction voltage, volts.} \end{aligned}$$

If the beam current and total voltage are specified, an expression is obtained which relates the total number of holes to the average perveance associated with each hole. As shown in Fig. 13, the average perveance per hole may be determined using a number of techniques; the most common methods are calculation on a digital or analog computer, or analysis of experimental data from operating thrusters. Figure 13 shows limits to the calculated values which may be derived directly from Child's law or from an equation derived by Kramer⁷ which makes allowance for the potential depression caused by the aperture in the accelerator. Note that the calculated perveance for at least three particular cases lies fairly close to this latter line.

The experimental data cover a broad range in the region from 25 to 50% of the maximum value, as shown in Fig. 13. This reduction in performance results because the calculated values represent maximum perveance per hole, while the experimental values represent average perveance per hole and make allowance for the fact that the plasma density varies across the thruster diameter and is a maximum only in the center. The experimentally-calculated values could be expected to coincide more exactly only if the plasma density were perfectly uniform. In two cases data are available for more than one spacing for a given electrode set. These data points are connected by dotted lines in Fig. 13 and show approximately the variation with d/w predicted by the analytical expressions. The basic conclusion is that it is very difficult to achieve average values of perveance per hole greater than $4 \times 10^{-9} \text{ A/V}^{3/2}$, even by extrapolation of the best experimental data taken to date.

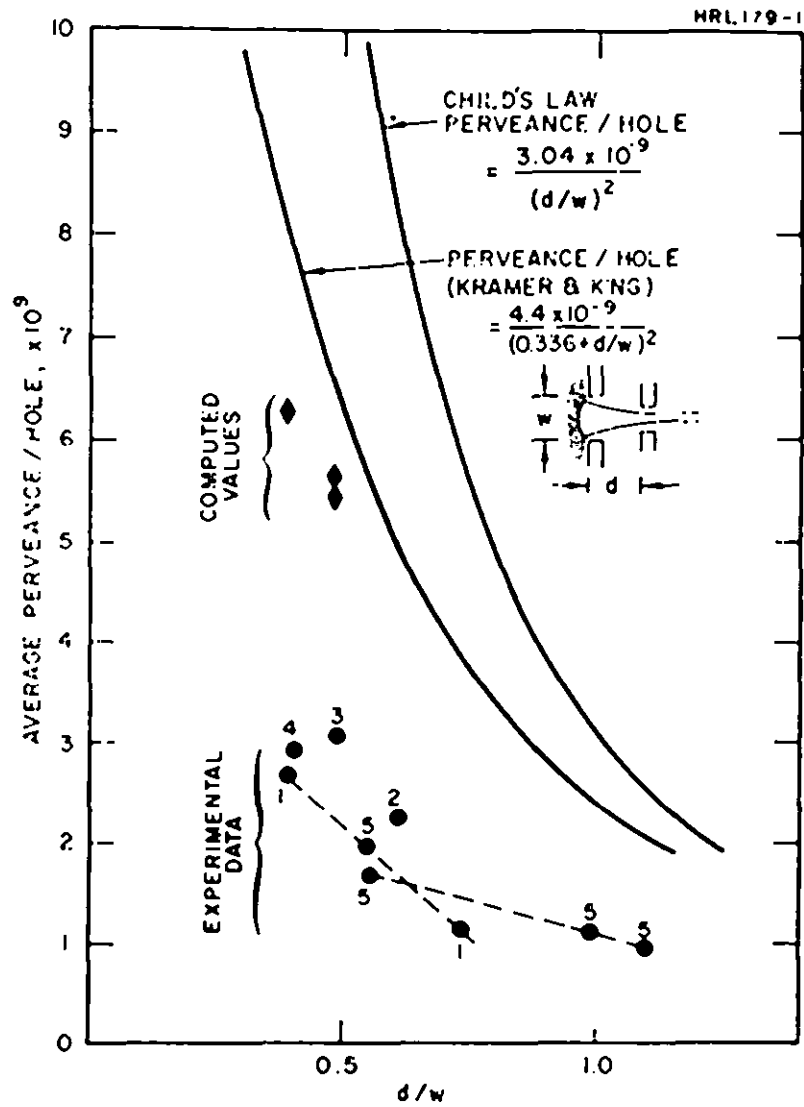


Fig. 13. Comparison of experimental and computer calculated perveance with Child's law value.

Data Point	Thruster Diameter, cm	V_m , kV	References
①	30	5.0	Task I
②	30	2.0	EAC 1968
③	20	5.0	H.J. King, J. Spacecraft Rockets <u>5</u> , 591 (1968).
④	20		T. Masek and E. Pawlik, "Thrust System Technology for Solar Electric Propulsion," Paper No. 68 541, AIAA 4th Propulsion Joint Specialists Meeting, Cleveland, 1968.
⑤	15		Kramer and King. ⁷

Equation (1) may be combined with the general expression for the number of holes per unit area in a hexagonal close-packed array as a function of the center-to-center spacing between the holes, to give the following expression

$$\lambda = 1.07 \left(\frac{P_n A}{I_B} \right)^{1/2} v^{3/4}. \quad (2)$$

This equation is shown in function form in Fig. 14 for $I_B = 1.95$ and area = 660 cm². When the experimental values measured for both insulated and conventional ion optical systems are compared with Fig. 14, they define the maximum center-to-center spacing for the apertures in the electrode system for any given beam current. For optimum structure and lifetime, the center-to-center spacing and hence the electrode thickness should be as large as is possible. The electrode dimensions are thus defined to within relatively narrow limits by this technique. If the screen open area is chosen to be as large as practical (60 to 70%), the aperture diameter of the screen may be defined directly. Depending on the exact electrode design chosen, the accel aperture diameter will normally be 2/3 to 3/4 that of the screen. Therefore, all dimensions except the interelectrode spacing are nominally defined. From Fig. 13 it is clear that it is desirable to minimize this spacing in systems requiring maximum perveance. Depending on the exact design, several factors may limit the breakdown limit. At the relatively low total voltages employed here (< 2 kV), very small spacings of the order of 10⁻² cm could be accommodated. Thus, this does not place a limit on the design. A third consideration in reducing the interelectrode spacing is the quality of the gun design. Small values of d/w generally will produce a less collimated beam, and thus a relatively higher accel-decel ratio is necessary to assure that the negative voltage is adequate to prevent backstreaming.

3. Thermomechanical Design Analysis - All proposed electrode systems consist of one or possibly two close spaced thin perforated plates. The exact position of these plates under operating conditions and their stability as a function of varying thermal and mechanical loadings is vitally important to the performance of the thruster. This problem was investigated both analytically and experimentally. The modeling technique used general but versatile computer simulation programs from the HAC library of computer programs. Both were completely developed, well documented programs which have small execution times for our applications.

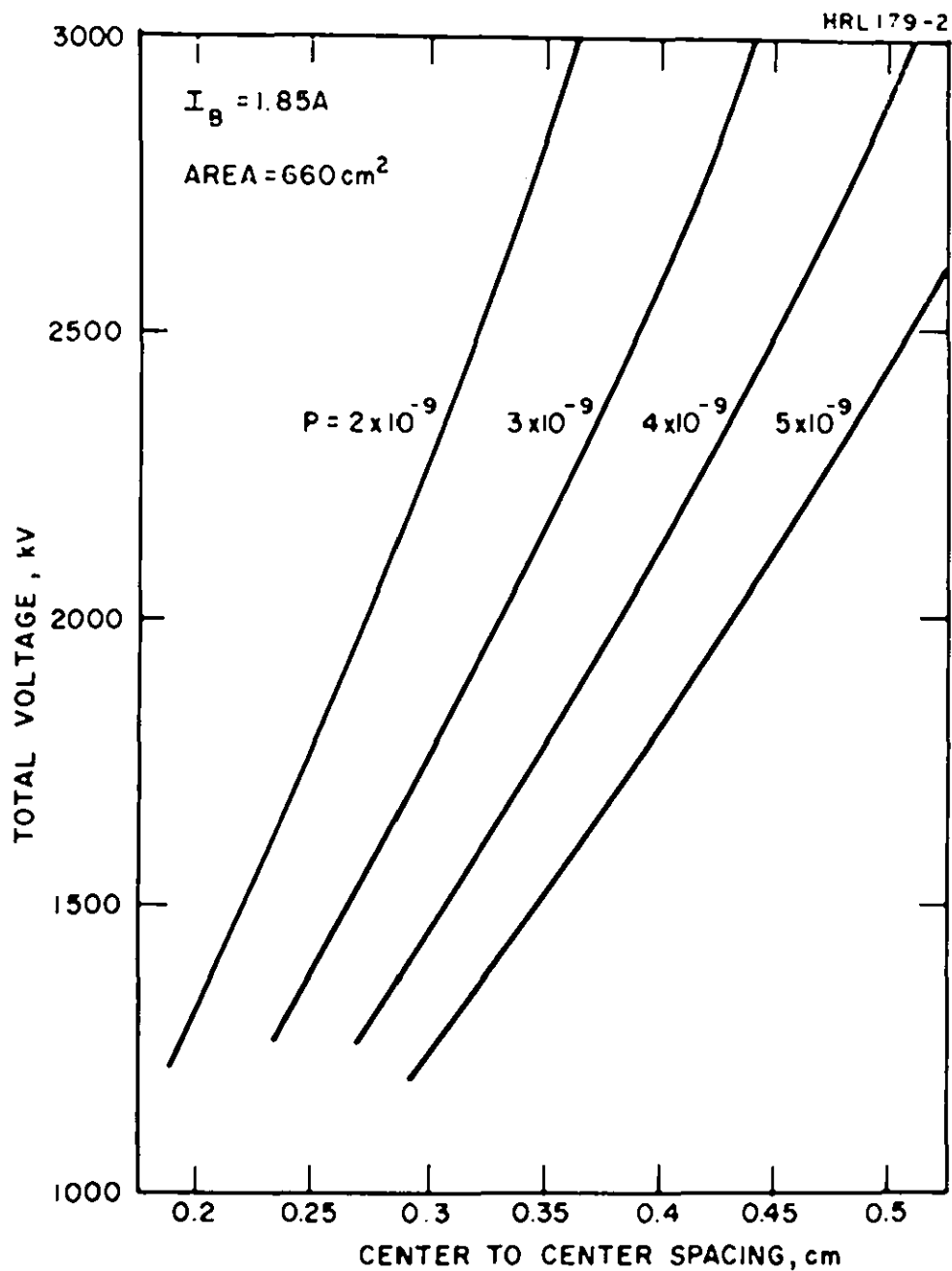


Fig. 14. Perveance/hole requirements for 1.85 A beam from 30 cm thruster.

The first is a heat transfer analysis program called TAS-1B which is used to solve for the temperature distributions and heat flows in the electrode system. This digital computer program solves for the steady-state temperature distribution in a lumped parameter network of temperature points (nodes) and heat flow paths (resistors). A node is provided for each constant temperature portion of the device being modeled. The network may contain up to 80 nodes and each node may be connected to any or all of the others. Any two nodes may be connected by two resistors. One represents conduction and/or convection; the other represents infrared radiation. TAS-1B does not account for the temperature dependence of thermal properties, and so heat flows due to conduction and convection are linear with respect to node temperatures. Infrared radiation is not linear because it depends on the fourth powers of the absolute temperature. Any two nodes, then, may be connected by a linear resistor, a radiation resistor, or both. In addition to interchanging heat with other nodes, each node may receive radiation and/or a direct heat input (such as from internal dissipation of electrical energy); TAS-1B does not permit a node to produce a direct heat output.

The second computer program chosen performs structure analysis of shells by a finite element method. Shells of revolution subject to axisymmetric or asymmetric mechanical and thermal loads can be handled. An electrode is divided into washer shaped regions which form the elements of the model. Thermal and mechanical loads are prescribed on each element and the computer program solves the equations of motions for the deformations. Since the dimensions of each element can be specified independently, initially dished and tapered electrodes can be considered. Since the stress analysis program considers solid plates, and the electrodes are perforated, an equivalent set of thermal and elastic parameters are used in the solid plate analysis in order to simulate the actual punched plate electrode. Justification for this substitution has been found in the literature.'

The major effort that has been required to use these computer programs is to prepare their inputs. For the thermal analysis program the view factors for the radiative heat transfer were the most difficult inputs to find. Fortunately, the view factor formulas recently derived¹ were for a range of electrode geometries which includes the low specific impulse case. The other inputs to the thermal analysis are the thermal conductance between nodes and the heat input from the discharge chamber.

The final electrode shape is calculated by an iterative procedure. The temperature profiles, support placement, initial shape of the electrode, thickness, and effects of any radial clamping on the electrode mounts may be readily investigated using this analytical technique. The objective of this study is, of course, to find an electrode system that will remain sufficiently stable under typical operating conditions to properly extract and focus the ion beam without interelectrode shorting. The effects of the different variables are summarized as follows:

(a) Temperature profiles. The thermal model of the electrode system has the form of a network of nodes, each of which corresponds to a constant temperature region on an electrode. For axisymmetric heating, the nodes are washer shaped (annuli) regions on the electrodes. Heat is transferred between adjacent washers of each electrode by conduction and between opposite washers of the two electrodes by radiation. An additional constant temperature node N_B , which represents the background, absorbs heat radiated directly from the accelerator electrode and from the screen electrode by way of the holes in the accelerator electrode. The heat input to the grid system from the discharge chamber is presented by a distribution of black body radiation which is incident on screen electrode and varies radially in intensity. The two temperature profiles used in this study are shown in Fig. 15. These profiles⁹ were calculated for an incident power of 250 W and a peak to average heat intensity of 1.5:1 across the screen electrode and an accel interception power of 20 W. The resulting profiles, called "A" for the screen electrode case ($T_{\text{center}} = 442^\circ\text{C}$ $\Delta T = 35^\circ\text{C}$) and "B" for the accel electrode case ($T_{\text{center}} = 293^\circ\text{C}$ $\Delta T = 30^\circ\text{C}$), were used throughout this study. These standard temperature profiles were used to assure that the results calculated would be consistent among themselves because it was desirable to compare the effects for different loading conditions. The actual magnitude of the buckling deformation is much more sensitive to the temperature gradient than the absolute temperature level, while the amount of radial displacement depends on the average temperature.

(b) Support placement. Table III summarizes the different support arrangements which were investigated. All cases were for an electrode thickness of 0.05 cm and an initial dish of 0.10 cm. Temperature profile "A" was used, and no radial constraint was imposed. The resulting axial displacements measured from the initial shape (parabola with 0.10 cm dish) are plotted in Fig. 16.

The optimum configuration studied has both a center and edge support. Comparing only those cases which have a center support, there is a progressive decrease in axial displacement as the edge support is moved away from the center. The 0.250 cm

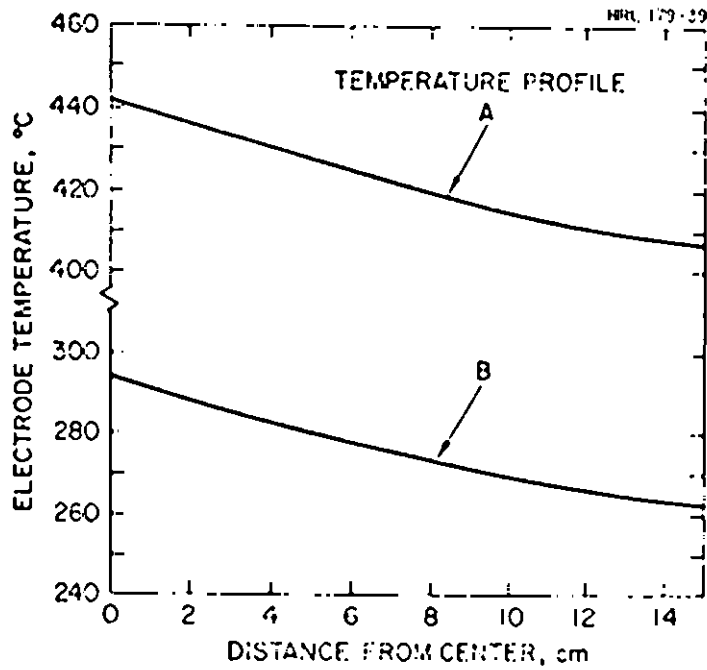


Fig. 15. Temperature distributions used for thermal buckling analysis.

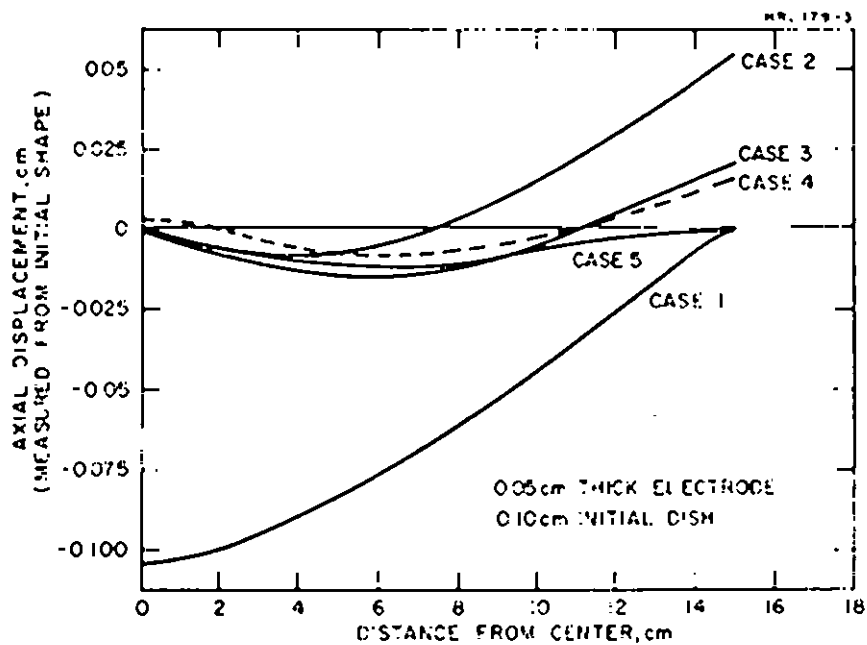


Fig. 16. Effect of support placement, no radial constraint, temperature profile "A".

thick electrode has more than an order of magnitude less displacement for identical electrode support configuration, initial dish, and temperature loading than the otherwise identical 0.05 cm thick case (Cases No. 3 and 6). The effect of moving the center support outward can be seen in Cases No. 1 and 4.

TABLE III

Summary of Support Configurations

0.05 cm thick, 0.10 cm dish, temperature profile "A"			
Case Number	Center Support	Edge Support, cm	Change in Shell Depth, cm
1	No	30	0.103
2	Yes	15	0.063
3	Yes	22.5	0.036
4	No	4.4 & 15	0.027
5	Yes	30	0.013
0.25 cm thick, 0.10 cm dish, profile "A"			
6	Yes	22.5	0.002

(c) Initial dish. The effect of the initial depth on the axial displacement was investigated for depths ranging from 0.01 to 0.042 cm. This was done using the same thermal loading as above, with no radial constraint, and for electrode thicknesses which ranged from 0.05 to 0.25 cm. Two different configurations were considered, both with center supports. The first had an edge support at 22.5 cm and the second at 30 cm. The cases are summarized in Table IV. Note that it is generally desirable to minimize the initial dish to keep the axial displacement at the lowest possible value.* For the 0.05 cm thick case it is seen an initial dish of ~ 0.20 cm results in a maximum axial displacement; for larger initial dish values, the axial displacement decreases slowly. For the range of initial depths considered, this decrease is not observed for the 0.127 cm case.

* Some dish is needed to insure that the resulting bowing will be in the right direction.

TABLE IV

Change in Shell Depth for Different Initial Depths

Center Support and Edge Support at 22.5 cm				
Initial Dish, cm	Thickness, cm			
	0.05	0.09	0.127	0.250
0.01	0.008			
0.05	0.023		0.004	
0.10	0.036	0.015	0.008	0.002
0.21	0.040		0.013	
0.42	0.029		0.017	
Center Support and Edge Support at 30 cm				
0.01				0.0002
0.05	0.013			
0.10				0.002
0.21				0.005
0.42				0.007

(d) Thickness. Reading across Table IV, the effect of thickness can be seen for an initial dish of 0.1 cm with a center support and edge support at 22.5 cm diameter. These data, which are plotted in Fig. 17, illustrate the rapid increase in axial displacements for electrode thicknesses less than ~ 0.1 cm. Thus thermomechanical considerations dictate the use of the maximum permissible electrode thickness, consistent with the constraints imposed by discharge efficiency and ion-optical characteristics.

(e) Radial clamping. For a realistic estimate of the amount of thermal buckling it is necessary to include the effects of the radial constraint imposed by the electrode supports. In this analysis we consider the zeroth

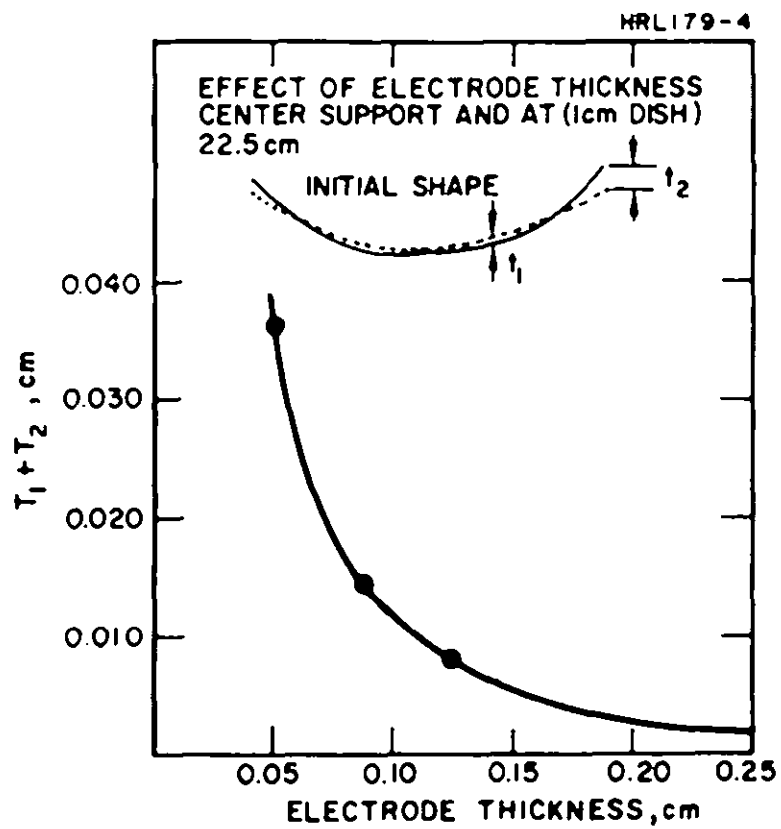


Fig. 17. Effect of electrode thickness; center support and at (0.1 cm dish) 22.5 cm.

order approximation in which the electrode supports are replaced by a constraint which fixes the radial boundary at a given radius. The case of interest is first run with no radial constraint, which permits the outer edge to expand to a certain value. The case is then re-run with this value minus a ΔR constraint which we have chosen to be 0.001, 0.0025, and 0.005 cm. Table V shows the sensitivity of the axial deformation to this type of constraint for a variety of cases. For example, a radial constraint of 0.001 cm increases by more than an order of magnitude the axial displacement compared with the no constraint ($\Delta R = 0$) case. The above data are plotted in Fig. 18. While a much more complete analysis is necessary to predict the actual equivalent radial constraint imposed by a given discrete support, it is apparent that the optimum electrode support will have the highest possible compliance in the radial direction.

(f) Temperature distribution. The effect of temperature distribution is shown below for a 0.050 in. thick electrode with an initial dish of 0.10 cm, and a center and edge support.

	$T_{\text{Center}}, ^\circ\text{C}$	$\Delta T, ^\circ\text{C}$	Change in Shell Depth, cm
Temperature Profile "A"	442	35	0.013
Temperature Profile "B"	293	30	0.0108

In this case, which has no radial constraint, the deflection is relatively insensitive to the absolute temperature level. On the other hand, the magnitude of radial displacement is nearly directly proportional to the temperature gradient. With a radial constraint of a given ΔR , the absolute temperature level would be expected to have a strong effect.

TABLE V

Change in Shell Depth for Different Radial Constraints
(0.125 cm thick; Center and Edge Support
Temperature Profile "A")

Radial Constraint, cm	Initial Dish, cm			
	0.01	0.10	0.20	0.41
$\Delta R = 0$	0.000235	0.00230	0.0045	0.007
$\Delta R = 0.00125$	0.0053	0.040 (0.110) ^a	0.045	0.035
$\Delta R = 0.0025$	0.011	0.077 (0.20)	0.085	0.063
$\Delta R = 0.0050$	0.021	0.150 (0.40)	0.166	0.120
^a Values in parentheses are for 0.05 cm thick electrode.				

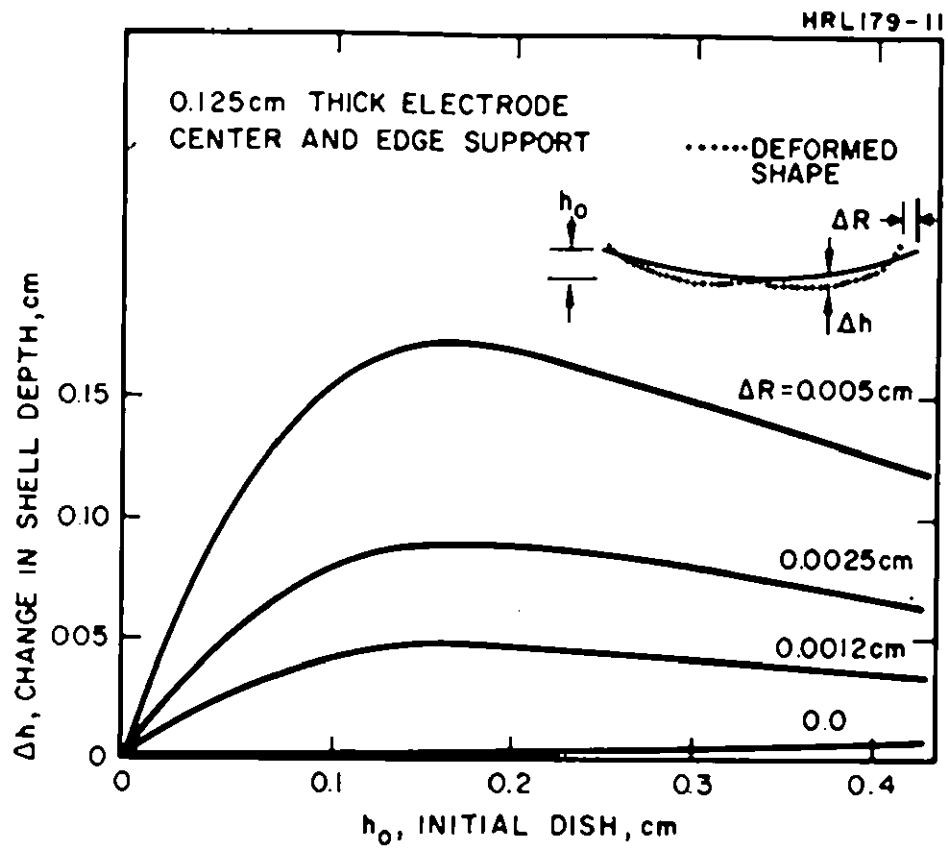


Fig. 18(a). Effect of initial shape on thermal distortion.

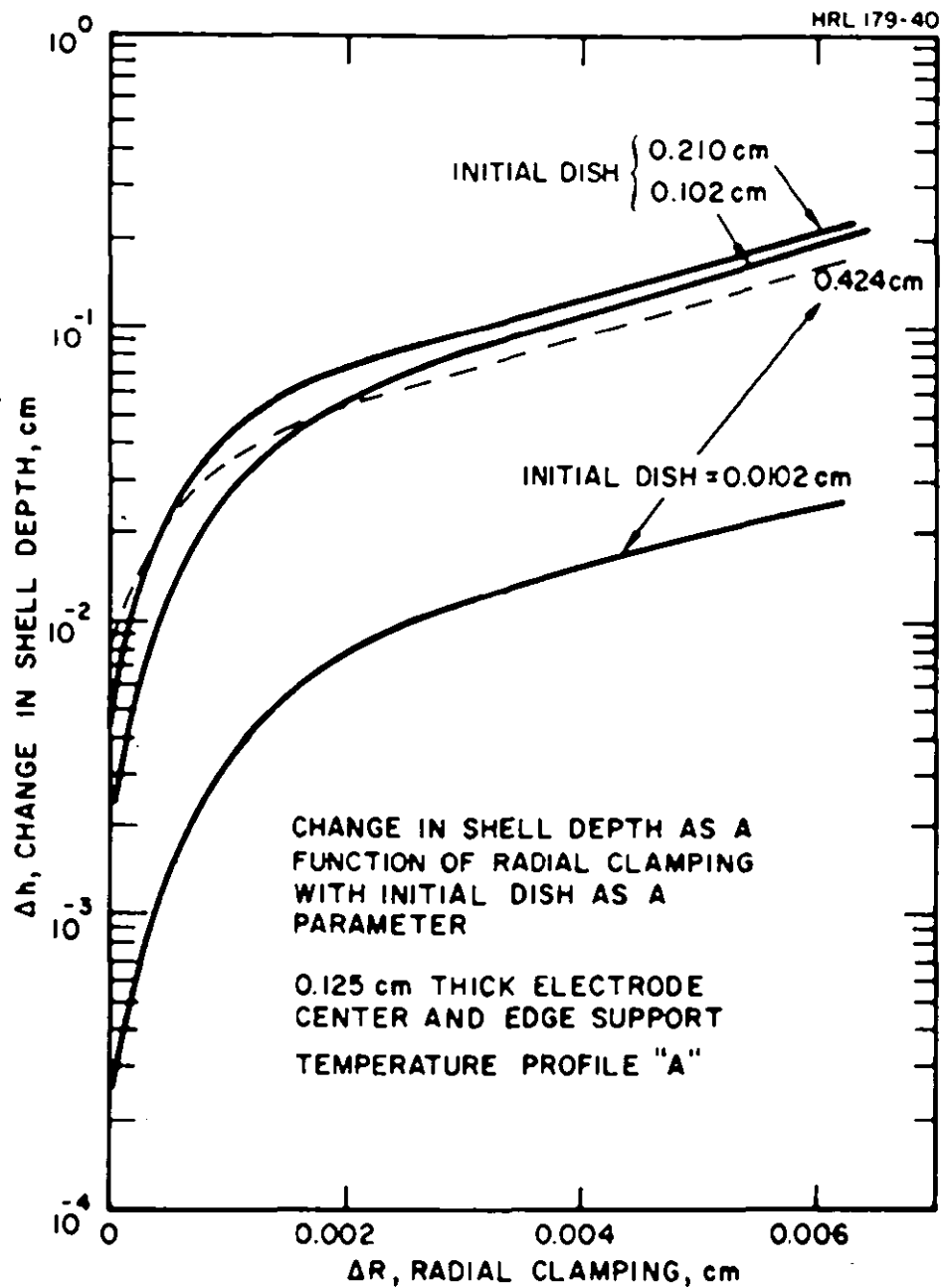


Fig. 18(b). Effect of radial clamping on plate distortion.

(g) Summary. The following general conclusions can be made:

1. when supported only at two radii, center and edge supports are superior to supports located at other radii.
2. thicker electrodes are more resistant to thermal warping
3. initial shape should be either flat or greater than 0.5 cm dish
4. radial clamping should be minimized (radial tension desirable).

4. Thermal Simulation Experiments - Bench tests were set up to check the validity of the calculations. Molybdenum plates 0.051 cm and 0.127 cm thick were annealed at 1050°C for 1 hour between heavy iron plates which had been surface ground to assure flatness. After annealing, the plates were inspected and found flat to ± 0.0127 cm. These plates were placed in a thermal test setup which consisted of a stainless steel ring to support the plates at their perimeter plus provision for a central load to simulate the center support, which is attached to the other electrode. The support ring and the plate itself could be heated to produce any desired temperature and temperature gradient. The temperatures were measured with thermocouples attached to the electrodes at ten locations across a diameter. The electrode shape was measured with an alignment telescope which could be focused on markers fixed to the electrode along two mutually perpendicular diameters - one with and one across the "grain" produced by rolling the sheet (Fig. 19).

In general the deformation of the test piece was increased simply by the handling necessary to put it in the fixture, and by the method of support. In contrast to the calculated shapes which are always regular and symmetrical, the measured values were irregular and often not reproducible. The average deformations were on the order of three times those calculated. This result is not unexpected, of course, because the test pieces contain residual stresses from the rolling and working process that were not totally annealed out. The experiment also differs from the calculation because the periphery of the plate was free to lift off the support ring in the test, but was confined to a plane in the calculations. The support structures used to mount the

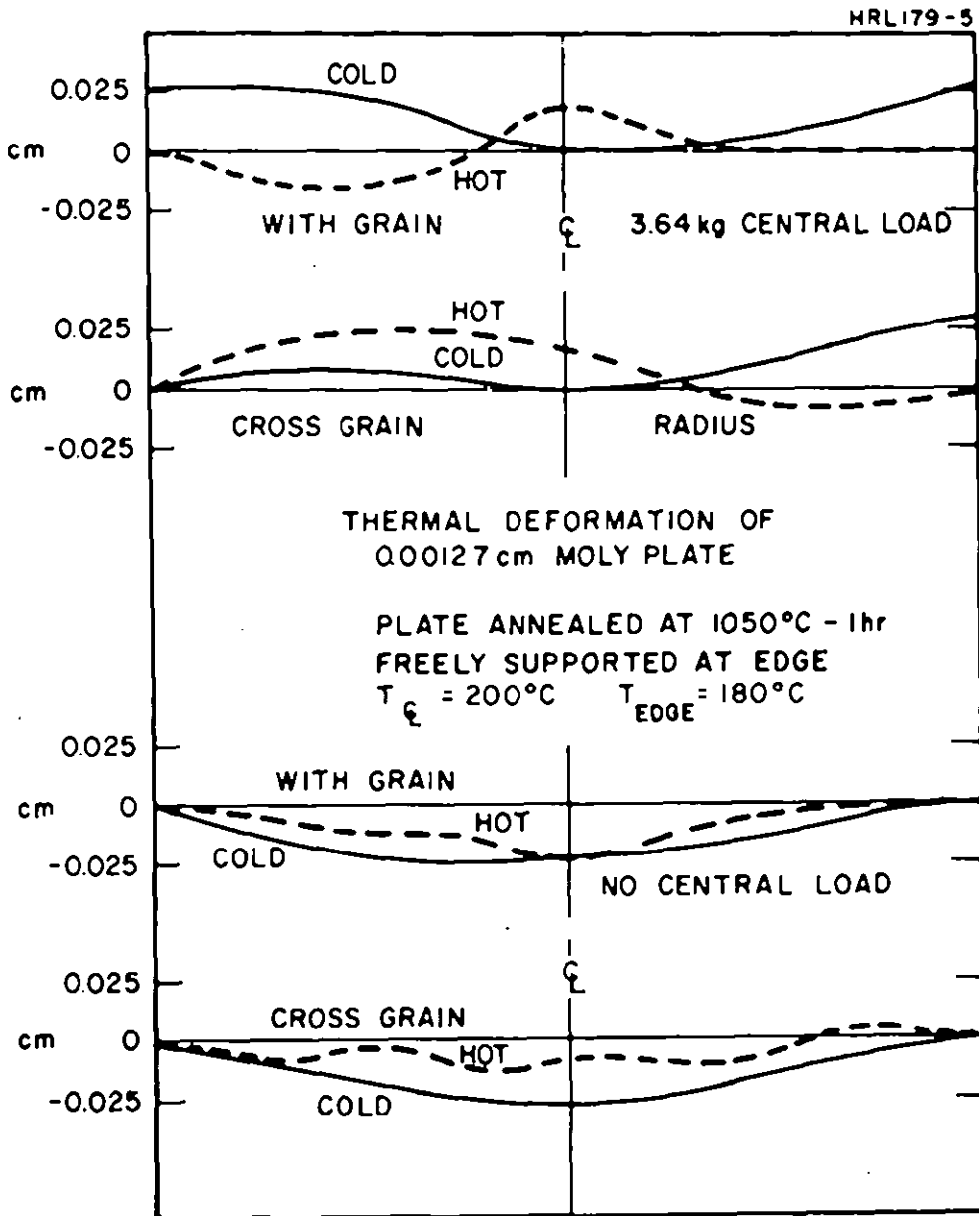


Fig. 19. Experimentally measured thermal distortion of thin plate.

electrodes on the thruster are designed to provide radial tension while confining the electrode periphery to a fixed plane. This technique improves the stability of the electrodes over that observed in the above tests.

The general conclusions to be drawn from the above calculations and tests are that thermal deformation of the order of ± 0.025 to ± 0.038 cm may be expected in a 30 cm diameter electrode. This amount is tolerable, but it may be necessary to increase the interelectrode spacing in the conventional optics above its optimum value to assure stable performance. This increase in spacing reduces the perveance below its maximum value, but still permits the design goals to be achieved. The above results also emphasize the need for a carefully controlled annealing procedure and an electrode support structure which minimizes thermal distortion.

5. Electrode Lifetime — The electrode lifetime estimated here assumes that the structure is adequate electromechanically, so that wear-out failure will occur only due to sputtering erosion. In the analysis only the effect of charge exchange ions from the downstream plasma is considered. Thus, erosion which may result from ions in the plasma adjacent to the hollow cathode neutralizer is excluded in this study. A number of factors make it difficult to accurately predict mean time to failure. The principal difficulty is that the exact energy and angle of the impinging charge exchange ions are not accurately known. It is assumed here that the charge exchange ions which reach the accel have energy equal to the decel voltage, and not total voltage, as is usually assumed. This assumption is considered reasonable because the charge exchange ions originate in the downstream plasma and fall through to the decel voltage of the accelerator electrode. It is also in agreement with estimates of the sputtering coefficient made from erosion measurements on accelerator electrodes.⁸ These are consistent with ion energy of approximately one-half the decel voltage rather than the total voltage, as has often been used previously. The uncertainty in sputtering coefficient of the impinging ions is compounded by the uncertainty in the radial distribution of both the ions and the neutrals which emanate from the thruster. It is also difficult to predict the extent to which an accelerator electrode may be eroded before it ceases to function properly. In the following calculations it is assumed that failure occurs when 50% of the accelerator mass has been removed. When the above assumptions are applied to accelerator electrodes with 50% open area, the following equation may be derived to represent the relationship between the four variables.

$$T = \frac{5.7 t}{\alpha J} \quad (3)$$

where

- T = electron lifetime in hours
- t = accelerator thickness in centimeters
- α = sputtering coefficient
- J = charge current density impinging on accelerator.

The nomograph in Fig. 20 permits a better visualization of the relationship between these variables. As illustrated in Fig. 21, it may be estimated that with the above assumptions, a 0.05 cm thick accelerator electrode would last 10,000 hours with a 1% drain current impinging at 500 V energy. The above values are consistent with the designs presented below. Perhaps the most important conclusion is that for a conventional ion optical system it may be easier to satisfy lifetime requirements than the structural requirements imposed by the thermomechanical analysis presented above.

b. Conventional Optics

1. Introduction — For the purpose of this report a conventional ion optical system is defined as one consisting of two metallic plates with matching apertures. The basic advantage of this type of system is that their performance is well understood because they have been used for a number of years. Conventional systems have demonstrated stable operation at relatively low drain currents and have extrapolated lifetimes of 10,000 hours or more. The disadvantage is primarily structural, particularly in low specific impulse designs of the type of interest here. Problems arise in devising methods of support to minimize the thermal warping which may occur during operation. There are also difficulties involved in manufacturing the electrodes themselves, which require as many as 15,000 matching apertures in each plate.

2. Survey of Existing Hardware Performance — Because this type of system has been used for a number of years, it is possible to compare the performance from a number of different sources for thrusters of different diameters. The average perveance per hole calculated from published data taken at the Hughes Aircraft Company, NASA Lewis Research Center, and Jet Propulsion Laboratory ranges from 1 to 3×10^{-9} A/V^{3/2} per hole for the aperture sizes generally employed (i.e., 0.32 to 0.475 cm diameter). Experiments with close spaced

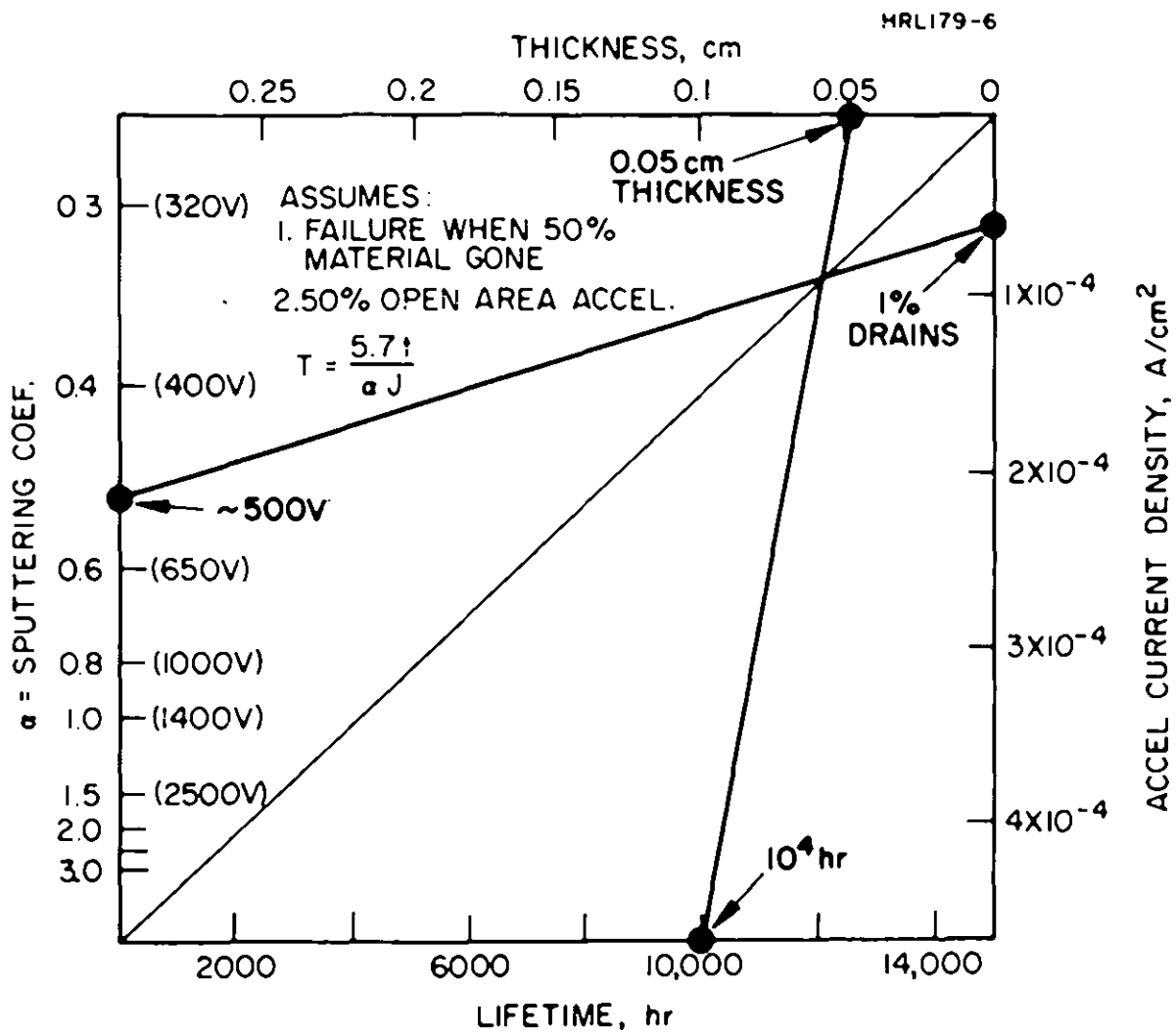


Fig. 20. Nomograph to estimate effect of charge exchange sputtering on electrode lifetime.

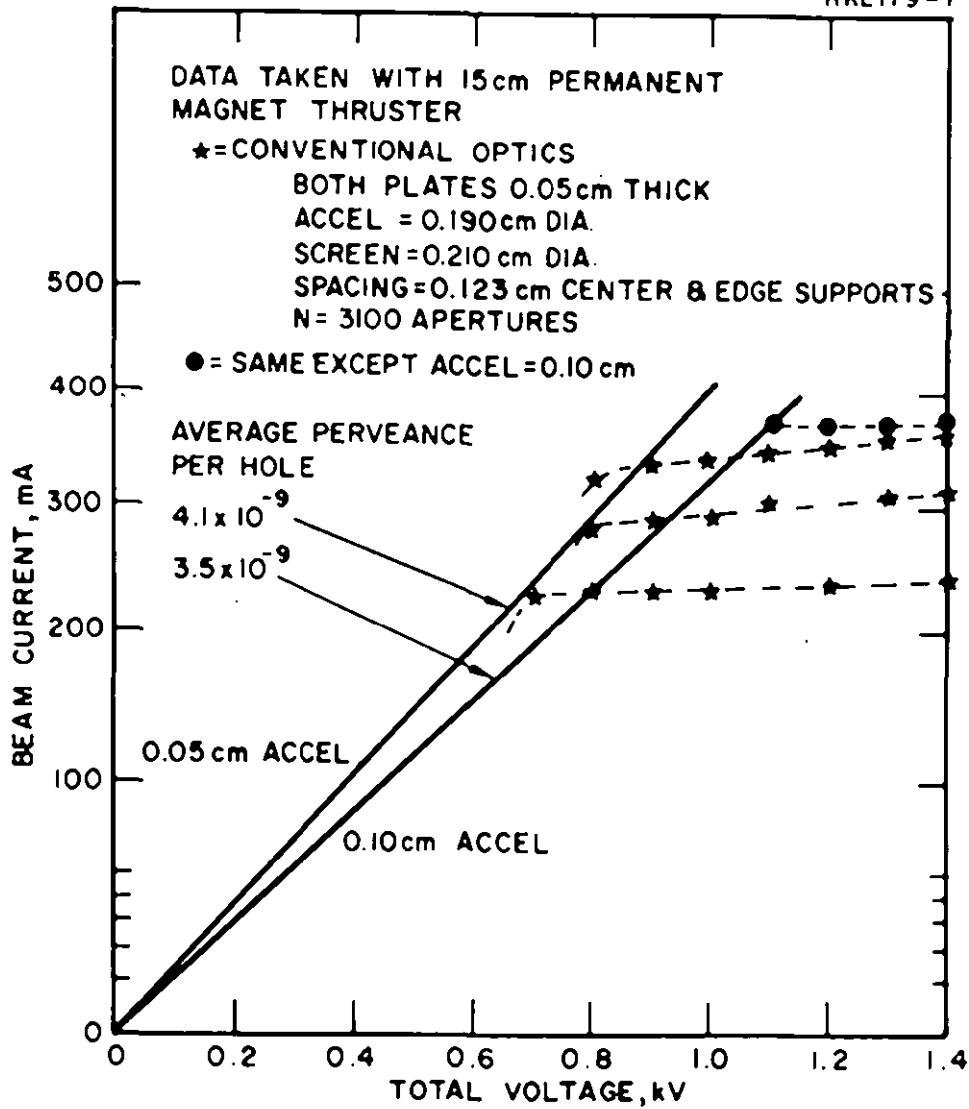


Fig. 21. Perveance data for 15 cm conventional optics.

electrodes with smaller holes (0.12 cm spacing; 0.213 cm apertures), made on a 15 cm thruster as part of this program, indicate that an average perveance of 4.1×10^{-9} can be achieved in the voltage range of interest here (see Fig. 21). Reference to Fig. 14 illustrates that a value of 3×10^{-9} or greater will be satisfactory for the design at hand.

3. Methods of Manufacture — Molybdenum is generally chosen as the electrode material because of its high temperature strength, high conductivity, low sputtering coefficient, and reasonably good workability. Several possible techniques have been considered for perforating the electrode which will require more than 10^4 apertures in a 30 cm diameter circle. The simplest, and first attempted, technique was to punch the material. This technique proved unsatisfactory because the hole spacing was irregular and delamination of the electrode material resulted. The internal stresses set up by punching and the upper limit on material thickness were also undesirable. An alternative method was to drill the holes with a numerically controlled drill. This technique is more costly and does not completely solve the problem of internal stresses created as the material is worked. It was also found that it was difficult if not impossible to hold the necessary tolerances on hole diameter and hole spacing, even with a numerically controlled drill. The only satisfactory technique was to drill the plates as a matched pair so that they would be aligned for at least one orientation. Perhaps the most promising technique established to date is chemical milling. This technique has not introduced additional stresses; it is relatively economical after a master has been made, and is accurately reproducible. Its principal difficulties are (1) it can be used effectively only on relatively thin material, which means that using it in the fabrication of a 30 cm accelerator would require a difficult laminar assembly of two or more layers, and (2) the apertures produced are countersunk from each side due to the etching process.

4. Conventional Optics Design — The 30 cm conventional ion optical system design shown in Fig. 22 uses the various measured and calculated parameters discussed above. The screen and accelerator were matched drilled from 0.075 and 0.125 cm arc cast molybdenum plates, respectively. The electrodes were drilled rather than chemically milled to assure that the cross section of the apertures was accurately defined. The screen was electropolished after drilling, to increase the screen open area and to radius the sharp corners produced by drilling. The final hole dimensions were 0.19 cm

M 7074

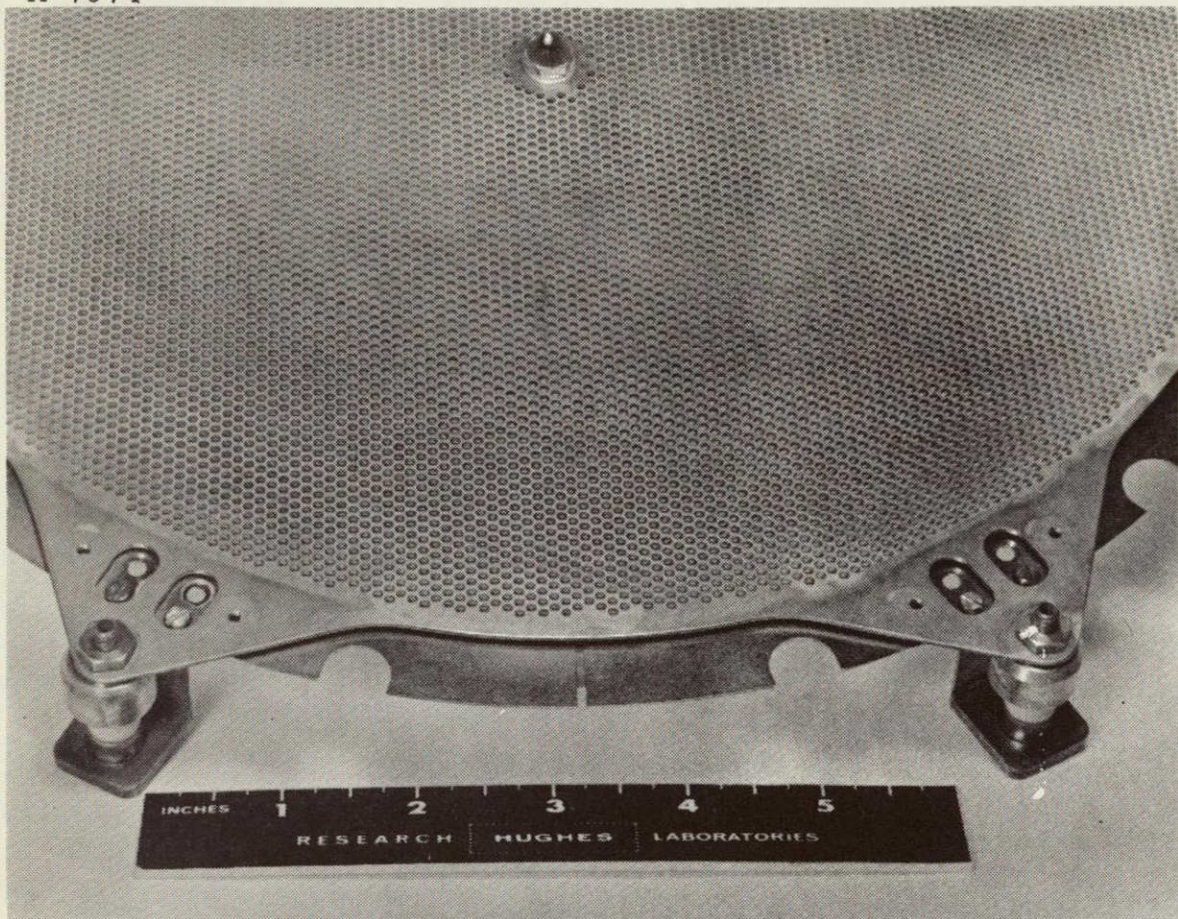


Fig. 22. 30 cm high perveance conventional ion optics system.

in the accelerator and 0.20 ± 0.01 cm in the screen, thus providing a screen open area of $\sim 62\%$. Center-to-center spacing is 0.25 cm. The interelectrode spacing was adjustable by shimming the mounting supports.

The screen electrode was supported on the thruster under radial tension. The accelerator is mounted to provide some radial compliance to minimize mechanical loading if the electrodes are at different temperatures. A single, centrally located, interelectrode support was used to define the interelectrode spacing on the center line. It is desirable to minimize such supports both to reduce the opaque area of the screen and to place the minimum radial constraint on the electrodes.

c. Insulated Optics

1. Introduction - Insulated optics are defined as those consisting of a single metal accelerator electrode which is coated on the plasma side with a layer of insulating material. The surface charge buildup on this insulator by the plasma acts as a virtual screen electrode to provide the necessary conditions for extracting and focusing the ion beam. A primary advantage of such a system is that the alignment and spacing between the virtual screen and the accelerator are fixed and are independent of any thermomechanical stresses induced in the electrode. The disadvantage of the system is that fabrication involves a new technology that is not well developed. The procedure for applying this insulating coating is discussed elsewhere in this report.

2. Design Criteria - In contrast to the conventional ion optical systems that had been used for many years, reliable test data for insulated optics were virtually unavailable at the start of the contract period. In order to meet the contract schedule, it was necessary to carry out a simultaneous design, fabrication, and test program to determine a functional 30 cm design. As soon as the fabrication procedures were adequate to produce functional hardware, several 15 cm electrodes were fabricated and tested to measure the perveance. The original data are shown in Fig. 23. Data also were taken with a larger aperture electrode (0.27 cm diameter on 0.32 cm spacing). Operation was erratic near the perveance line because of electron backstreaming from the neutralizer. While it was speculated that a thicker insulating coating would permit stable operation, it was concluded that a design of the type shown in Fig. 23 would provide a more reliable starting point for the 30 cm design.

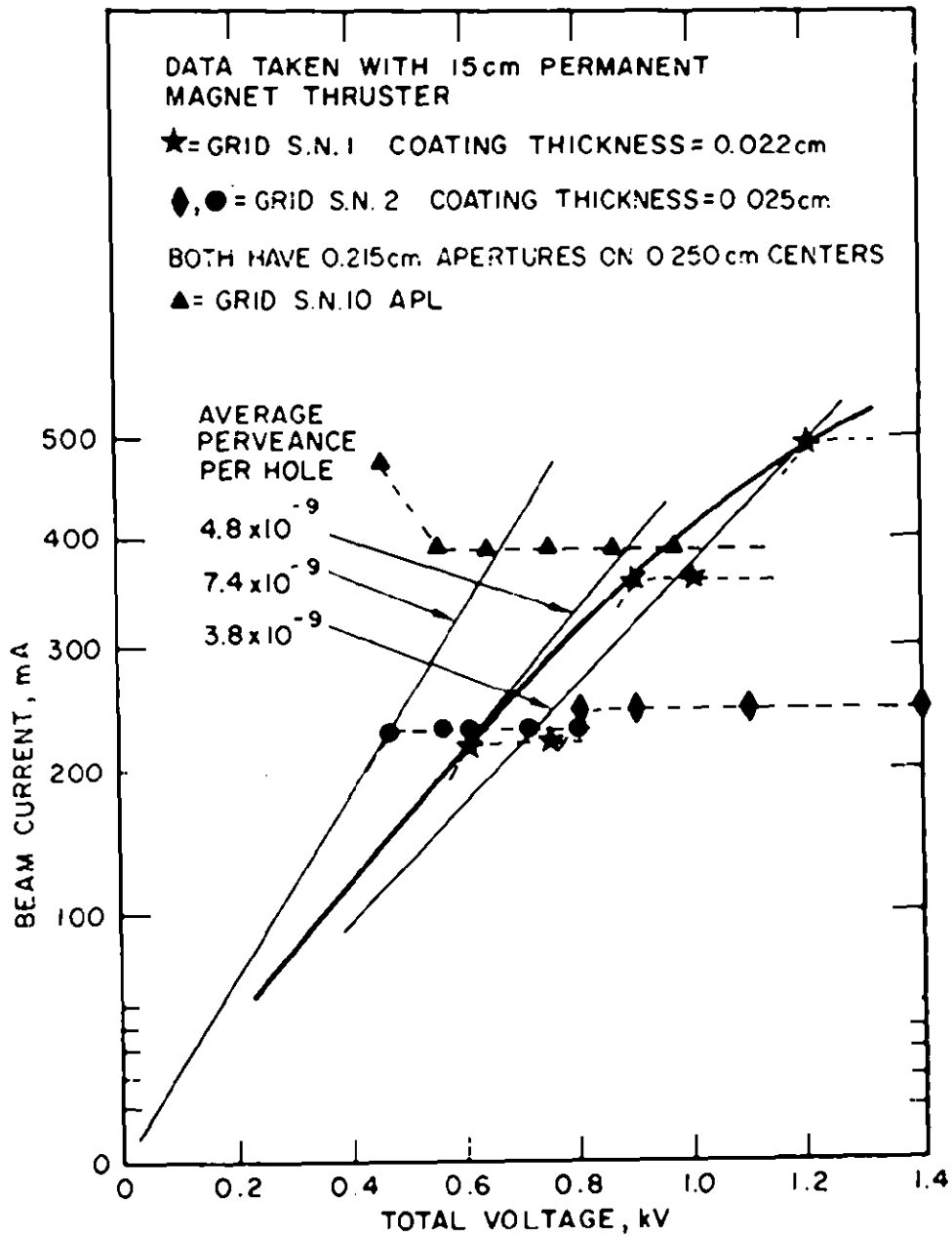


Fig. 23. Perveance data for 15 cm insulated optics.

It is also necessary that the chosen design operate in the voltage range required to produce the desired specific impulse. This constraint means that the insulating coating must sustain the total extraction voltage without appreciable current leakage or breakdown; this requires a dielectric strength of the order of 40,000 to 60,000 V/cm.

It is important that both the surface and volume resistivity be high because of the geometry. For a 30 cm electrode with 70% open area (i.e., 212 cm² opaque area) with 14,000 apertures of 0.190 cm in diameter, these quantities may be estimated as follows:

$$\begin{aligned}\text{Volume resistivity} &= R_V = \rho_V t / A \\ t &\equiv \text{thickness} = 0.05 \text{ cm} \\ A &\equiv \text{area} = 212 \text{ cm}^2 \\ \rho_V &\equiv \text{volume resistivity} \\ &\sim 10^6 \Omega\text{-cm at } 20^\circ\text{C} \\ &\sim 10^8 \Omega\text{-cm at } 300^\circ\text{C};\end{aligned}$$

therefore,

$$\begin{aligned}R_V &= 2.4 \times 10^{12} \Omega \text{ at } 20^\circ\text{C} \\ &= 2.4 \times 10^4 \Omega \text{ at } 300^\circ\text{C}.\end{aligned}$$

$$\begin{aligned}\text{Surface resistance} &= R_S = \frac{t}{c} \frac{\rho_S}{N} \\ t &\equiv \text{thickness of coating} \\ c &\equiv \text{circumference of single hole} = \pi d \\ N &\equiv \text{number of holes} = 14,000 \\ \rho_S &\equiv \text{surface resistivity} \\ &\sim 10^{15} \Omega/\square \text{ at } 20^\circ\text{C}.\end{aligned}$$

The surface resistivity is strongly dependent on the surface conditions and history. Presumably it will always be less than the above value, quoted in the Corning Glass Handbook No. B-83 for clean dry borosilicate glass at room temperature; therefore,

$$R_S \leq 6 \times 10^9.$$

Several conclusions may be drawn from these calculations:

1. Surface leakage probably will be larger than volume leakage by several orders of magnitude. This result is consistent with voltage breakdown tests on the material sample, where it has been observed that the breakdown path is invariably over the surface of the coating to the metal rather than through the insulating layer.
2. Using the higher (but more accurately known) volume resistivity at an operating temperature of 300°C, the leakage current for the 30 cm thruster is

$$I = \frac{1500 \text{ V}}{2.4 \times 10^4} = 6.25 \times 10^{-2} \text{ A.}$$

Thruster tests made later in the program typically showed accelerator currents of 10^{-2} A for a clean new electrode, ultimately rising to approximately 7×10^{-2} A in a few hours. A possible interpretation of this is a combined surface plus volume resistivity of $1.5 \times 10^5 \Omega$, which gradually decreases as the surface is contaminated by sputtered or condensed material (this is always observed on the insulating surface after a few hours of operation).

3. The above mechanism can account for a large fraction of the observed leakage currents in this type of system. Although they are undesirable from the standpoint of electrical efficiency, such currents are not destructive (as they would be if they arose from charge exchange or direct interception). Kerslake,⁹ however, has postulated an upper limit to such permissible currents; he has shown that a runaway condition can arise as a result of the drop in volume resistivity associated with the temperature rise at locations where resistance heating of the insulating layer is excessive. This failure mode has not been observed in tests at HRL, probably as a result of the limited capacity of the accelerator supply used.

4. An additional experimental observation is that the drain currents to the accelerator are a function more of the beam current than of the beam voltage. This result is consistent with the fact that the plasma sheath moves forward at the higher plasma density and shortens the surface conduction path, and also with the fact that the number of ions extracted from the plasma which are not focused through the aperture (i.e., those which impinge on the insulating surface) may be increased.

3. Methods of Fabrication

(a) Accelerator electrode. The accelerator electrode is perforated by chemically milling the apertures in a molybdenum sheet. This technique accurately reproduces the pattern of the original master, maintaining uniform spacing between the apertures. This is essential to the application of a uniform coating. Visual inspection of the flatness of the finished piece and photomicrographs of a section of an electrode after milling indicate that no appreciable stresses are introduced by this machining process.

Following perforation, the electrode is "dished" to improve stability. Using a technique originated at LeRC, it has been demonstrated that these electrodes can be readily formed by cold forging. Following forging the part will be stress relieved at a temperature 50°C higher than that which will be encountered in firing the refractory coating (1100 to 1150°C)

The piece is then electropolished to remove the sharp corners over which the insulating layer must be applied. Typically an electrode which was originally 0.050 cm thick perforated with 0.188 cm diameter apertures is reduced in thickness to 0.045 cm and the apertures will be enlarged to 0.208 to 0.213 cm. Following a light sandblast to remove the sheen left by the electropolishing, the electrode is washed with detergent, rinsed, air dried, and is then ready for coating.

(b) Application of insulating coating.* A substrate slurry (MCR-1K) is prepared from fused mullite, Ferro Corporation No. 3249 frit and enamel clay in the proportions 19.5:4:1. This is mixed with a small quantity (~ 0.1% by

* See Appendix I for more detail.

weight) of sodium nitrate and distilled water, and ball milled to mix and grind the material. The viscosity and specific gravity are adjusted to achieve the correct spraying and adhesion properties by the addition of distilled water. The material is sprayed onto the electrode with a nitrogen driven spray gun, air-dried, and visually inspected with low power microscope to assure a smooth, even coat. If the coating is not satisfactory, it may be washed off and reapplied.

The electrode is fired at 1100°C for 30 min in an argon atmosphere (1 psig) in an rf furnace. Proper coupling is achieved by placing a 1.25 cm thick graphite susceptor between the electrode and the rf coil. The cooling period after firing is approximately 1 hour. The refractory subcoat may be built up to the thickness desired by applying more 0.0125 to 0.025 cm thick layers in the above manner.

The filler coating (MF-4A) is applied in the following manner. Silica, boric acid, alumina, magnesium oxide, and calcium carbonate in the ratios of 100:268:69:63:33 are dry mixed and fired at 1450°C. The mixture is quenched in water and dried. It is next crushed and combined with enamel clay (9%), sodium nitrite, and water and ground for 6 hours. The mixture is then sprayed over the subcoat and fired in the same atmosphere as above at 1025°C for 30 min.

The final surface coat (MC-1) is principally Ferro No. 3249 frit with 4% enamel clay added. This coating is ground for 4 hours, applied in the same manner as the filler glass, and fired at 950 to 1000°C for 30 min.

It is generally necessary to remove small quantities of glass from the downstream face of the electrode with fine emery cloth.

The following parameters were measured for a sample prepared in the above manner:

Layer Number	Coating	Accumulated Thickness, cm	Voltage Breakdown in Air, kV
1	MCR-1K	0.0125	0.8
2	MCR-1K	0.0460	1.2
3	MF-9A	0.0460	1.5
4	MC-1	0.0530	1.9

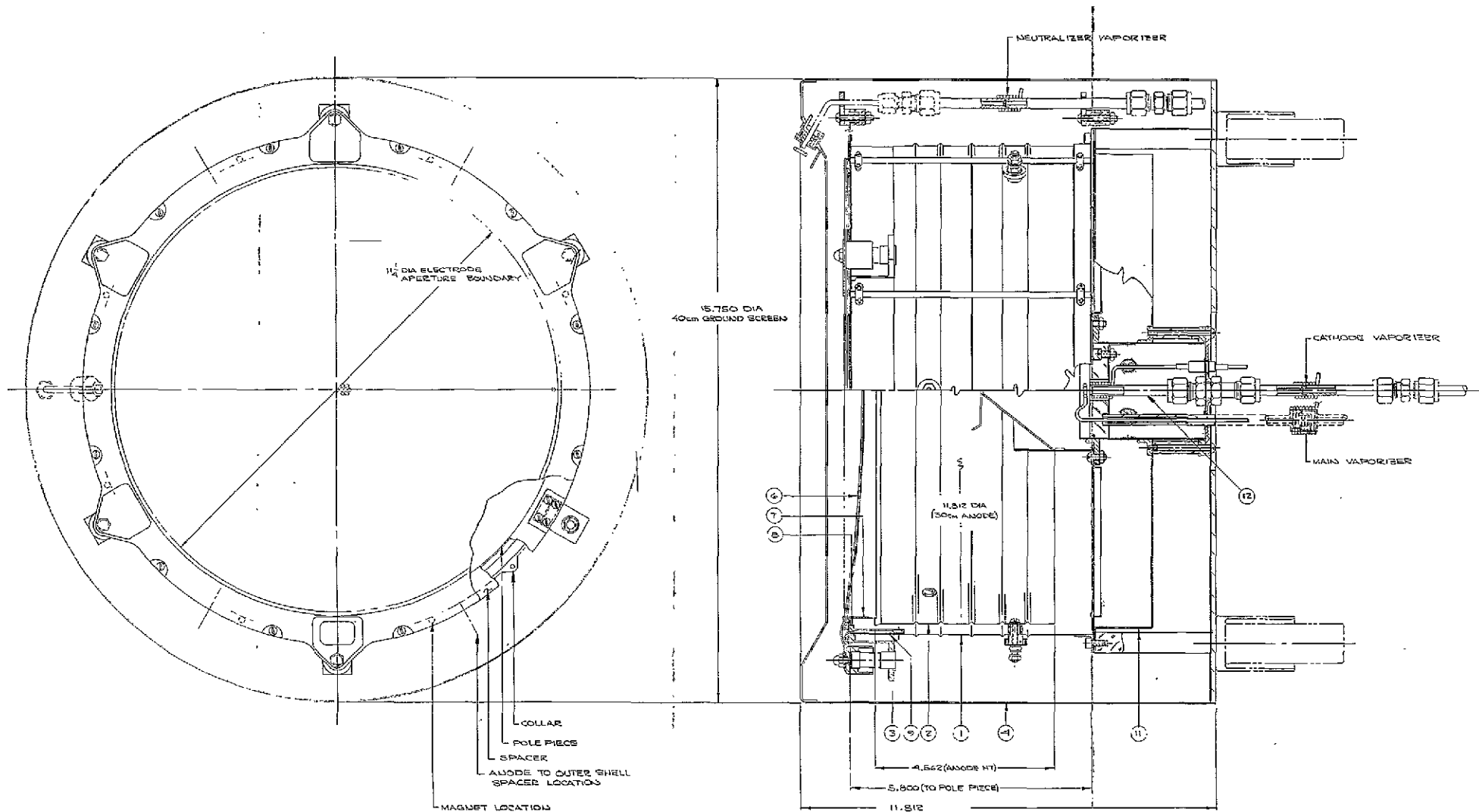
4. Insulated Optics Design - The insulated optics design detail is shown in Fig. 24. The base material is 0.051 cm thick arc cast molybdenum perforated by chemical milling with 0.190 cm diameter holes on 0.254 cm centers. The current handling capabilities of the type of structure were illustrated in Fig. 23 for a 15 cm diameter thruster. Novel features of this design are that the electrode is dished prior to coating and the structures which support the electrode keep it under radial tension to minimize thermal distortion.

A photograph of the finished grid is shown in Fig. 25, along with a cross section of the electrode and glass laminate. A section of the electrode after operation (shown in Fig. 26) illustrates the effective open area of the structure.

The data and calculations presented above indicated that this electrode system would fully meet the design goals of the contract. Experiments with the 15 cm diameter thruster indicate that a minimum negative accelerator voltage of 250 V is required to prevent electron backstreaming and that a maximum total voltage of 1500 to 2000 V should be achievable. These values include the design values of + 1000 V, -500 V used in all the above calculations. The minimum accelerator voltage (~ 250 V) may be used to reduce the energy of charge exchange ions and to decrease the beam spread if desired.

d. Ion Optics Evaluation with 30 cm Thruster

The studies described in the previous sections indicate that ion optical systems of both conventional and insulated designs can be designed and fabricated to fulfill the contractual goals of 1.85 A of ion beam at a net voltage of 1.0 kV. Therefore, it was valuable to compare the two systems experimentally on the same 30 cm thruster to establish the relative merits of each. Because of the financial limitations of the program and the long lead time to procure the perforated molybdenum sheet and fabricate the electrodes, it was possible to test only one of each type of optical system. The designs were thus somewhat conservative to assure that performance data for each system would be collected. The specifications for the final hardware are given below.

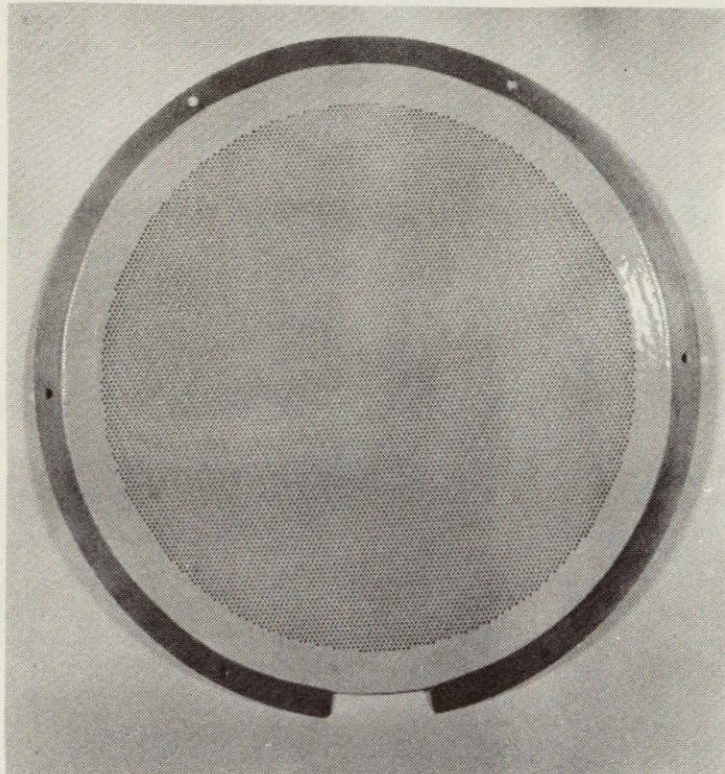


FOLDOUT FRAME -1

Fig. 24. 30 cm insulated ion optics design.

FOLDOUT FRAME -2

M 7053



M 7067

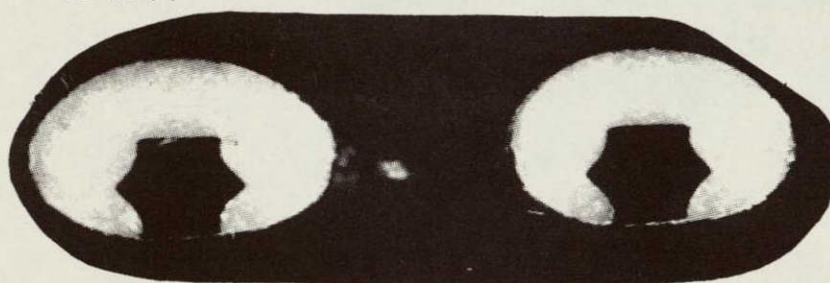


Fig. 25. Photographs of finished insulated ion optical system.

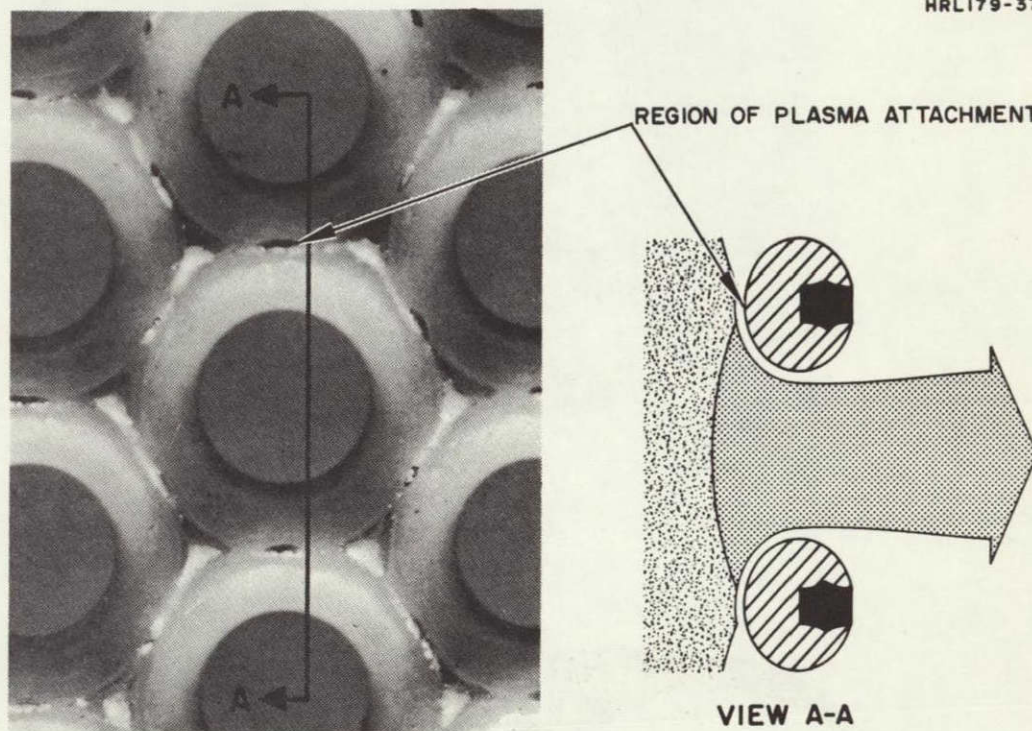


Fig. 26. Photograph of insulated ion optics after operation, showing plasma attachment.

1. Conventional Optics

Test 1

Screen

thickness	0.075 cm
apertures	0.20 cm
open area	62%

Accelerator

thickness	0.125 cm
apertures	0.19 cm

Center-to-center aperture spacing	0.250 cm
--------------------------------------	----------

Electrode spacing

test 1A	0.165 cm
test 1B	0.115 cm

Test 2

Same as Test 1, with screen electrode thickness reduced to 0.045 cm.

Test 3

Task 1 high specific impulse optics with inter-electrode spacing reduced to 0.100 cm.

Screen

thickness	0.075 cm
apertures	0.400 cm
open area	72%

Accelerator

thickness	0.250 cm
apertures	0.320 cm

Center-to-center aperture spacing	0.450 cm
--------------------------------------	----------

Electrode spacing	0.100 cm
-------------------	----------

Note: All systems had a single, central, interelectrode support.

2. Insulated Optics

Accelerator

thickness	0.05 cm
apertures	0.20 cm
Center-to-center aperture spacing	0.25 cm
Insulating coating	0.04 to 0.05 cm
Aperture diameter after coating	0.10 to 0.15 cm
Electrode shape	flat

Test 1 with conventional optics and the test of the insulated optics were conducted with the discharge chamber used to run the Task II design verification test. Further tests with conventional optics (tests 2 and 3) were run with the slightly modified chamber used to run the 500 hour endurance test, which used insulated optics. Direct comparison between the performance of the conventional and insulated optics is therefore available in each case.

The test results are summarized in Table VI and in Figs. 27 and 28. While these data are virtually self-explanatory, several conclusions may be emphasized here.

1. The perveance of the insulated optics is much higher than that of any conventional system tested. With the insulated optics the desired 1.85 A beam current is achievable with a total extraction voltage of 1500 V, while the conventional optics require ~ 3500 V.
2. The discharge chamber performance is considerably better with the insulated optics than with conventional optics. Two effects are responsible for this difference. By their very nature the insulated optics have a high percentage open area and a thin effective screen electrode. As a result of structural limitations, neither of these desirable features was achieved in the Test 1 conventional design. After the structural integrity of the design was demonstrated in Tests 1A and 1B, the screen thickness was reduced by almost a factor of two. Although part of the

TABLE VI

Summary of Ion Optical System Performance

V_+ , kV	I_+ , A	V_- , kV	I_- , mA	V_D , V	I_D , A	Total ^a Hg Flow, Equiv. A	η_m dischg, %	eV/Ion ^a dischg
Conventional test 1A (0.20 cm aperture, 0.075 cm thick screen, 0.165 cm spacing)								
1.6	2.00	2.00	14	44	21.0	2.16	80.3	485
1.0	1.50	1.95	12	43	17.0	2.16	76.0	432
1.0	1.42	1.95	12	42	14.6	2.16	70.6	374
1.0	1.32	1.95	12	41	12.0	2.16	68.5	342
Conventional test 1B (same as 1A, with spacing reduced to 0.115 cm)								
1.0	1.60	1.98	20	36	19.0	2.20	73	430
1.0	1.56	1.90	20	35	18.2	2.20	71	415
1.0	1.45	1.90	19	34	17.0	2.20	66	405
1.0	1.34	1.90	18	33	15.6	2.20	61	385
Conventional test 2 (same as 1B, with screen thickness reduced to 0.045 cm)								
1.34	1.8	2.0	13	40.2	15.6	—	—	—
1.0	1.50	2.0	16	41.3	15.0	1.615	95.3	417
1.0	1.440	2.0	14	39.0	12.7	1.615	91.5	347
1.0	1.340	2.0	14	37.0	10.0	1.615	85.1	279
Conventional test 3 (0.40 cm apertures, 0.075 cm thick screen, 0.100 cm spacing)								
1.0	0.95	1.00	77	38.2	8.6	—	—	346
2.7	1.70	1.00	17	35.0	12.7	1.880	94.3	264
2.7	1.60	1.00	16	33.0	10.2	1.880	88.5	212
2.7	1.41	1.00	17	31.0	8.5	1.880	78.0	189
Insulated optics (0.05 cm thick screen, 0.05 cm thick coating, 0.20 cm apertures)								
Task II Preliminary Test								
1.0	1.89	0.85	30	50	11.0	2.14	90.5	295
1.0	1.79	0.77	30	47	9.8	2.14	85.5	257
1.0	1.74	0.80	30	46	9.0	2.14	83.0	242
1.0	1.65	0.80	30	44	8.0	2.14	79.0	220
Task II Design Verification Test								
1.0	1.59	0.64	40	35.4	9.8	2.01	86.5	218
Task III Design Verification Test								
1.0	1.87	0.50	63	37.2	12.5	2.15	88.2	249
Task IV Endurance Test								
1.0	1.904	0.4	50	40.9	8.6	2.06	93.4	190
^a Includes mercury flow through main vaporizer, hollow cathode, and plasma bridge neutralizer.								

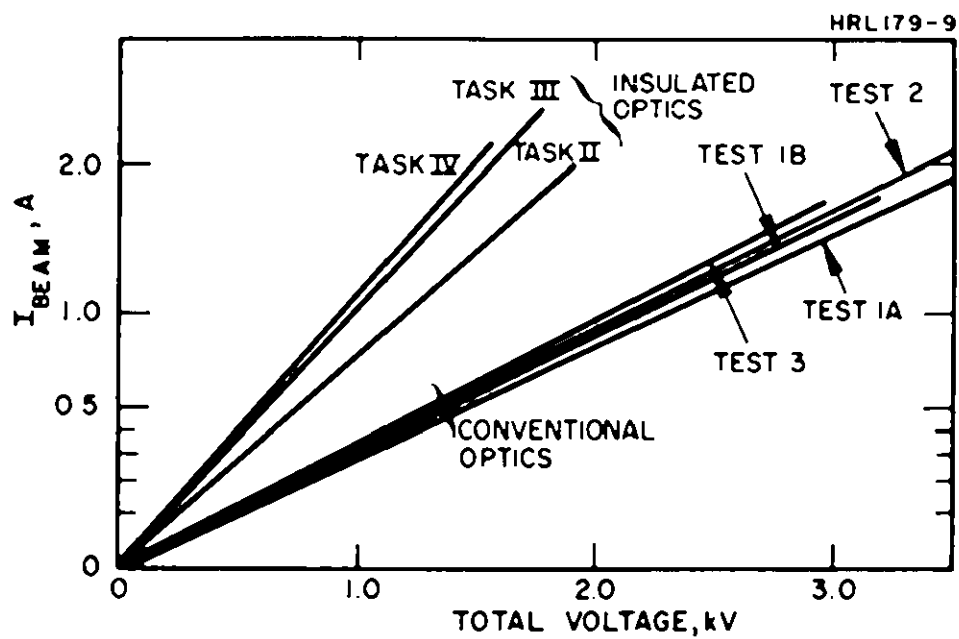


Fig. 27. Pervance of 30 cm optics listed in Table VI.

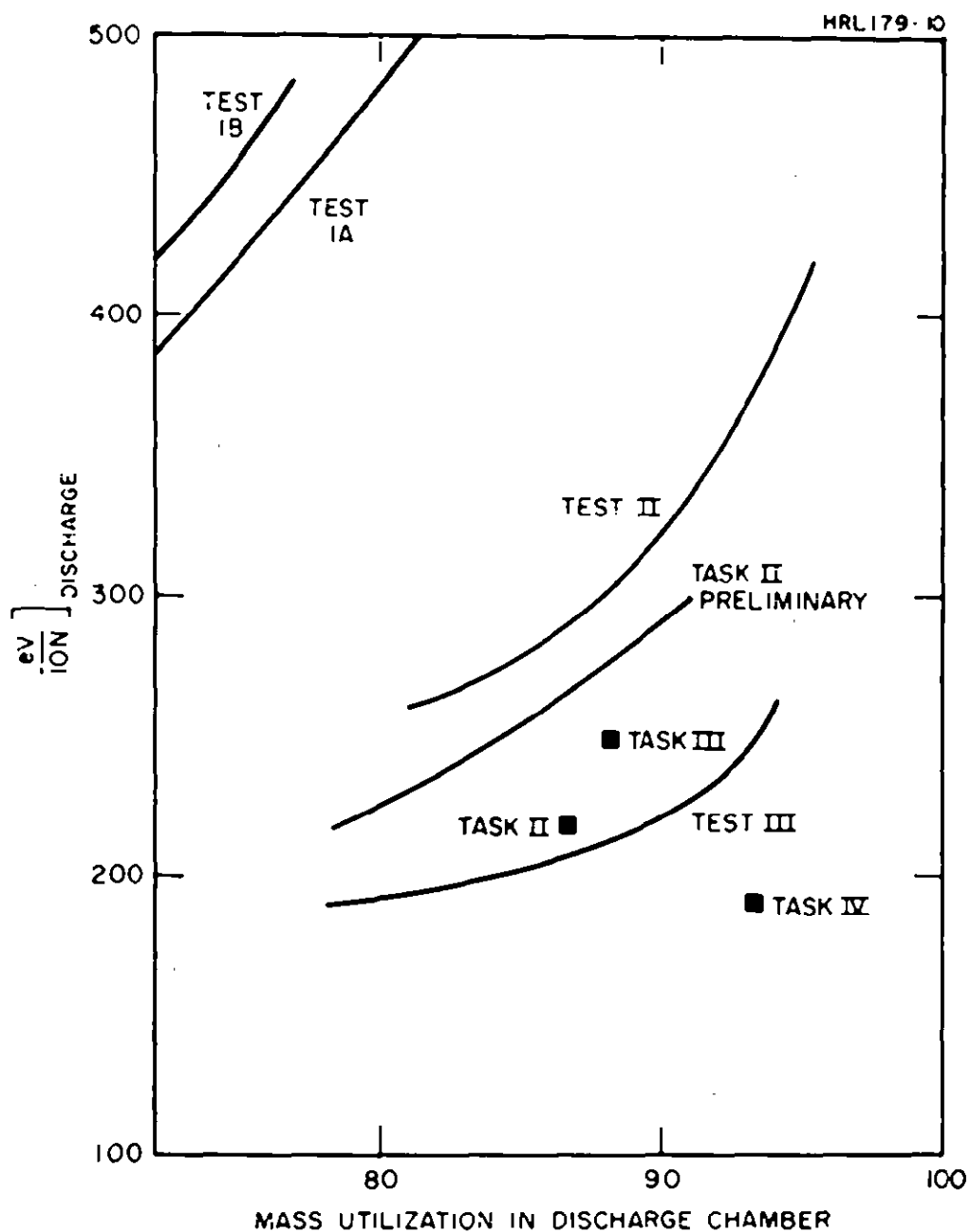


Fig. 28. Discharge chamber performance with ion optical systems listed in Table VI.

resultant performance improvement must be attributed to an improved discharge chamber design, for the second test it may be clearly seen that the thinner screen improves the discharge chamber performance. With the center-to-center aperture spacing used here (0.250 cm), it is not possible to exceed 62% open area without losing structural integrity because the thickness of the web between apertures is reduced to less than 0.05 cm. The effect of open area may be seen by comparing Tests 1 and 2 with Test 3. In the last the open area was 72%, compared with 62% in Tests 1 and 2. The perveance was not improved, but the rather meager data for Test 3 indicate that the discharge chamber losses were significantly reduced.

3. While not shown by the data, the conventional ion optical systems operated more stably, particularly in conjunction with the plasma bridge neutralizer. With the insulated optic it was often very difficult to recover from an arc because a discharge would strike between the neutralizer and the anode. This discharge could not be extinguished by applying greater negative accelerator voltage because the large currents which would then flow could damage the grid. This problem was finally alleviated, as discussed in Section III-B-5, by adding more energy storage to the accelerator circuit.
4. The accelerator drain currents were typically lower with the conventional system. This occurs because the drain currents here result primarily from charge exchange only, while leakage currents predominate in the insulated system.

The final choice of ion extraction system was based on the data shown in Figs. 27 and 28. The insulated ion optics met both the efficiency and perveance requirements set by the contract goals, while the conventional system fulfilled neither (except at a high accel-decel ratio).

2. Discharge Chamber Development

This section deals with the discharge chamber modifications which were necessary to permit the scaled 30 cm diameter thruster, developed in the early part of the program, to meet the performance goals for low specific impulse operation using the insulated, single grid ion extraction system described in Section III-B-1. The following goals were set by the contract:

1.	Input power	2.5 kW
2.	Electrical efficiency	74%
3.	Propellant utilization efficiency	87%
4.	Over-all efficiency	64%
5.	Specific impulse	2,750 sec
6.	Net acceleration voltage	1,000 V
7.	Thrust	0.026 lb.

Using the results obtained in the development of the high specific impulse thruster discharge chamber, and information supplied by members of the NASA LeRC staff, modifications of the following parameters were considered, evaluated, and tested:

1. Cathode geometry and location
2. Magnetic field configuration and intensity
3. Mercury propellant introduction mode
4. Ion chamber length-to-diameter ratio
5. Anode geometry and location
6. Neutralizer performance.

Before discussing individually the approach applied to each parametric variation, it should be noted that these parameters are not completely independent, and changing one parameter may affect the optimization of several others. Consequently, emphasis was placed on achieving the required performance levels with a minimum of thruster modification, since operation of the thruster discharge chamber developed for high specific impulse operation was already near the required performance levels when the thruster was operated with the single grid accelerator system (see Table II). The parametric variations pertaining to discharge chamber performance are discussed in detail below, while the cathode and neutralizer performance are discussed in later sections.

a. Cathode Location and Geometry

Development of the thruster hollow cathode geometry is described in a later section; however, the cathode location and baffle-pole piece configuration will be considered here. The cathode location was not varied from the conventional SERT-II configuration shown in Fig. 5. As described in the discussion of the high specific impulse thruster, the three factors which influence the emission capability of the hollow cathode for a fixed discharge voltage are

1. baffle to pole tip open area
2. magnetic field strength in the open area
3. neutral or ion density in the open area.

Two approaches were used to obtain favorable discharge voltage-current characteristics:

1. baffle diameter was varied
2. a variable magnetic field was applied across the baffle open area.

The latter approach is an application of a concept formulated under a previous contract (NAS 3-9703), and later successfully developed under a Hughes IR&D program, using a 15 cm diameter thruster. Because variation of the magnetic field in the baffle-pole piece open area has an effect on the electrons analogous to changing the baffle diameter, the implementation has been termed a variable magnetic baffle. Experiments with variations in baffle dimensions were carried out during tests of the ion extraction system to permit evaluation of the ion extraction system with the discharge chamber operated in a near-optimum voltage-current regime. Because the variable magnetic baffle concept required a significant variation in thruster geometry (see Fig. 29), a second discharge chamber was modified to perform these experiments in parallel with the optimization of the conventional design. The objective of baffle diameter modification was to achieve a ratio of discharge current to beam current on the order of 5, with cathode propellant flow on the order of 5 to 10% of the discharge chamber propellant flow, and with discharge voltage between 35 and 40 V. Figure 30 shows the baffle changes required to produce the desired discharge loss and voltage-current characteristics (thruster parameters are given in Table VII). While some of the change in performance observed in this figure can be attributed to the characteristics of the insulated grids used in the tests, the final choice of 5.7 cm diameter is consistent with Bechtel's¹¹ results. For 1.5 A beam current,

NRL.79-19

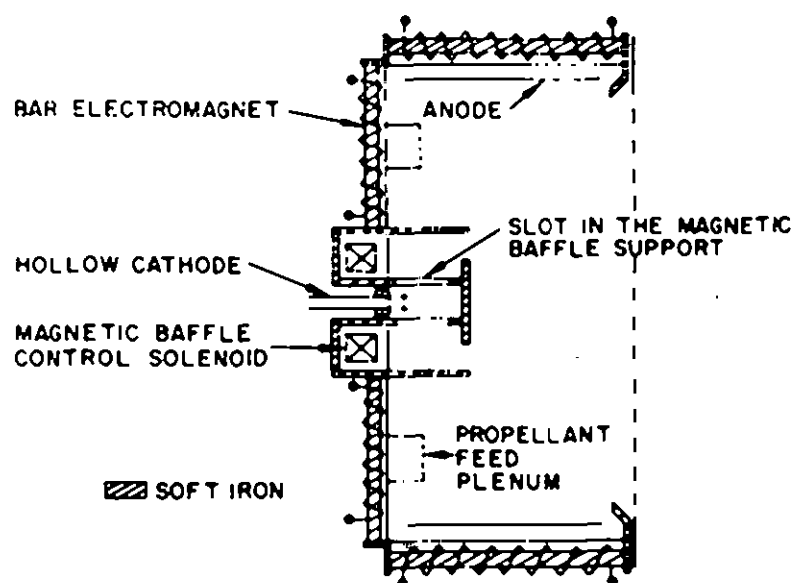


Fig. 29. 30 cm thruster configuration showing variable magnetic baffle geometry.

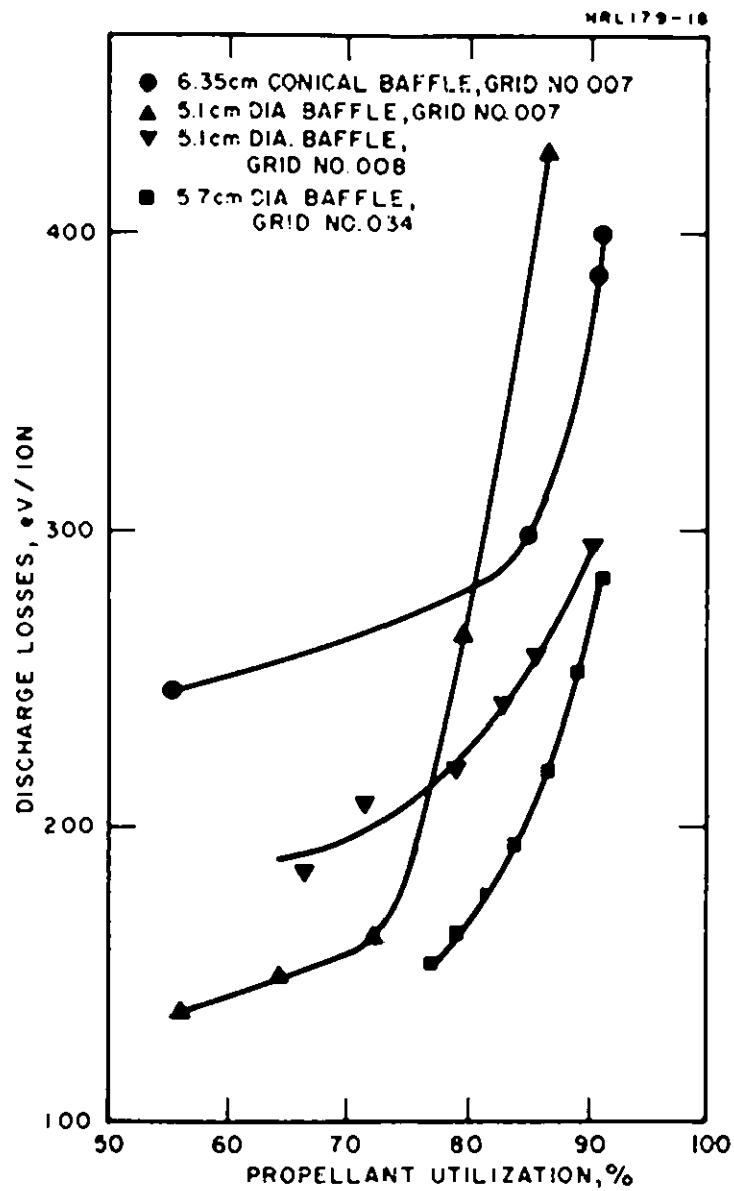


Fig. 30. Discharge chamber performance for several baffle and optic geometries.

TABLE VII

Thruster Parameters for Figure 30

Ion Extraction System - single, insulated grid SN 007 ● Baffle Geometry 6.35 cm diameter, conical										
V_{beam} V	I_{beam} mA	V_{acc} V	I_{acc} mA	V_D V	I_D A	I_{N1} mA (equiv.)	I_{N2} mA	I_{N3} mA	η_m %	E_I eV/ion
1000	548	500	12	48	2.8	850	147	997	88	246
↓	909	↓	31	37	9.5	850	↓	997	91	386
	816		24	39.5	9.4	700	↓	847	96	455
	773		27	36.5	8.5	↓	↓	↓	91	400
	720		30	33	6.5	↓	↓	↓	85	298
▲ Baffle Geometry 5.1 cm diameter, in plane of cathode pole tip										
1000	416	860	16	40	1.4	655	76	731	87	135
↓	485	↓	18	41.5	1.9	↓	↓	↓	66.5	163
	515		18	44.5	2.2	↓	↓	↓	70.5	190
	562		19	50	3.2	↓	↓	↓	77	284
	578	850	16	40	1.3	600	75	675	56	138
	436	↓	17	41	1.6	↓	↓	↓	64.5	150
	486	↓	17	43.2	1.95	↓	↓	↓	72	173
	516	↓	17	49	2.9	↓	↓	↓	79.3	266
	584	↓	18	52	4.8	↓	↓	↓	86.5	427
▼ Ion Extraction System - single, insulated grid SN 008 Baffle Geometry 5.1 cm diameter, in plane of cathode pole tip										
1000	1860	850	30	50	11	1860	200	2060	90.5	295
↓	1760	770	30	47	9.8	↓	↓	↓	85.5	257
	1702	800	38	46	9.0	↓	↓	↓	81	242
	1620	800	30	44.5	8.0	↓	↓	↓	79	220
	1447	800	33	43	7.0	↓	↓	↓	71.5	208
	1370	800	30	42.5	6.0	↓	↓	↓	66.5	186
■ Ion Extraction System - Single, insulated grid SN 034 Baffle Geometry - 5.7 cm diameter, in plane of cathode pole tip										
1010	1944	660	56	38.5	14.8	2040	97	2137	91	293
↓	1894	↓	56	37.2	12.8	↓	↓	↓	88.8	252
	1843		57	36.3	11.1	↓	↓	↓	86.5	218
	1793		57	35.5	9.8	↓	↓	↓	84	193
	1742		58	34.5	8.9	↓	↓	↓	81.6	176
	1690	↓	60	33.5	8.2	↓	↓	↓	79	163
	1639	↓	61	33	7.8	↓	↓	↓	77	154

Becktel found that a 5.1 cm baffle is optimum. His resultant baffle-to-pole diameter was 0.7, compared with 0.75 in our program, where the required beam current was 1.85 A. The increased current meant that either the baffle diameter must increase or the cathode propellant flow rate must decrease to maintain the discharge voltage in the desired range (in accord with Becktel Fig. 12). Decreasing the cathode propellant flow to less than 5% of the discharge chamber propellant flow is undesirable because the discharge becomes unstable and difficult to ignite. (It should be noted here that cathode propellant flow was manually adjusted to obtain the desired discharge voltage, and controlled at a constant value in proportion to temperature. Hence no provision was available to momentarily increase cathode propellant flow to facilitate discharge ignition or damp instability.) The data shown in Fig. 30 for the 5.7 cm diameter baffle were obtained with several noteworthy refinements in baffle support structure and cathode pole piece geometry. It was noted that the cathode pole piece was slightly out of round (2 mm difference in maximum and minimum diameter) and that it was difficult to repeat thruster performance characteristics after the baffle had been removed and replaced. It has been pointed out by both LeRC^{12,13} and HRL¹⁴ investigators that the effect of the baffle is "electrical" in nature and is therefore critically related to the baffle and pole piece orientation and spacing. This means that the baffle controls the flow of electrons from the hollow cathode to the discharge chamber by means of the electric and magnetic fields established by the pole piece and baffle as electrodes rather than mechanical obstacles for deflecting propellant flow or simple aperture limitation of electron flow. To position the baffle more precisely with respect to the pole piece, a machined support ring (aluminum) was forced over the pole piece to make it circular in cross section, and a baffle support structure was fabricated as shown in Fig. 31, using a fixture to insure the shape and facilitate duplication. This modification resulted in the improvement shown in Fig. 32 and enhanced the repeatability of experiments.

The variable magnetic baffle was found to be a valuable optimization tool in previous 15 cm diameter thruster experiments. The magnetic baffle was capable of controlling discharge voltage-current characteristics over a relatively large range of propellant flow ratios (between hollow cathode and discharge chamber). A direct scaling of the baffle dimensions to the 30 cm diameter thruster was not nearly as successful in producing the desired magnetic control capability. Performance

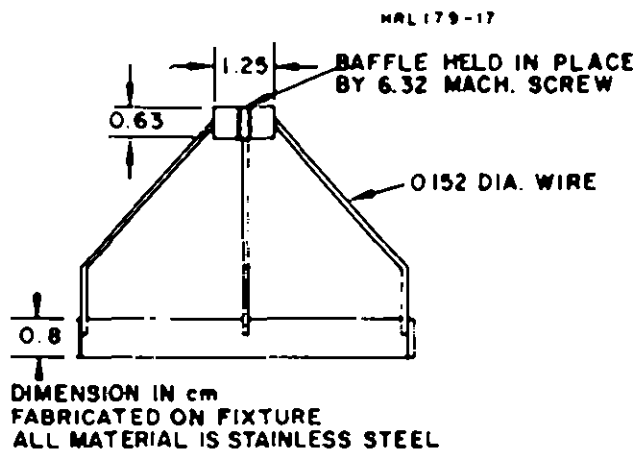
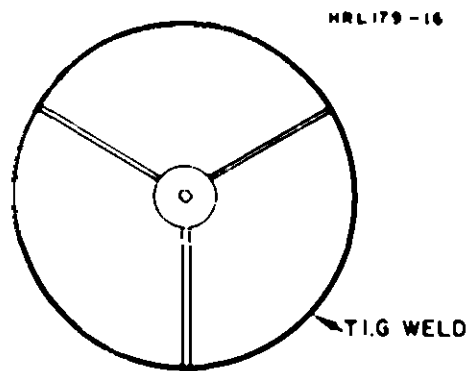


Fig. 31. Tripod baffle mount for
30 cm diameter thruster.

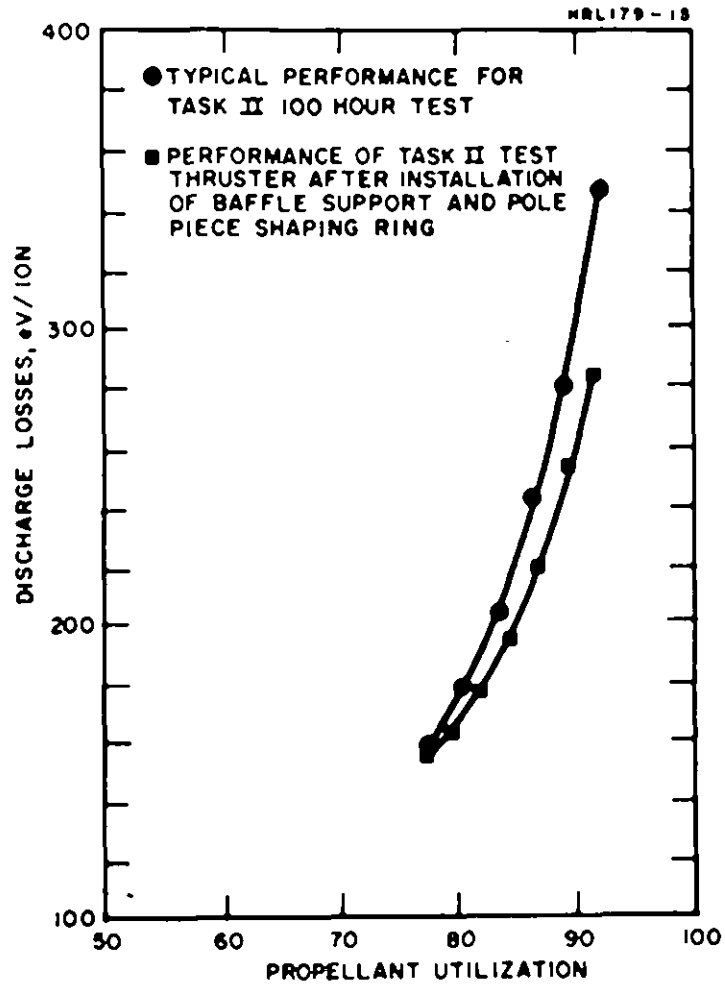


Fig. 32. Comparison of discharge performance before and after installation of pre-formed baffle support and pole piece shaping ring.

characteristics for the thruster shown in Fig. 29 are given in Fig. 33 for several levels of beam power (thruster parameters are shown in Table VIII). While these performance characteristics compare favorably with the fixed baffle thruster, they were obtained by varying the cathode propellant flow in addition to the baffle magnet current. Because it was necessary to adjust both cathode flow and baffle magnet, the variable magnetic baffle was of little value as an optimization tool in the configuration tested. It is believed that the dimensions of the magnetic baffle and pole piece must be nearer those of the conventional baffle and pole piece to obtain the desired control characteristics. Time was not available to explore this possibility.

b. Magnetic Field Configuration

Considerable care was taken in the development of the scaled high specific impulse thruster discharge chamber to generate a magnetic field geometry with suitably divergent field lines and the scaled field strength. The procedure used to develop the desired configuration was described in Section III-A-1. This magnetic configuration is generated using both radial and axial permanent magnets. For some of the ion optical system tests, the axial permanent magnets were replaced by bar electromagnets. The optimum axial magnet current was found to be very nearly the same as for the high specific impulse thruster. Discharge losses were found to be a rather sensitive function of axial magnet current near the optimum. Consequently, conversion to permanent magnets had to be done at least in part experimentally because the field maps (values) can never be exactly duplicated by replacing the bar electromagnets by permanent magnets. Figure 34 compares thruster performance for several combinations of axial and radial permanent magnets. No other variations in magnetic field strength or configuration were made in the low specific impulse optimization program. A mapping of the axial magnetic field values for this magnetic configuration is shown in Fig. 35. Although the 30 cm thruster developed by LeRC uses only axial magnets for generation of the magnetic field, it is probable that the field shape and strength are nearly the same.

c. Mercury Propellant Introduction Mode

As in the high specific impulse thruster discharge chamber, the propellant is injected into the discharge chamber directly and through the hollow cathode by means of two vaporizers to assure independent control of these two flow rates.

TABLE VIII

Data for Figure 33

Symbol ■ Main Flow - 1.82 A (equiv.) Cathode Flow - 0.159 A (equiv.) Magnet Currents - Side, 0.6 A; Back, 0.9 A; Baffle, 0.35 A $V_- = 1.0$ kV $V_+ = 0.66$ kV Cathode Heater Power 27 W; Keeper 2.65 W Neutralizer Heater Power 17 W; Keeper 2.3 W Vaporizer Power 19 W Total						
I_+ , mA	I_- , mA	V_D , V	I_D , A	η_m , %	E_I , eV/Ion	I_D/I_B
2000	33	41.1	13.9	99	290	7
1950	32	39.6	12.7	96.6	262	6.6
1900	32	38.9	11.9	94.2	248	6.3
1850	33	37.7	11.0	91.5	228	6
1800	35	37.0	10.3	89	216	5.8
1750	36	36.3	9.7	86.5	205	
1700	37	36.0	9.0	84	195	
1650	36	35.6	8.2	81.5	182	
Symbol ▼ Main Flow - 1.38 A Cathode Flow - 0.137 A Magnet Currents - Side, 0.5 A; Back, 0.9 A; Baffle, 0.5 A $V_- = 1.0$ kV $V_+ = 0.46$ kV Cathode and Neutralizer Powers Same as Above Vaporizer Powers 17.8 W						
1450	25	37.9	10.0	93.8	266	7
1400	26	36.9	9.0	90.5	241	6.6
1350	26	36.2	8.0	87.2	218	6
1300	26	36	6.8	84	192	
1250	27	36	5.5	80.5	162	
1210	30	36	4.9	77.7	150	

TABLE VIII (Cont'd)

Symbol ●						
Main Flow - 1.69 A						
Cathode Flow - 0.170 A						
Magnet Currents - Side, 0.5 A; Back, 0.9A; .						
Baffle, 0.56 A						
$V_- = 1.0$ kV						
$V_+ = 0.65$ kV						
I_+ , mA	I_- , mA	V_D , V	I_D , A	η_m , %	E_I eV/Ion	I_D/I_B
1850	16.5	46.0	10.0	98.5	251	5.3
1800	18	45.0	9.8	96	248	
1750	17.5	43.0	9.3	93	231	
1700	19	41.5	8.8	90.5	211	
1650	19	40.0	8.4	87.5	206	
1600	18	39.0	7.95	85	196	
1550	18	37.8	7.6	82.5	188	
1500	18	37.0	7.4	79.5	185	
1450	18	36.0	7.2	77	181	

Symbol ▲						
Main Flow - 0.98 A						
Cathode Flow - 0.145 A						
Magnet Currents - Side, 0.5 A; Back, 0.9A;						
Baffle, 0.08 A						
$V_- = 1.0$						
$V_+ = 0.65$						
1100	13.5	42	6.2	96	240	4.9
1050	12	40.8	5.1	92	200	
1000	15	39.2	4.6	87	183	4.7
950	16	38	4.1	83	167	
900	18	37	3.6	78	150	

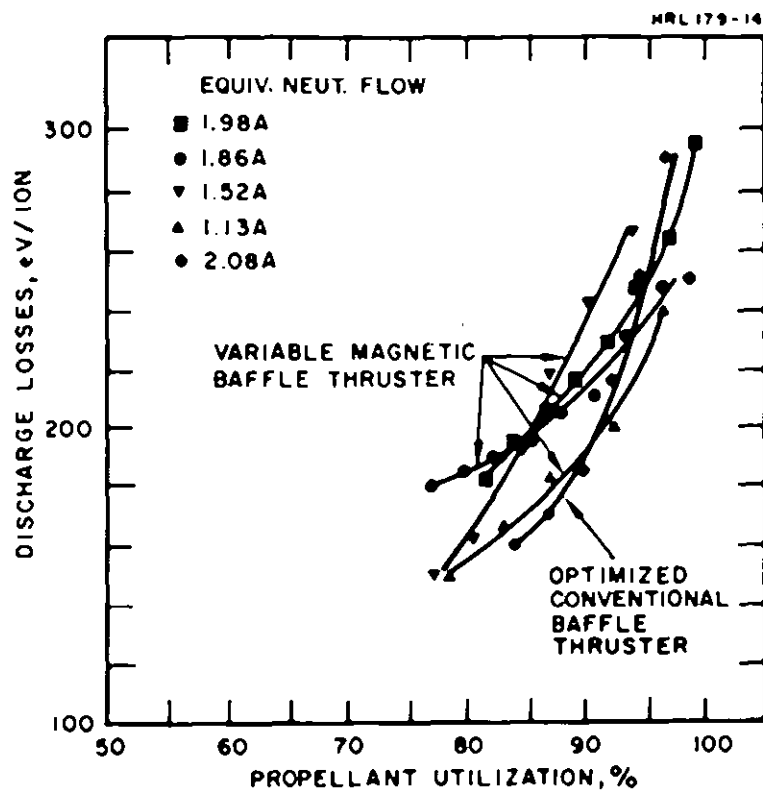


Fig. 33. Comparison of discharge performance mappings for the 30 cm diameter variable magnetic baffle thruster and the optimized conventional baffle thruster.

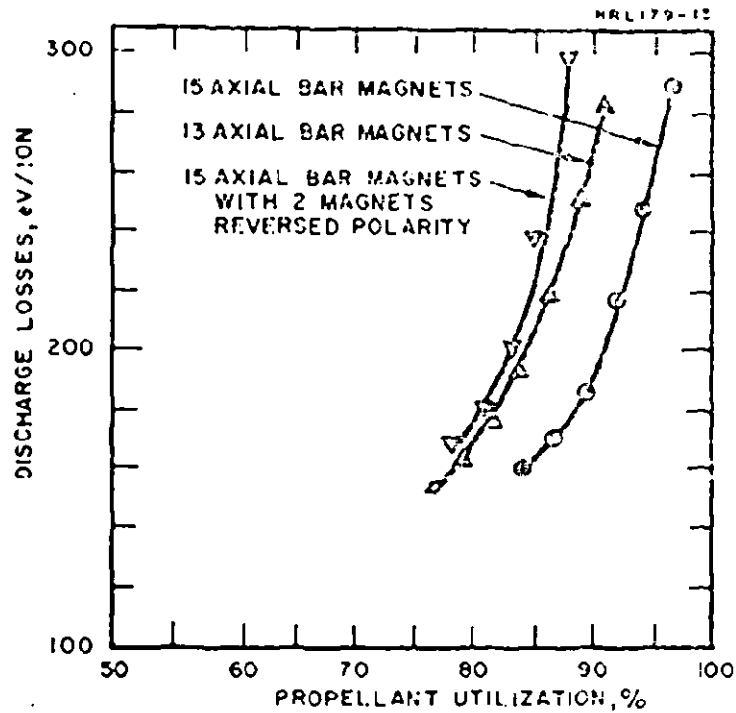


Fig. 34. Comparison of performance mappings for thruster operation with 13 and 15 axial bar magnets and 8 radial bar magnets.

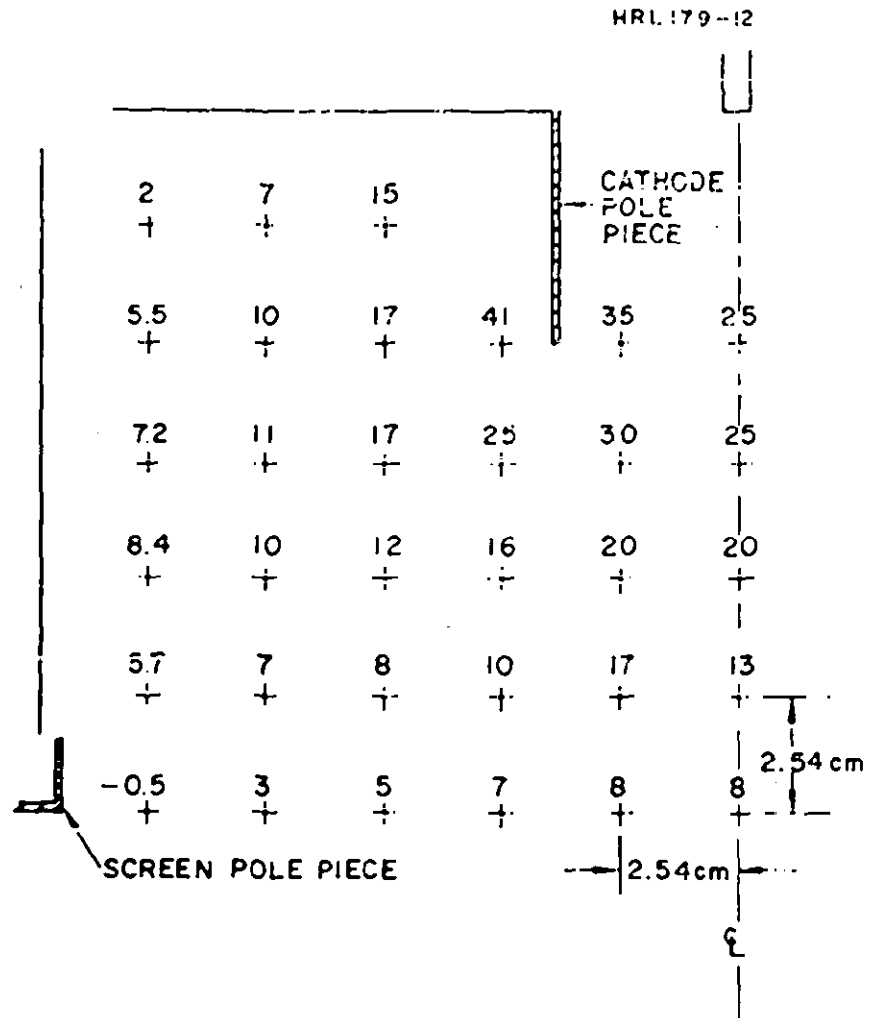


Fig. 35. Axial magnet field mapping for optimized magnetic configuration generate by 8 radial and 15 axial permanent magnets. Field values are in Tesla $\times 10^4$.

During this portion of the program the discharge chamber propellant plenum was modified as shown in Fig. 36, principally to facilitate radial magnet mounting and propellant electrical isolator mounting. Consequently the schematic thruster shown in Fig. 36 represents the optimized thruster discharge chamber.

d. Ion Chamber Length

In scaling from 15 cm diameter to 30 cm diameter it was shown that discharge chamber length should remain invariant. No variation of ion chamber was attempted after the scaling of the high specific impulse chamber proved successful. As stated above, radial magnets were installed to generate a sufficiently divergent magnetic field with this relatively small length-to-diameter ratio.

e. Anode Geometry and Location

The only modification in anode geometry attempted was the installation of an isolated electrode at the upstream boundary of the discharge chamber (i.e., approximately in the same plane as the cathode tip). This electrode could be alternately switched from anode to cathode potential during operation. The objective of this experiment was to determine whether ion loss could be diminished by operating more of the discharge chamber boundary at anode potential. The result was a nearly imperceptible increase in discharge current (about 1%) when the electrode was operated at anode potential. It is therefore concluded that most ion loss to the discharge chamber walls occurs at the cathode pole piece and baffle, the screen electrode and pole piece, or the anode.

f. Neutralizer Performance

Discussion of neutralizer optimization is deferred to a separate section which follows cathode development. The optimum neutralizer location and angle is shown in Fig. 36. In this position, the neutralizer propellant flow can be reduced to about 3 to 5% of the beam current value without loss of stability. At this propellant flow rate, there is no excessive sputtering erosion on the accelerator grid in the vicinity of the neutralizer.

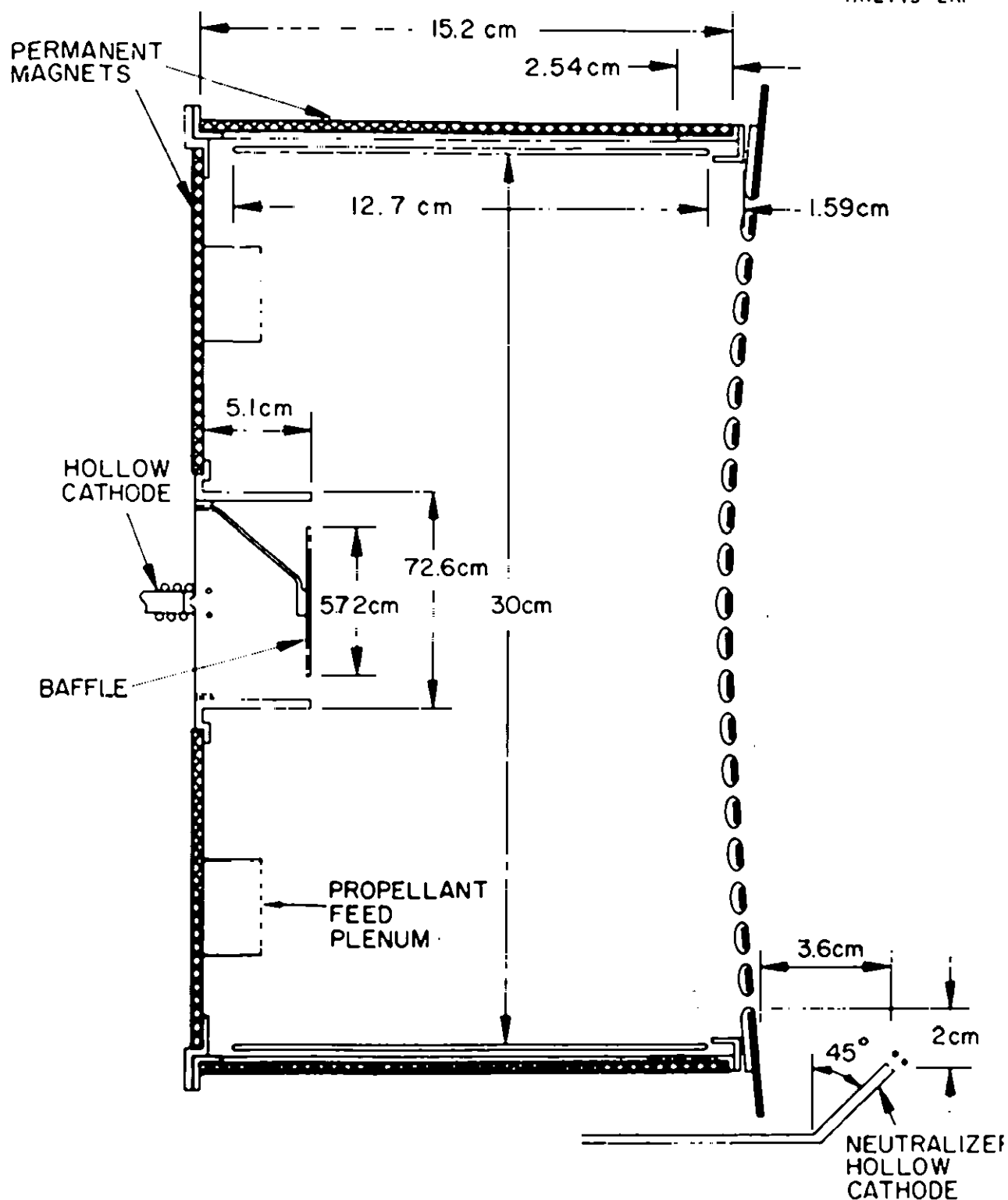


Fig. 36. 30 cm diameter thruster optimized for operation at 2.5 kW power, 2750 sec specific impulse.

3. Hollow Cathode Design

The goal of this task was to improve upon existing hollow cathode technology which was developed primarily for 15 cm size thrusters. The low requirement was for an efficient hollow cathode for use in 30 cm thrusters which could be easily restarted and have a projected lifetime of 10,000 hours. The cathode requirements of a 30 cm thruster are nominally 10 A of emission with an equivalent neutral atom current of 0.1 to 0.2 A. The study was conducted by operating the cathodes at these nominal neutral and emission currents in the diode configuration shown schematically in Fig. 37. The quantities monitored were discharge voltage, discharge current, neutral current, cathode tip temperature (self-heated), and orifice erosion. Initially, a program plan was organized to investigate separately the effects of

1. Cathode temperature
2. Insert material
3. Orifice diameter
4. Starting mechanisms.

This program was subsequently modified because it was soon evident that the initial cathode design would self-heat at the rated emission current and that the self-heating was proportional to the length of the orifice and inversely proportional to the orifice diameter. In the first cathodes tested, cathode tip temperatures typically self-heated to 1600 to 1700°C (measured with an optical pyrometer) at the 10 A emission level, and severe erosion of the orifice was observed after only a few hours of operation. Thus, all effort was guided toward the reduction of operating temperature and orifice erosion. A number of modifications were made; their sequence was determined to some extent by the data reported by Kerslake and Rawlin.¹⁵ Their data indicate that self-heating of the cathode is reduced if the cathode tip is made thinner (orifice length reduced) or if the diameter of the cathode orifice is made larger. Figure 38 shows the cathode configurations, and Table IX gives the experimental results. The first modification reduced the cathode tip thickness, but maintained the same orifice diameter. Because the operating temperature and orifice erosion were not significantly reduced by this modification, the next modification increased orifice size. The Type II cathode tip was adopted at this point because it was thought that reducing the entire tip thickness to 0.051 cm would limit thermal conduction of heat away from the orifice. In addition, the Type II cathode tip was considered somewhat easier to construct. Because cathode No. 106 showed promise

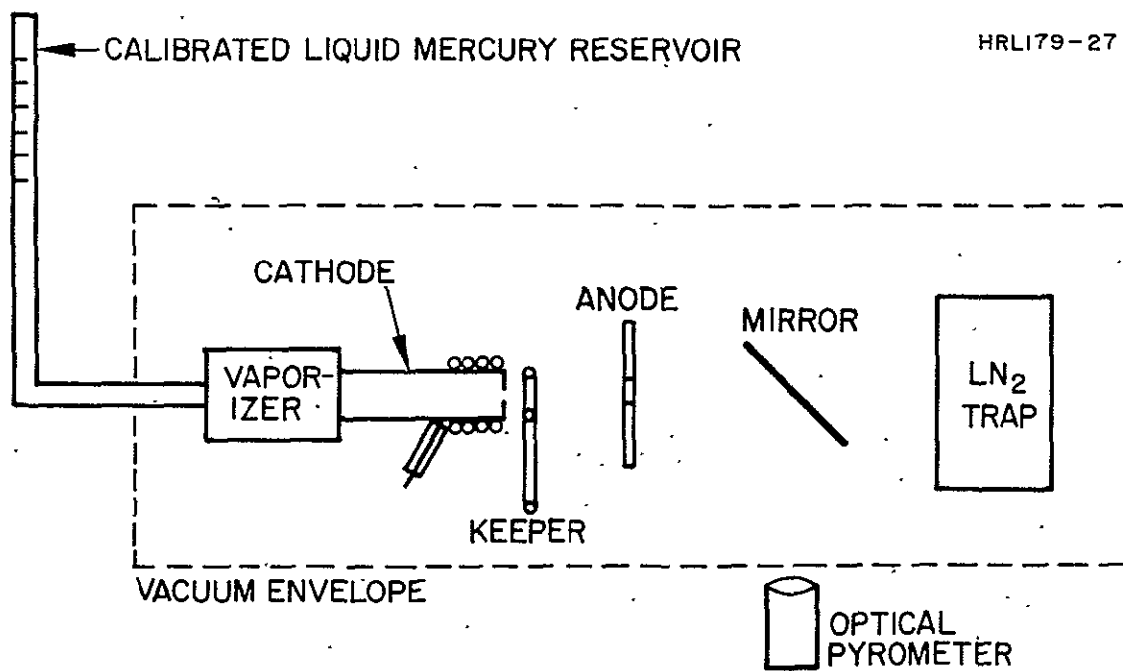


Fig. 37. Schematic diagram of diode configuration for hollow cathode tests.

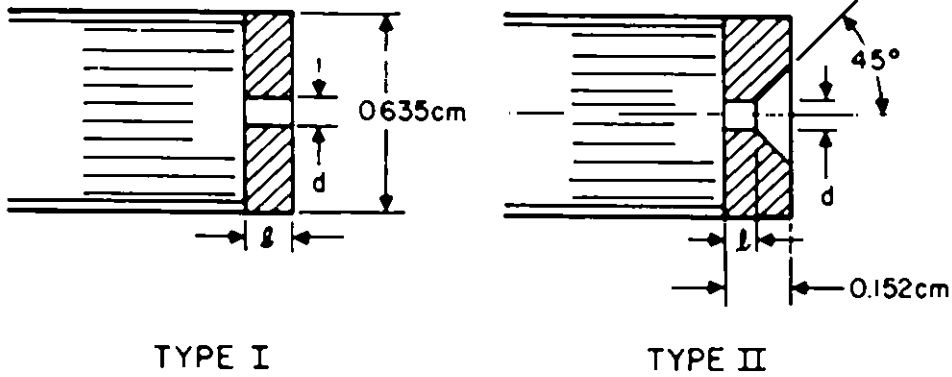


Fig. 38. Cathode configurations.

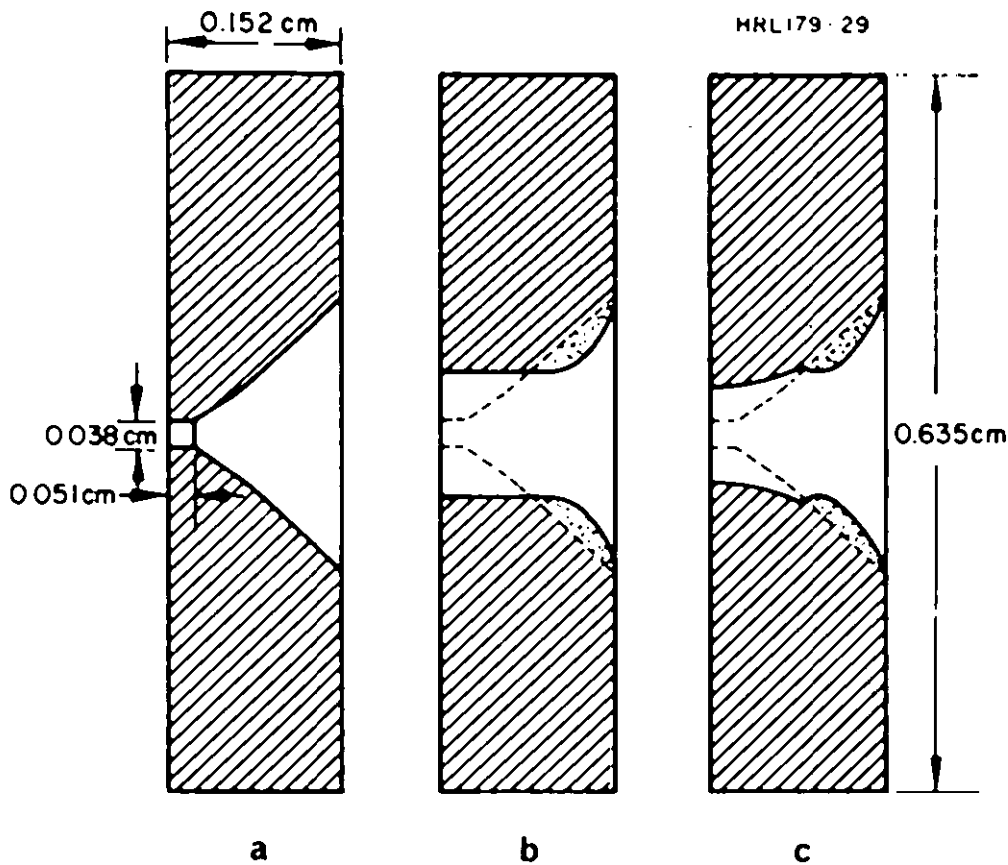


Fig. 39. Cathode tip cross sections synthesized from plastic moldings taken (a) before test, (b) after 22 hours of testing, and (c) after 46 hours of testing.

in initial tests, it was decided to extend the test period. The test time totaled 46 hours, with the test being interrupted after 22 hours to take a mold profile of the orifice. A thermal setting plastic material used by dentists in making oral impressions was used for this profile. By photographing these molds, it is possible to synthesize a cathode tip cross section as shown in Fig. 39. It is interesting to note that during the first 22 hours of testing, rather severe erosion took place, enlarging the orifice and depositing the material removed in the beveled region (Fig. 39(b)). During the next 24 hours of test little additional erosion can be seen; however, there appears to be some re-orientation of the deposited material. Testing was discontinued at this point, and the cathode was cross-sectioned and photographed. The photomicrographs of the cross-sectioned cathode revealed that the crystal structure of the deposited material which fills the 45° bevel portion of the orifice was quite different from that of the undamaged portion of the cathode tip. Thus it appears that erosion of hollow cathode orifices arises from a yet undetermined phenomenon which is a function of both the current density and the contact area of the orifice with the current carrying plasma. Further investigation of this phenomenon probably could lead to a better understanding of the cathode emission mechanism.

The results of this study may be summarized in terms of the originally proposed program, as follows:

1. Cathode temperature — The original 0.63 cm diameter hollow cathode self-heated when operated at rated current, and the cathode temperature was not an independent variable. The final cathode design with a modified orifice geometry has alleviated this difficulty and permits controlled operation at up to 20 A.
2. Insert material — Several types of insert material, coating, and substrate were tried during tests of cathode 102, but no difference in operation or re-starting could be detected.
3. Orifice diameter — Orifice diameter and orifice length are critical dimensions to both operating temperature and cathode erosion.
4. Starting mechanisms — Only one attempt was made to incorporate an internal cathode starter. While a discharge could easily be initiated, it was internal and could not be made to penetrate the orifice.

TABLE IX

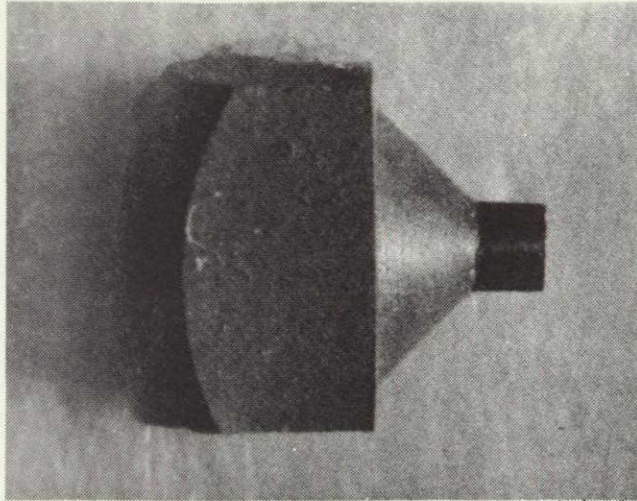
Cathode Tests with Variations on Cathode Configuration
(All data are for bell jar testing with 10 A emission current)

Serial Number	Type	Hours Tested	ℓ , cm	d , cm	Tip Temperature, ^a °C
102	I	20	0.152	0.025	1640
103	I	8	0.051	0.025	1430
106	II	46	0.051	0.038	1250
107	II	16	0.051	0.076	1020
^a Measured with an optical pyrometer.					

Discussions were held with R.T. Bechtel and W. Kerslake of NASA LeRC, and it was determined that cathode orifice diameters of 0.076 cm were currently being operated at LeRC with negligible erosion observed. The final cathode design was therefore fixed with a cathode tip of type II shown in Fig. 38; the orifice diameter was set at 0.076 cm, and orifice length at 0.051 cm. The insert was constructed of tantalum foil and coated with triple carbonate emissive mixture as described in Ref. 15. A single cathode was installed and operated throughout the low specific impulse optimization and test program with no perceptible erosion after an estimated running time of 300 hours at currents ranging up to 20 A. A second cathode of this design was used for the 500 hour design verification test. Figure 40 shows photomicrographs of plastic moldings of the cathode orifice made before and after the 500 hour test. The erosion is again imperceptible. While this is indeed desirable, it reduces to conjecture the extrapolation of cathode lifetime. In this vein, the following reasoning might be applied to determine a projected lifetime.

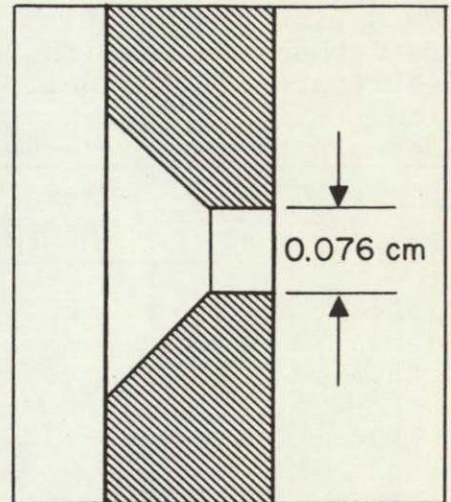
Because cathode erosion is usually first observed as a chamfering of the downstream edge of the orifice, it is plausible that material removal of about 0.002 cm dimension would be perceptible on the corner of the orifice in the photomicrograph of the plastic mold. Because this cannot be seen in Fig. 38, it might be concluded that the erosion rate

M7018



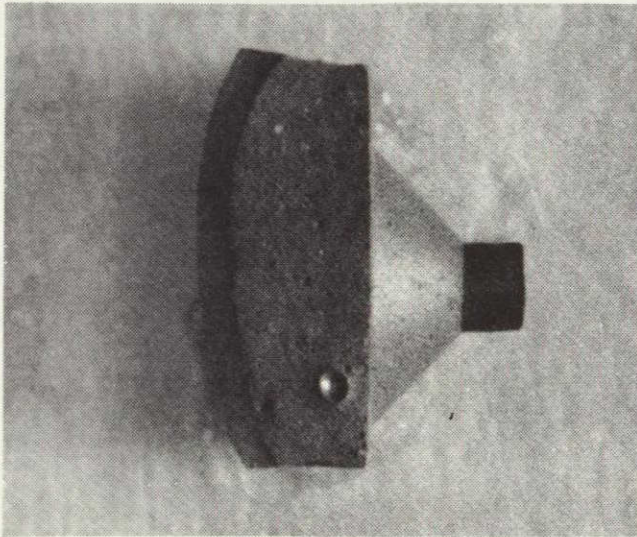
BEFORE TEST

HRL143-41R1



CROSS-SECTION OF
CATHODE ORIFICE

M7017



AFTER TEST

Fig. 40. Profiles of hollow cathode orifice before and after 500 hours of testing.

is on the order of 0.002 cm/500 hours or less. Following this line of reasoning, it would take 10,000 hours or more for this corner to reach the upstream boundary of the orifice and start to increase the orifice size (which is the lifetime limitation). Hence, it can be conjectured that the cathode has a minimum lifetime of 10,000 hours.

In addition to having a long projected lifetime, the type II cathode design is observed to restart more reliably than the type I cathode. One explanation for this observation is that the lower self-heated operating temperature is less damaging to the emissive coating on the insert. In cathode 103, for example, the insert was removed after only 8 hours of operation and the emissive coating was almost entirely depleted. In cathode 107, on the other hand, after 75 hours of the Task II 100 hour test, the insert appeared little different from when it was installed.

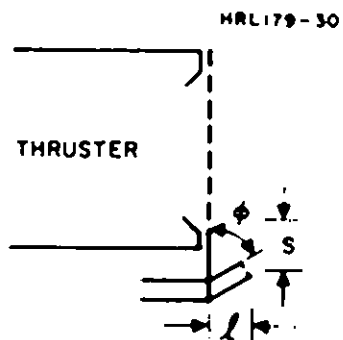
4. Neutralizer Development

As thrusters are operated at lower specific impulses, the importance of the neutralizer increases because space charge density increases even though beam current density remains constant. To obtain neutralization without unduly penalizing either electrical or propellant utilization efficiencies, a plasma bridge neutralizer must

1. operate with a minimum coupling voltage
2. require a minimum propellant flow through the hollow cathode
3. not cause excessive charge exchange erosion to the accelerator grid electrode.
4. have a lifetime comparable to other thruster components (10,000 hours or more).

For a 30 cm thruster operating at a specific impulse of 2750 sec, the hollow cathode neutralizer must operate with less than 100 mA (equivalent) neutral flow rate and must couple to the beam with a maximum of 20 V potential difference between beam and neutralizer cathode. The neutralizer locations and angles tested during the program are summarized in Table X. Variation No. 1 represents the configuration used on the high specific impulse thruster tests. While the electrical performance of this neutralizer location and angle was satisfactory, an unacceptable pattern of charge exchange erosion was observed on the accelerator grid electrode after the 100 hour test of the high specific impulse thruster. Careful examination of the erosion pattern indicated that the neutral atom

TABLE X
Neutralizer Variations and Results



Variation Number	t, cm	S, cm	ϕ , deg.	Incut mA (equiv.)	V_{coupling} , V	Excessive Erosion	Keeper	Test Circuit Schematic, Fig. No.
1	2.54	1.2	30	60	15	Yes	Open	41
2	3.0	2.0	45	80	15	No	Open	41 & 42
3	3	2	30	35	15	Yes	Open	42
4	3	2	45	117	12	No	Open	43
5	2.5	2.5	60	500	15	No	Open	43
6	3	2	45	70	12.7	No	Partially Enclosed	43

efflux from the neutralizer forms a conical plume with half-angle of the order of 45° . It was therefore concluded that the neutralizer cathode angle (shown in Table X as ϕ) should be 45° or more. The rather excessive (for 100 hour operation) erosion was discussed with the NASA contract manager and other members of LeRC, and it was recommended that the length of the ℓ and s dimensions be increased. This was done in variation No. 2, with good results. The charge exchange erosion was monitored by spot welding a 0.001 cm thick sheet of tantalum on the downstream surface of the accelerator grid near the neutralizer. No erosion could be detected. It was thought that the increase in ℓ and s perhaps would be sufficient to account for the improvement in erosion, and that the neutral propellant flow required to obtain the acceptable coupling voltage could be decreased by decreasing the neutralizer cathode angle. Variation No. 3 was an attempt to achieve this; however, although the propellant flow requirement decreased, the erosion rate increased. The remaining variations represent attempts to improve the neutralizer characteristics through slight changes in angle and keeper electrode. The final configuration, No. 6, has a partially enclosed keeper electrode which forces neutral atoms, ions, and electrons to pass through the keeper electrode aperture. The keeper electrode aperture in all cases was 0.48 cm in diameter and was spaced 0.152 cm from the neutralizer cathode tip.

The neutralizer cathode was constructed in the same way as the SERT-II hollow cathode throughout the majority of this program. That is, the cathode tip geometry was like that of type I shown in Fig. 38 with the tube o.d. set at 0.318 cm and the cathode orifice 0.020 cm in diameter and 0.102 cm long. The final design was modified to resemble the thruster cathode, the geometry shown in Fig. 38 as type II. This decision was precipitated when a drill rod was accidentally lodged and broken off in the cathode orifice while attempting to measure the orifice diameter after 100 hours of the 500 hour verification test had been logged. Rather than replace the cathode, it was decided to remove the cathode obstruction by chamfering the orifice. Throughout the remaining 400 hours of the test, the neutralizer orifice showed no tendency to close (as had been observed during some previous tests) and the usual chamfering erosion was absent, as with the thruster cathodes. The final neutralizer cathode geometry, therefore, makes use of the 45° half angle chamfer and thus provides a neutralizer orifice 0.025 cm in diameter and 0.025 cm long. Because both NASA LeRC tests and those performed at HRL indicate that neutralizer failure occurs somewhat anomalously as

a result of cathode orifice closure, it is difficult to project a neutralizer lifetime. On the basis of the thruster cathode development, it is believed that the material which closes the neutralizer cathode originates from the typical chamfering erosion observed on the downstream edge of the cathode orifice of type I cathode tips. If this is the case, there is good reason to believe that the type II cathode tip will eliminate this erosion and orifice closure will not occur. Based on this supposition, neutralizer lifetime can be extrapolated beyond 10,000 hours.

5. Control and Restart Systems

Thruster operation at high specific impulse can be performed quite satisfactorily for short duration testing with open loop control systems (manual control). Consequently, at the beginning of the low specific impulse thruster development program the thruster power conditioning was completely manually controlled. A schematic diagram of the power conditioning used for ion optical system evaluation tests is shown in Fig. 41. Using this system, the establishment and maintenance of the boundary between the discharge chamber plasma and the accelerator system could be performed adequate for short duration tests, but the system required constant attention from and adjustment by the operator because the power supplies used were unable to maintain a constant voltage under instantaneous arcing. In high perveance, low specific impulse ion optical systems, the plasma boundary and the accelerator electrode are in close proximity. If, in the event of an arc across the acceleration region, the power supply voltages drop, the plasma can advance downstream and penetrate into the acceleration region. If the accel electrode power supply can recover before the plasma boundary reaches the accel electrode, the potential distribution will focus the ion current so that it does not intercept the electrode. If the accel power supply does not recover before the plasma engulfs the accel electrode, the power supply must then be capable of delivering sufficient current to sweep out and collect all the ions in the acceleration region, thus forcing the space charge to re-establish the potential distribution which focuses the ion beam. The last statement implies that the accel power supply, which normally supplies current which is only a few percent of the beam current, must be capable of supplying currents of the order of the beam current for short periods of time. The largest available power supply with negative output was installed, and the system was tolerably stable. During the Task II 100 hour test it became evident that more stability was required, and several modifications were made.

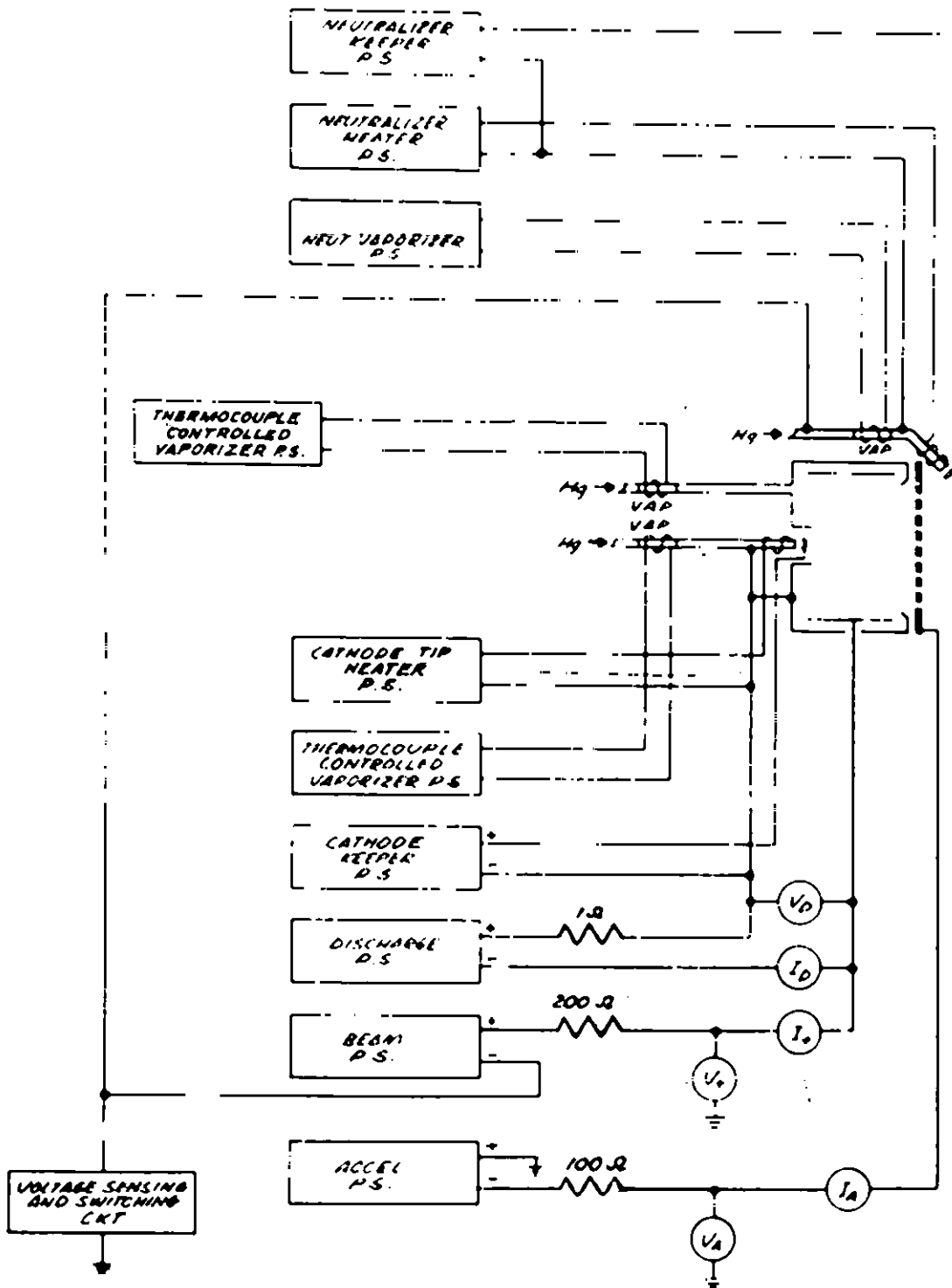


Fig. 41. Initial electrical test system schematic.

First, to supply the current necessary to satisfy arc recovery conditions, a resistance capacitance network was added in the output of the accel power supply. The logic of this circuit is as follows. The capacitor nearest the load (accel) discharges to satisfy the arc requirements. This drops the output voltage instantaneously; however, the energy stored in the remaining capacitors rapidly recharges the discharged capacitor and the effective voltage recovery time is significantly shortened. In this way, the current surge required from the accel power supply is reduced in magnitude and stretched out in time. While this circuit improved operational stability, occasional penetration of the acceleration system by the discharge plasma was still observed. Part of this instability was attributed to activation of the neutralizer bias bypass circuit by the transients from the capacitive discharge. A capacitor was installed to bypass transients and increase the response time of the bypass circuit. This further improved stability. These modifications are shown in Fig. 42.

At the outset of the Task III optimization program, a set of electrical isolators were installed in the thruster chamber and thruster cathode mercury vapor feed lines. This permitted operation of the vaporizer power supply at ground potential and allowed installation of a control loop for controlling thruster chamber vaporizer power (main propellant flow) in proportion to beam current. In addition, it was discovered that the ion beam could be restored after a plasma penetration of the grid by simply switching the ac power input to the discharge power supply off and on. The time constant with which the discharge voltage decayed was relatively long due to the large filter capacitors in the output of this supply. This modification was incorporated into the power conditioning as a control loop which switched off the discharge supply input power whenever the accel current exceeded a preset value. These modifications are shown in Fig. 43. With this system, the thruster could be operated with little or no adjustment by the operator after initial warm-up and adjustment.

Although the system shown in Fig. 43 provides satisfactory control for stable operation, the following shortcomings were noted:

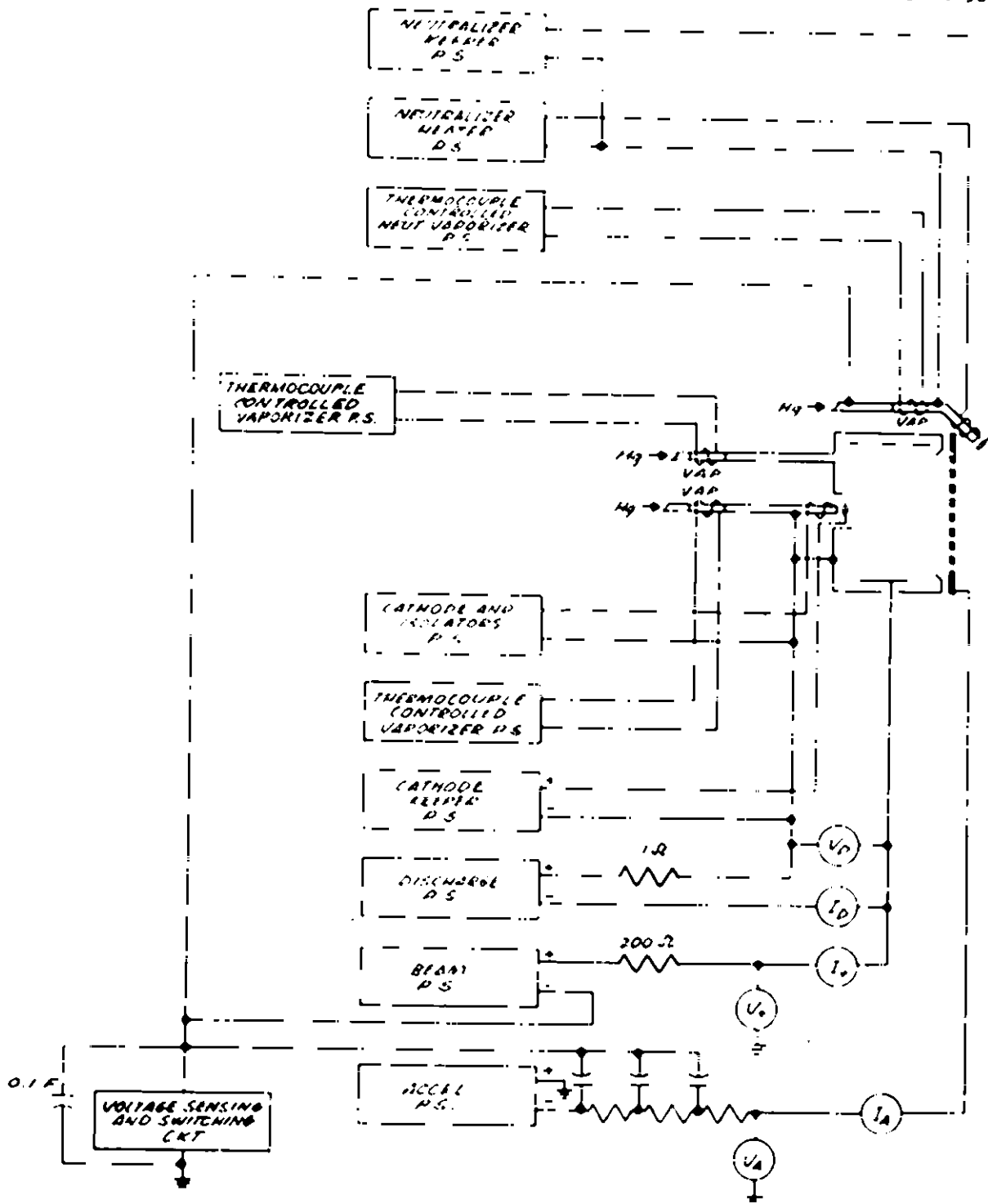


Fig. 42. Electrical test system schematic showing modification required for stabilization during Task II 100 hour test.

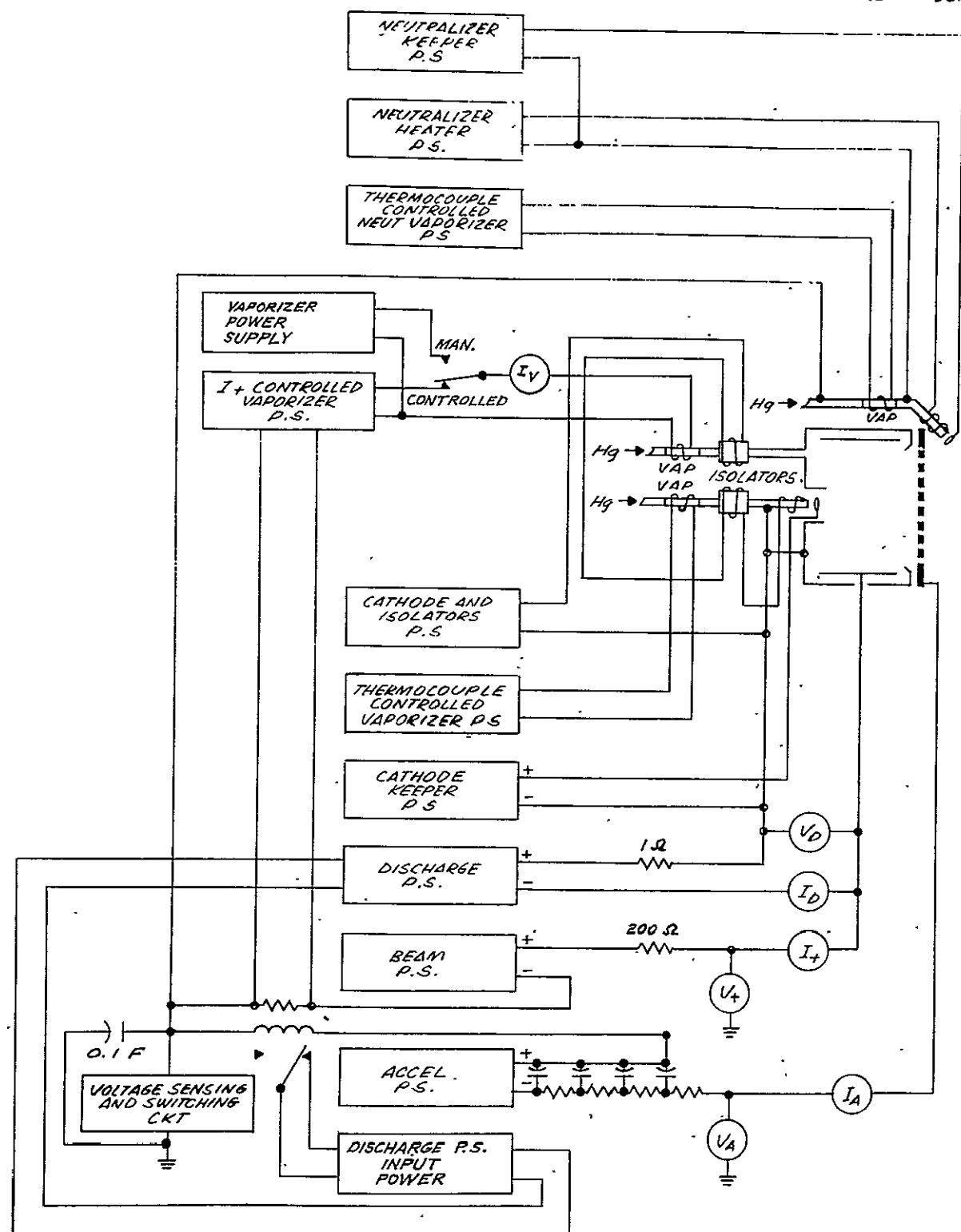


Fig. 43. Electrical test system schematic showing modifications used for Task III and IV testing.

1. Control of the hollow cathode vaporizer based on vaporizer temperature does not insure that the cathode flow rate remains constant, and consequently the discharge voltage tends to vary. Control of the hollow cathode vaporizer in proportion to discharge voltage would be preferable.
2. A thruster-control loop instability exists in the beam current-vaporizer control loop. This instability does not appear while the control loop is maintaining a stable operating point, but only when the beam set control is adjusted to obtain higher beam currents. The instability is manifested as a change in discharge mode such that increasing propellant flow causes a decrease in extracted ion beam.

During this program this problem was circumvented by installing a manually controlled vaporizer power supply for increasing propellant flow to increase beam current. This power supply was also used to hold propellant flow constant over short periods for thruster performance mapping. For automatic power level control, a new solution must be found.

3. Re-establishment of the ion beam by switching the discharge power supply input places undue strain on power supply components. A method which would control the discharge, beam, and accel power supply outputs in a predetermined sequence, would be preferable.

6. Thruster Tests

This section briefly discusses test procedures and methods used throughout the program and presents representative data indicative of the thruster performance and component lifetime at the completion of each task.

a. Thruster Performance

All tests were performed in the HRL 9 ft diameter vacuum facility in which ambient pressure is typically 10^{-6} Torr during testing. The thrusters were operated for sufficient time (1 or 2 hours) to come to equilibrium before electrical and mercury flow data are recorded. Flow data are obtained by recording the mercury level in each reservoir as a

function of time and fitting these data with a straight line. For short duration tests, electrical parameters are read for each performance mapping. For the longer design verification tests, both electrical and flow data were taken at 30 min intervals throughout the test. Variable power operation (throttling) was performed by stabilizing propellant flow at each power level and performance mapping (discharge losses versus propellant utilization). The variable power operation characteristic of the thruster was then obtained by cross plotting points taken from these performance mapping curves.

Representative thruster parameters from Tasks II, III, and IV are presented in Table XI. A comparison of representative performance mappings for each stage of development is given in Fig. 44. At least part of the improvement seen in the performance mappings for Tasks III and IV can be attributed to improvement in the fabrication of the insulated grid. Both the quality and uniformity of the coating improved with each grid, and better performance was observed. Throttling characteristics of the thruster chamber developed under this program are shown in Fig. 45. These data points were obtained as described above, without a control system. Many beam profiles were obtained during both the short term and the longer design verification tests, using the probe configuration shown in Fig. 46. Beam profiles were measured at two locations, 2.5 cm and 1.5 m downstream of the accel electrode. Representative beam profiles for these locations are shown in Figs 47 and 48. In addition to the performance data presented in this report, extensive documentation has been submitted in the form of special reports covering the longer design verification tests. In the Task II 100 hour test, most of the difficulties which were experienced during the test were related to the power conditioning and thruster wiring. In the Task III 100 hour test, the insulated grid failed after 76 hours of operation and a second grid was required to complete the 100 hour test. For the Task IV 500 hour test, power conditioning and control systems operated without difficulty throughout the test period. The only disappointing aspect of the test was the short lifetime of the insulated single grid ion optical system. Three grids were required to complete the test. Table XII summarizes the performance during the three test periods and the average results for the total test

b. Component Lifetime

As discussed in Section III-B-3, useful lifetimes of greater than 10^4 hours may be anticipated for the hollow cathode and neutralizer cathode as a result of the 500 hour test conducted in Task IV. The insulated electrodes, on the

TABLE XI

Comparison of Representative Thruster Parameters for Tasks II, III, and IV

	Task II			Task III			Task IV		
	V	A	P	V	A	P	V	A	P
Beam	1000	1.59	1590	1000	1.86	1860	1000	1.854	1854
Discharge	35.4	9.8	347	36.5	10.3	376	40.9	8.6	353
Accel	640	0.040	65.6 ^a	580	0.053	84 ^a	405	0.050	70.2 ^a
H.C. Heater	7.8	3.0	23.4	7.3	2.8	20.4	18.1	2.8	50.6 ^c
Neut. Heater	4.9	3.1	15.2	6.4	3.1	19.8	5.0	2.9	14.5
H.C. Keeper	8.1	0.29	2.4	9.0	0.25	2.2	8	0.28	2.2
Neut. Keeper	10.2	0.27	2.8	11	0.2	2.3	9.7	0.22	2.1
Main Vaporizer	2.9	2.1	6.1	3.8	2.55	9.7	3.6	2.4	8.6
H.C. Vaporizer	1.9	1.6	3.0	2.5	2.08	5.2	2.3	2.0	4.6
Neut. Vaporizer	2.3	2.2	5.1	1.9	1.6	3.0	1.5	1.1	1.6
Neut. Coupling	22 ^b	1.59	35.0	22 ^b	1.86	41	21.9 ^b	1.185	40.6
Cathode Isolator				6.5	3.0	19.5	see c		
Main Isolator				6.4	3.0	15.0			
Total Power			2095.6			2458.1			2402.0
^a Accel power is computed as $I_{\text{accel}} \times V_{\text{total}}$. ^b Neutralizer coupling power is computed as $I_{\text{beam}} \times (V_{\text{neut}} + 12)$. ^c Cathode heater and isolator heaters were operated in series.									

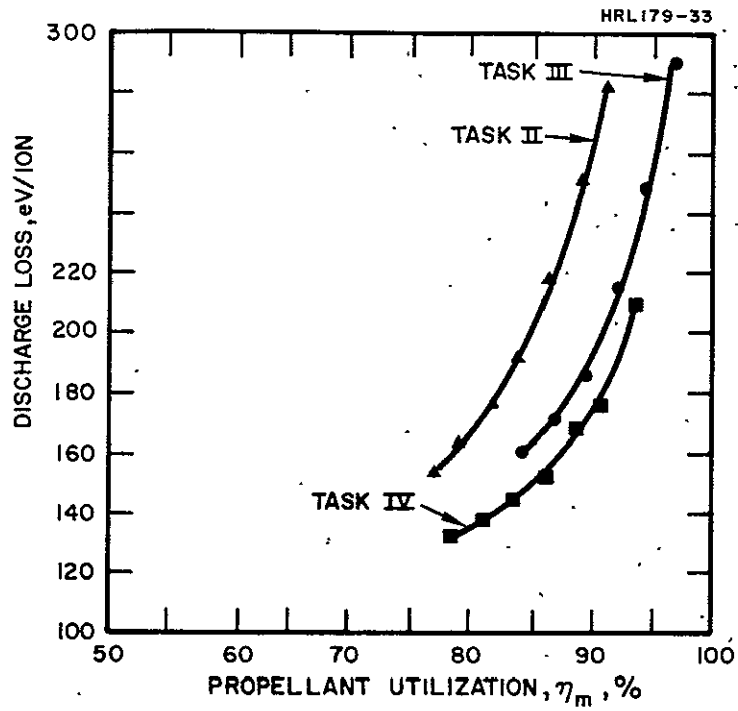


Fig. 44. Comparison of performance mapping for several stages of thruster development.

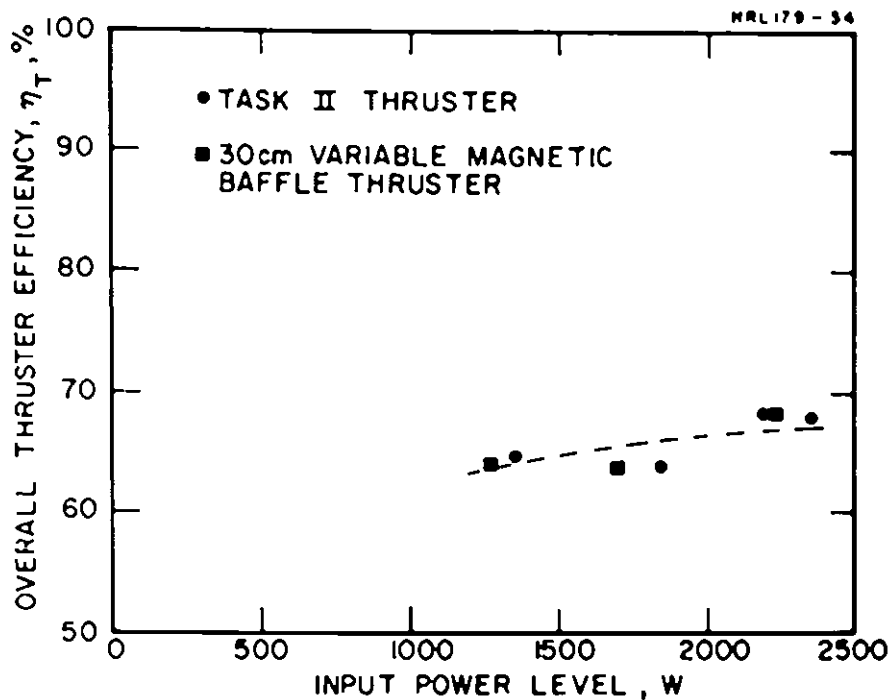


Fig. 45. Variable power operation characteristic for the 30 cm thruster chamber developed under this program (2750 sec specific impulse).

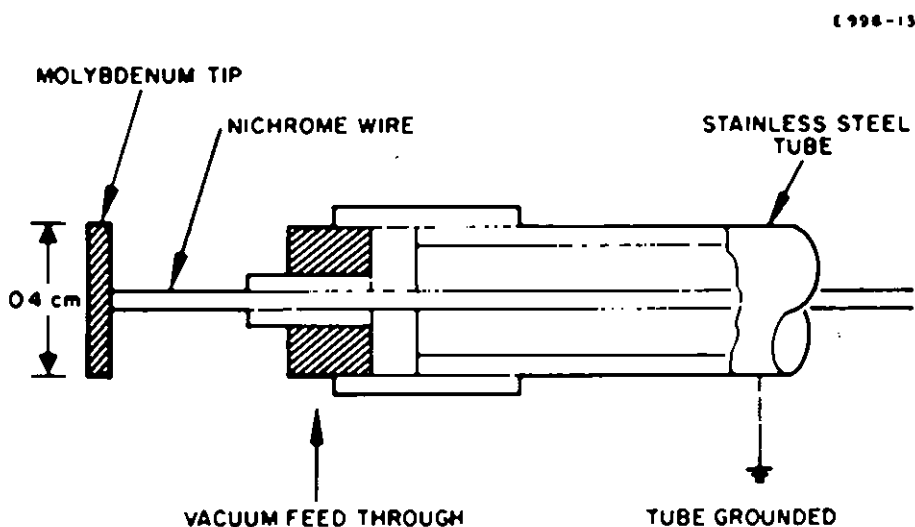


Fig. 46. Probe configuration for measuring ion beam profiles.

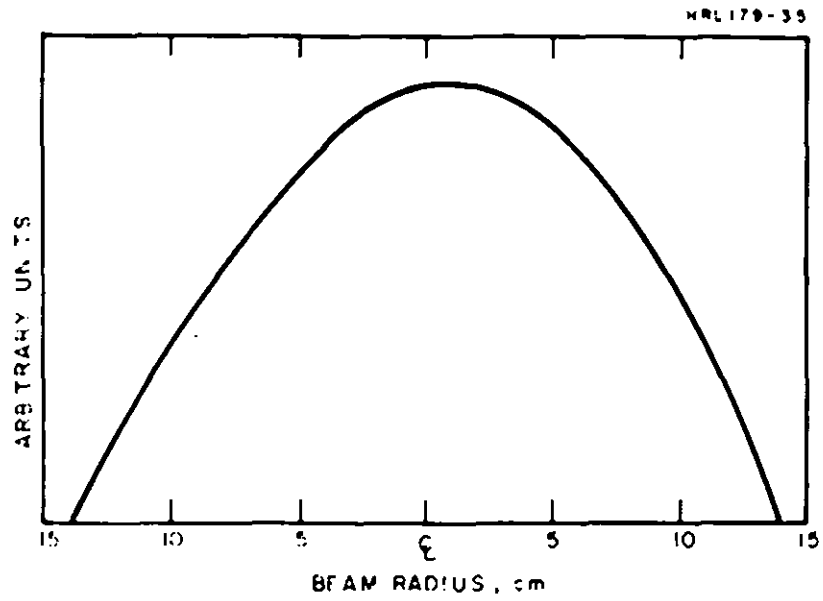


Fig. 47. Beam profile 2.5 cm downstream of accel electrode.

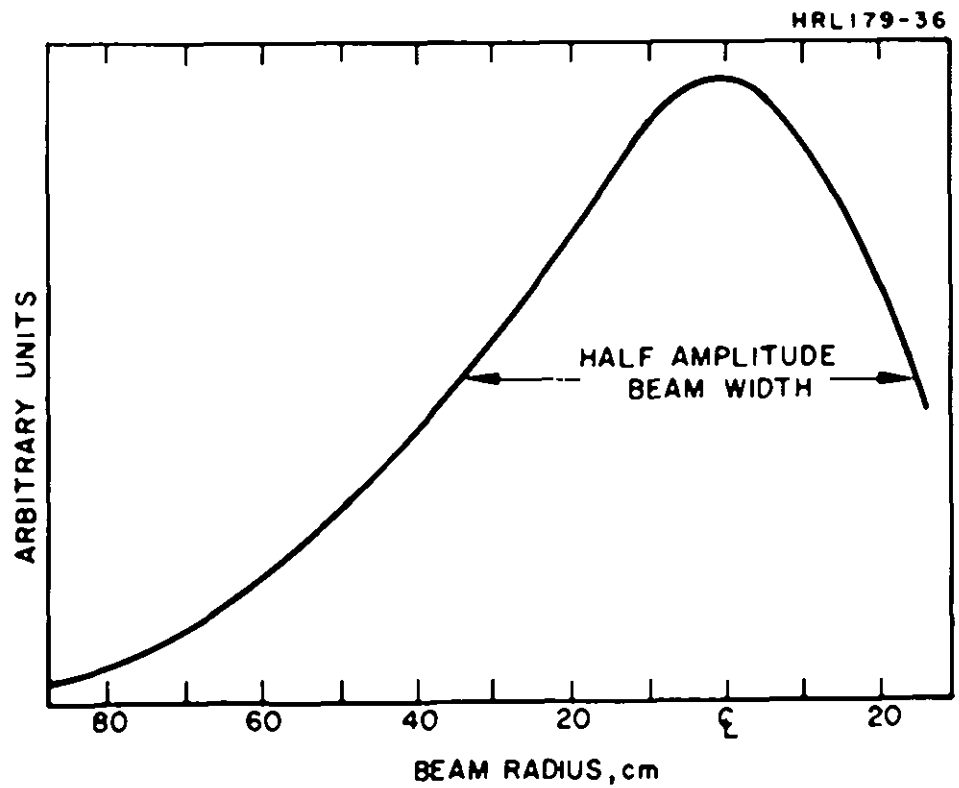


Fig. 48. Beam profile 1.52 cm downstream of accel electrode.

TABLE XII

Task IV 500 Hour Test Performance Summary

Parameter	Hours 0 + 200			Hours 200 + 400			Hours 425 + 500			Total Test ^a		
	V	I	P	V	I	P	V	I	P	V	I	P
Beam	1000	1.849	1849.0	1000	1.856	1856.0	1000	1.863	1863.0	1000	1.854	1854.0
Discharge	41.0	8.9	363.0	41.1	8.2	339.0	40.1	9.0	361.0	40.9	8.6	353.0
Accel ^b	480	0.055	81.4	350	0.049	66.2	352	0.038	51.4	405	0.050	70.2
Cathode and Isolators Heater	18.4	2.9	53.4	17.9	2.7	48.3	18.0	2.8	50.4	18.1	2.8	50.6
Neut. Htr.	5.0	2.8	14.0	5.0	2.9	14.5	5.0	2.9	14.5	5.0	2.9	14.5
Cath. Keeper	8.2	0.31	2.5	8.0	0.25	2.0	7.7	0.25	1.9	8.0	0.28	2.2
Neut. Keeper	11.9	0.25	3.0	8.4	0.20	1.7	7.2	0.20	1.4	9.7	0.22	2.1
Main Vap.	3.6	2.3	8.3	3.5	2.4	8.4	3.6	2.4	8.6	3.6	2.4	8.6
Cath. Vap.	2.4	2.1	5.0	2.3	2.0	4.6	2.3	2.0	4.6	2.3	2.0	4.6
Neut. Vap.	1.6	1.2	1.9	1.4	1.0	1.4	1.5	1.1	1.6	1.5	1.1	1.6
Neut. Coupling ^c	24.2	1.849	44.7	20.2	1.856	37.5	20.0	1.863	37.3	21.9	1.854	40.6
Total Power	2,426.2 W			2,379.6 W			2,395.7 W			2,402.0 W		
Total Losses	577.2 W			523.6 W			532.7 W			548.0 W		
Electrical Efficiency	76.6%			78.0%			77.9%			77.1%		
Mass Efficiency	87.0%			92.2%			92.0%			90.0%		
Total Efficiency	66.6%			71.9%			71.7%			69.4%		
Thrust	26.9 mlb			27.0 mlb			27.1 mlb			27.0 mlb		
I _{sp}	2,751 sec			2,915 sec			2,909 sec			2,846 sec		
Power/Thrust.	90.3 W/mlb			87.1 W/mlb			88.4 W/mlb			89 W/mlb		
eV/Ion	196			183			194			190		
Main Flow Rate	1.04 cm ³ /hr			1.00 cm ³ /hr			1.02 cm ³ /hr			1.02 cm ³ /hr		
Cathode Flow Rate	0.095 cm ³ /hr			0.065 cm ³ /hr			0.061 cm ³ /hr			0.077 cm ³ /hr		
Neut. Flow Rate	0.041 cm ³ /hr			0.044 cm ³ /hr			0.040 cm ³ /hr			0.042 cm ³ /hr		

^aData from hours 400 + 425 excluded because of electron backstreaming through the grid.

^bAccel Power is computed as $I_{\text{accel}} \times V_{\text{total}}$.

^cNeut. Coupling Volt = Thruster floating potential plus estimated beam potential of 12 V.

other hand, failed after approximately 200 hours of operation. The failure process was one of erosion of the insulating coating in a localized area, so that the negative electrode was exposed to direct ion bombardment at the full extraction voltage. The exposed electrode area soon sputtered away and the failure progressed to the point where either backstreaming of electrons or loss of ion focusing ability occurred in that local area. The fact that the failed area was destroyed, plus the different environmental conditions between an operating thruster and bench test of the electrode before and after operation, make quantitative analysis difficult.

We first list a number of empirical observations made about the electrode system during and after failure, followed by a discussion of mechanisms which may be responsible for the degradation.

(1) Observations

- a. After operation for 200 hours, three radial zones usually may be identified on the electrode. The central zone (~ 5 cm diameter) appears to be eroded by direct ion impingement. Sections cut from this area generally show a degradation in the structural properties of the glass. The next area (to a diameter of ~ 20 cm) is generally in good condition and shows little evidence of sputtering or other damage. The outer zone shows some general erosion intermediate between the first two. The apertures in this zone are often irregular in shape.
- b. Failure may occur in any of the three zones defined above and at any azimuth. The failure point does not appear to be connected in any way with the location of the neutralizer or any other thruster component.
- c. Backsputtered material from the collector is deposited on the downstream face of the electrode and in the electrode apertures on the ceramic coating. The deposits are heavier in zone III near the thruster periphery.
- d. Electrode No. 35, which was used to start the 500 hour life test, was removed from test after 10 hours of test and after 100 hours of test for inspection. It was then observed through a high power telescope during the remainder of its test until failure at 200 hours. No visual

erosion was observable at 10 hours. A few apertures showed slight erosion at 100 hours. Gross changes in aperture shape began to appear approximately 24 hours before the test was terminated.

- e. It has not been possible to correlate the failure location with any anomalous physical characteristic of the grids (i.e., thickness, minor flaws, discoloration, aperture size, etc.) using high resolution pictures taken prior to the test.
- f. An insulating coating (presumably from the electrode) builds up on the anode during the test.
- g. No incandescence or other indication of temperatures high enough to melt the insulating coating has been observed during the test.
- h. Neither the arcing rate nor the accelerator current increases dramatically as erosion becomes visible.

(2) Probable Failure Mechanisms

- a. Sputtering - Cross sections of the electrodes taken from zones I, II, and III are shown in Fig. 49. The electrode shapes are consistent with the model illustrated in which direct sputtering occurs in the central region because of the high current density there. Similarly, ions which cross over due to the lack of space charge in zone III will sputter this region in a less localized way. This general picture is consistent with computer studies of ion extraction systems with varying ion arrival rate. The actual rate at which material is removed cannot be predicted because of the unknown sputtering coefficients of the insulator and the poorly defined current density and energy of the arriving ions. Modifying the shape of the insulating material may have several effects on the performance - change in the shape of the equipotential lines, exposure of the softer filler glass material, and reduction in the insulation strength due to reduced thickness of the insulator. The impacting ions may also modify the substrate material; however, this is speculative at best.

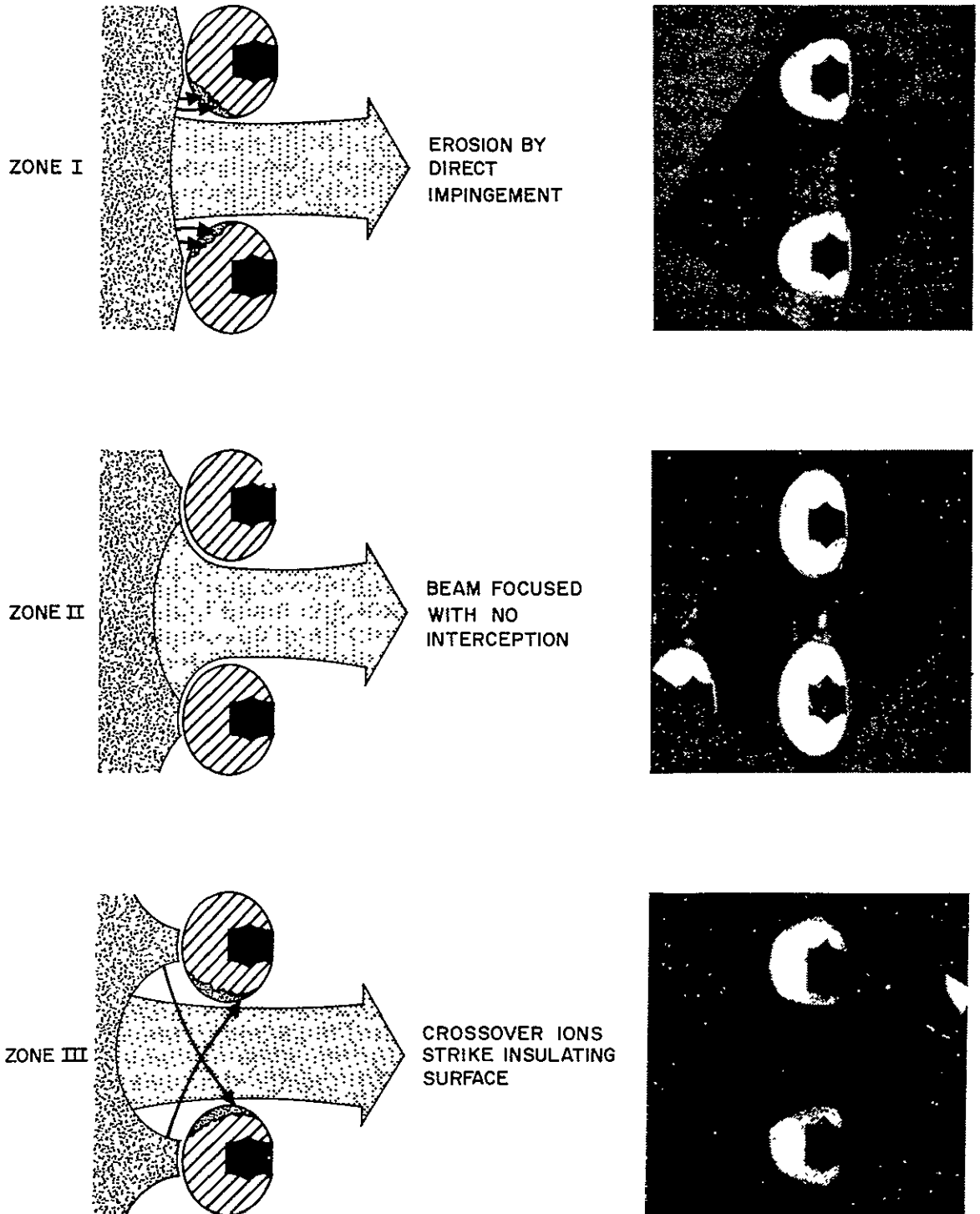


Fig. 49. Effect of ion sputtering of insulating coating.

- b. Buildup of surface charge — A buildup of surface charge due to impacting ions would modify the equipotentials and hence the performance of the ion optical system. This depends critically on the ion arrival rate and leakage resistance of the insulating material. Poor performance of a pure alumina insulator during a brief test of that material prior to this program is taken as an indication that the high surface and volume resistance of this material may prevent the surface charge from leaking away, thus preventing the plasma sheath from stabilizing at the desired location.
- c. Deposition of sputtered material — It is visually observed that a metallic sputtered deposit builds up on the exposed downstream surfaces of the electrode, even though the beam path is 5 m long. This deposition is greatest near the periphery, where its removal by charge exchange erosion is a minimum. This sputtered film modifies both the equipotentials and the surface leakage and is a source of numerous small arcs which are visible during the test. A change in operating current or voltage is generally accompanied by a period of intensive arcing which appears to remove some of this sputtered material. Obviously, testing in a large facility where the removal rate by charge exchange ion sputtering exceeds the deposition rate would be desirable.
- d. Ion migration¹⁶ — It has been observed that when a voltage is impressed across a glass sheet, the ionic constituents in the glass (particularly the positive ions) tend to migrate. After long exposure to electric fields the mechanical properties of the glass have been observed to degrade. This may be the cause of the poor structural properties of the glass in zone I. A possibly related observation is that of a region of failure adjacent to the metal electrode in otherwise structurally integral coatings near the edge of zone I. While a number of totally unrelated explanations for these observations may be possible (i.e., gas evolving from the metal, voids created during manufacture, etc.), these regions may represent

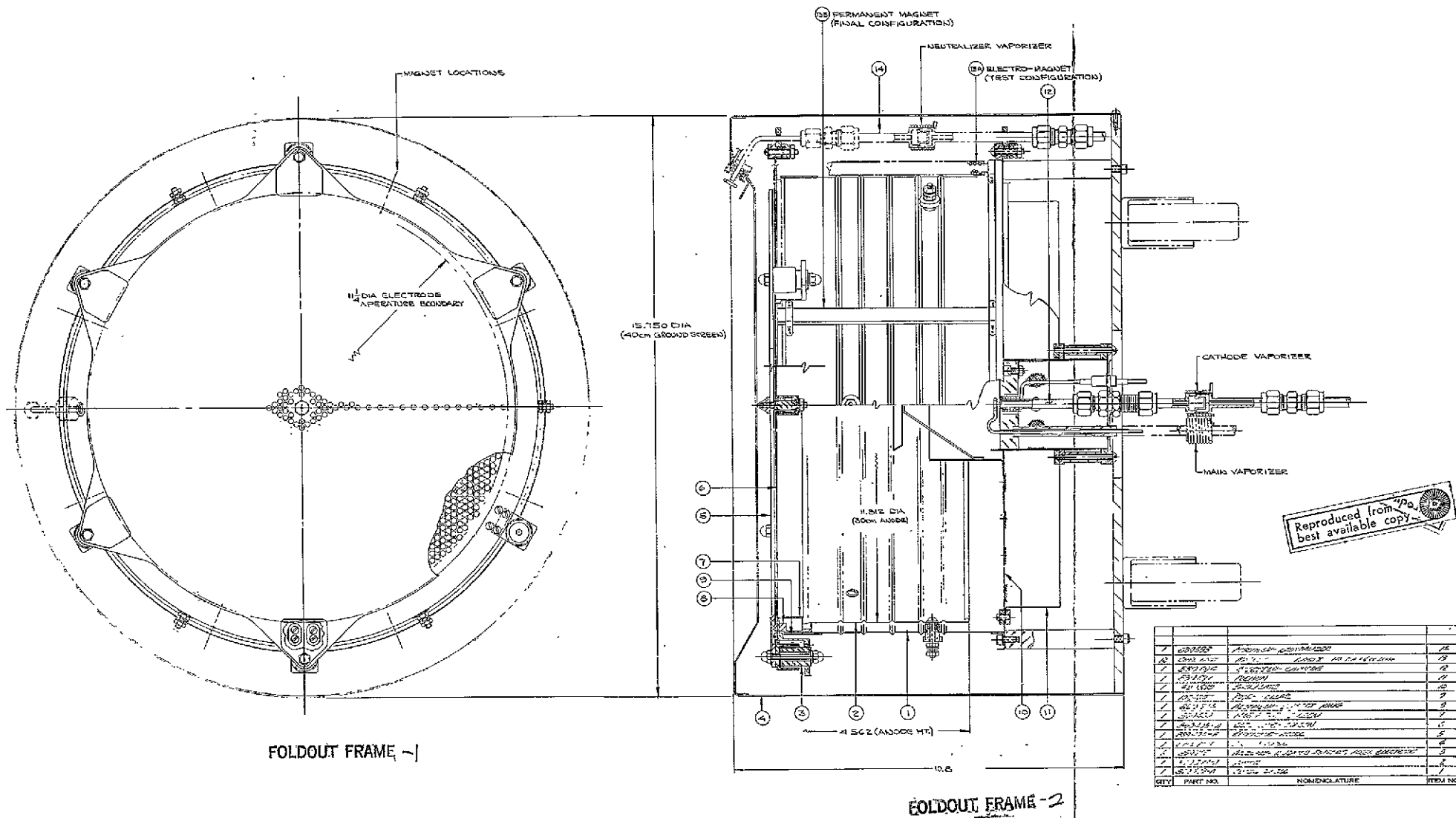
areas of high voltage gradient at the boundary of a depleted region. This depletion may be enhanced by removal of material by sputtering and the continuous impingement of positive charge on the surface.

- e. Thermal runaway. - The resistivity of all ionic glasses falls rapidly by several orders of magnitude as the glasses are heated a few hundred degrees. If a voltage is impressed across the glass at the time of heating, the leakage currents will increase to the point where I^2R losses will ultimately continue to heat the glass, until a thermal runaway condition exists. This phenomenon itself may destroy the glass or it may modify the equipotential shapes sufficiently that the conditions necessary for stable ion beam extraction are no longer fulfilled. This phenomenon also will be enhanced by sputter erosion, particularly if the coating thickness is marginal to begin with.
- f. Aperture shape - The procedure used to perforate the molybdenum electrodes (i.e., chemical milling) produces an aperture with a "waist" as seen in the photographs in Fig. 49. The thinner insulating coating in this area may be subject to higher electrical and mechanical stress and as a result may deteriorate more rapidly than other regions, thus creating a local area from which the erosion can spread.

Presumably all of the above phenomena are present to some degree. Further analyses and tests are required to determine quantitatively the extent to which each contributes to the electrode failure.

C. DELIVERABLE HARDWARE

Thrusters identical to those used in the Task I design verification tests and the Task IV endurance test were fabricated and delivered to LeRC as part of the contracted effort. The design layouts and photographs shown in Figs. 50 through 55 illustrate the deliverable hardware. All parts were fabricated to mil spec drawings (MIL-D-1000 category E - Form 3) and were delivered complete with the quality control and drawing package specified in the contract. Table XIII summarizes the mechanical and performance characteristics of each thruster.



ig. 50. Task I 30 cm thruster delivered under contract.

M 6775

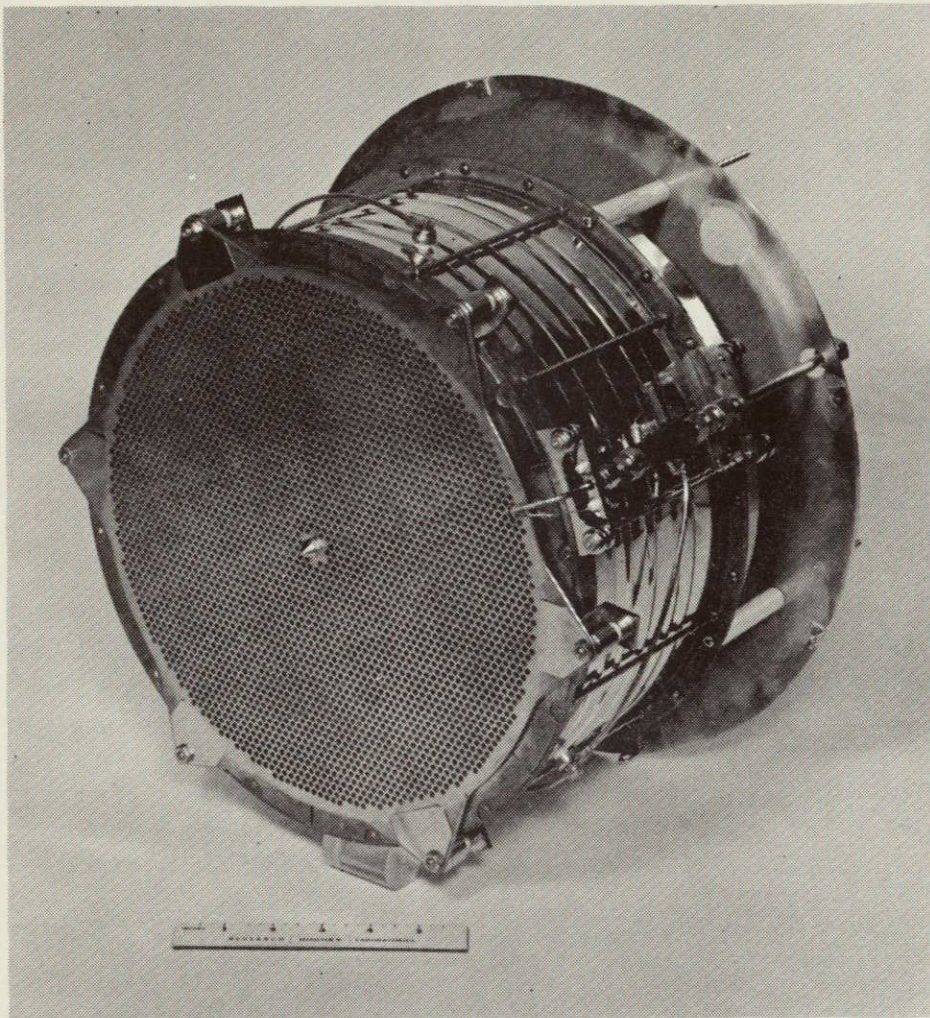


Fig. 51. Task I 30 cm thruster delivered under contract.

M 6773

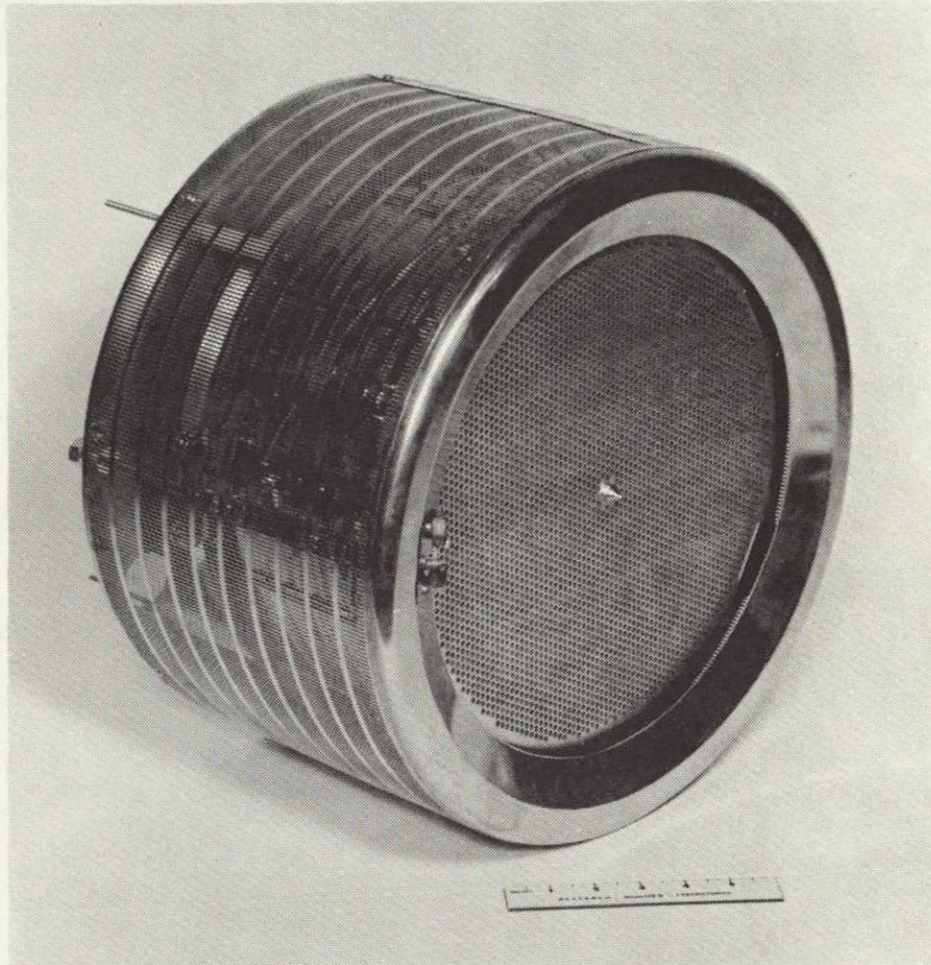
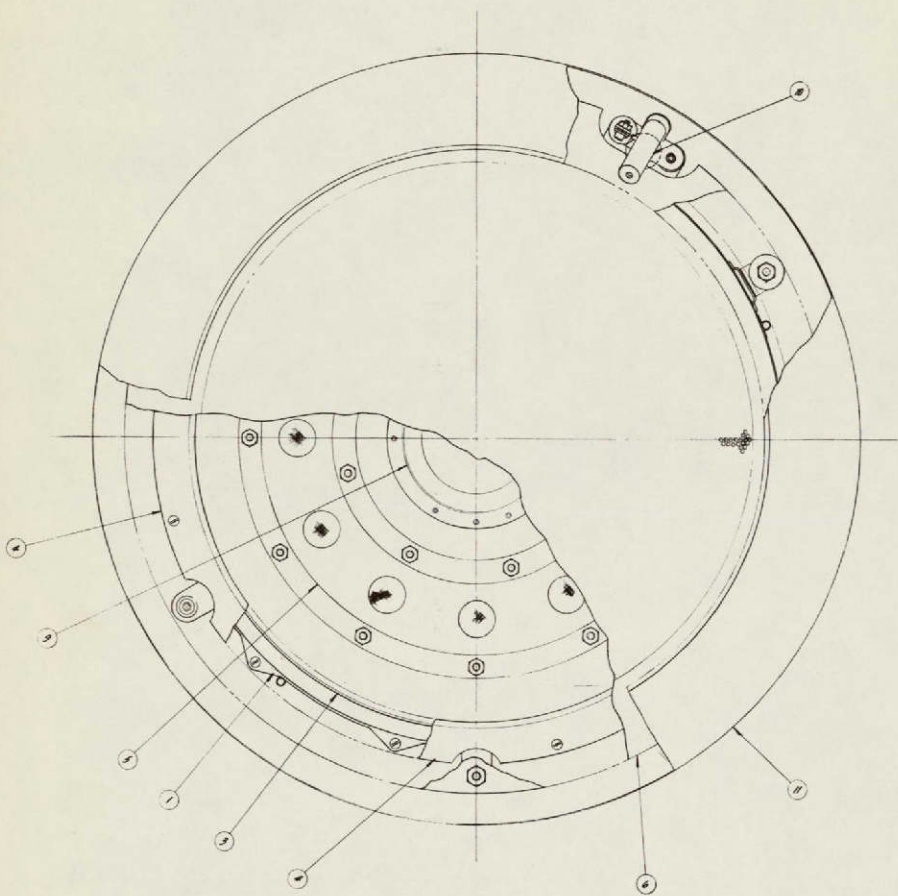
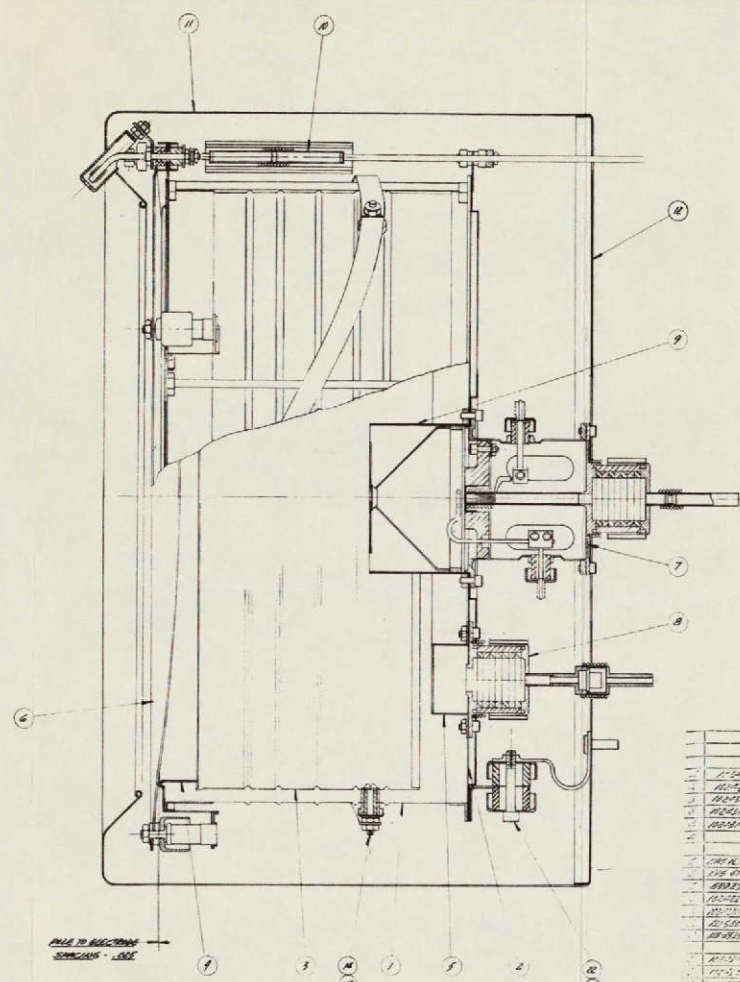


Fig. 52. Task I 30 cm thruster delivered under contract.



FOLDOUT FRAME - 1



FOLDOUT FRAME - 2

Reproduced from
best available copy.

QTY	PART NO.	NOMENCLATURE	ITEM NO.
1	1-1000	FLANGE-ROD	1
1	1-1001	FLANGE-ROD	2
1	1-1002	FLANGE-ROD	3
1	1-1003	FLANGE-ROD	4
1	1-1004	FLANGE-ROD	5
1	1-1005	FLANGE-ROD	6
1	1-1006	FLANGE-ROD	7
1	1-1007	FLANGE-ROD	8
1	1-1008	FLANGE-ROD	9
1	1-1009	FLANGE-ROD	10
1	1-1010	FLANGE-ROD	11
1	1-1011	FLANGE-ROD	12
1	1-1012	FLANGE-ROD	13
1	1-1013	FLANGE-ROD	14
1	1-1014	FLANGE-ROD	15
1	1-1015	FLANGE-ROD	16
1	1-1016	FLANGE-ROD	17
1	1-1017	FLANGE-ROD	18
1	1-1018	FLANGE-ROD	19
1	1-1019	FLANGE-ROD	20
1	1-1020	FLANGE-ROD	21
1	1-1021	FLANGE-ROD	22
1	1-1022	FLANGE-ROD	23
1	1-1023	FLANGE-ROD	24
1	1-1024	FLANGE-ROD	25
1	1-1025	FLANGE-ROD	26
1	1-1026	FLANGE-ROD	27
1	1-1027	FLANGE-ROD	28
1	1-1028	FLANGE-ROD	29
1	1-1029	FLANGE-ROD	30
1	1-1030	FLANGE-ROD	31
1	1-1031	FLANGE-ROD	32
1	1-1032	FLANGE-ROD	33
1	1-1033	FLANGE-ROD	34
1	1-1034	FLANGE-ROD	35
1	1-1035	FLANGE-ROD	36
1	1-1036	FLANGE-ROD	37
1	1-1037	FLANGE-ROD	38
1	1-1038	FLANGE-ROD	39
1	1-1039	FLANGE-ROD	40
1	1-1040	FLANGE-ROD	41
1	1-1041	FLANGE-ROD	42
1	1-1042	FLANGE-ROD	43
1	1-1043	FLANGE-ROD	44
1	1-1044	FLANGE-ROD	45
1	1-1045	FLANGE-ROD	46
1	1-1046	FLANGE-ROD	47
1	1-1047	FLANGE-ROD	48
1	1-1048	FLANGE-ROD	49
1	1-1049	FLANGE-ROD	50
1	1-1050	FLANGE-ROD	51
1	1-1051	FLANGE-ROD	52
1	1-1052	FLANGE-ROD	53
1	1-1053	FLANGE-ROD	54
1	1-1054	FLANGE-ROD	55
1	1-1055	FLANGE-ROD	56
1	1-1056	FLANGE-ROD	57
1	1-1057	FLANGE-ROD	58
1	1-1058	FLANGE-ROD	59
1	1-1059	FLANGE-ROD	60
1	1-1060	FLANGE-ROD	61
1	1-1061	FLANGE-ROD	62
1	1-1062	FLANGE-ROD	63
1	1-1063	FLANGE-ROD	64
1	1-1064	FLANGE-ROD	65
1	1-1065	FLANGE-ROD	66
1	1-1066	FLANGE-ROD	67
1	1-1067	FLANGE-ROD	68
1	1-1068	FLANGE-ROD	69
1	1-1069	FLANGE-ROD	70
1	1-1070	FLANGE-ROD	71
1	1-1071	FLANGE-ROD	72
1	1-1072	FLANGE-ROD	73
1	1-1073	FLANGE-ROD	74
1	1-1074	FLANGE-ROD	75
1	1-1075	FLANGE-ROD	76
1	1-1076	FLANGE-ROD	77
1	1-1077	FLANGE-ROD	78
1	1-1078	FLANGE-ROD	79
1	1-1079	FLANGE-ROD	80
1	1-1080	FLANGE-ROD	81
1	1-1081	FLANGE-ROD	82
1	1-1082	FLANGE-ROD	83
1	1-1083	FLANGE-ROD	84
1	1-1084	FLANGE-ROD	85
1	1-1085	FLANGE-ROD	86
1	1-1086	FLANGE-ROD	87
1	1-1087	FLANGE-ROD	88
1	1-1088	FLANGE-ROD	89
1	1-1089	FLANGE-ROD	90
1	1-1090	FLANGE-ROD	91
1	1-1091	FLANGE-ROD	92
1	1-1092	FLANGE-ROD	93
1	1-1093	FLANGE-ROD	94
1	1-1094	FLANGE-ROD	95
1	1-1095	FLANGE-ROD	96
1	1-1096	FLANGE-ROD	97
1	1-1097	FLANGE-ROD	98
1	1-1098	FLANGE-ROD	99
1	1-1099	FLANGE-ROD	100

Fig. 53. Task V 30 cm thruster delivered under contract.

M 7054

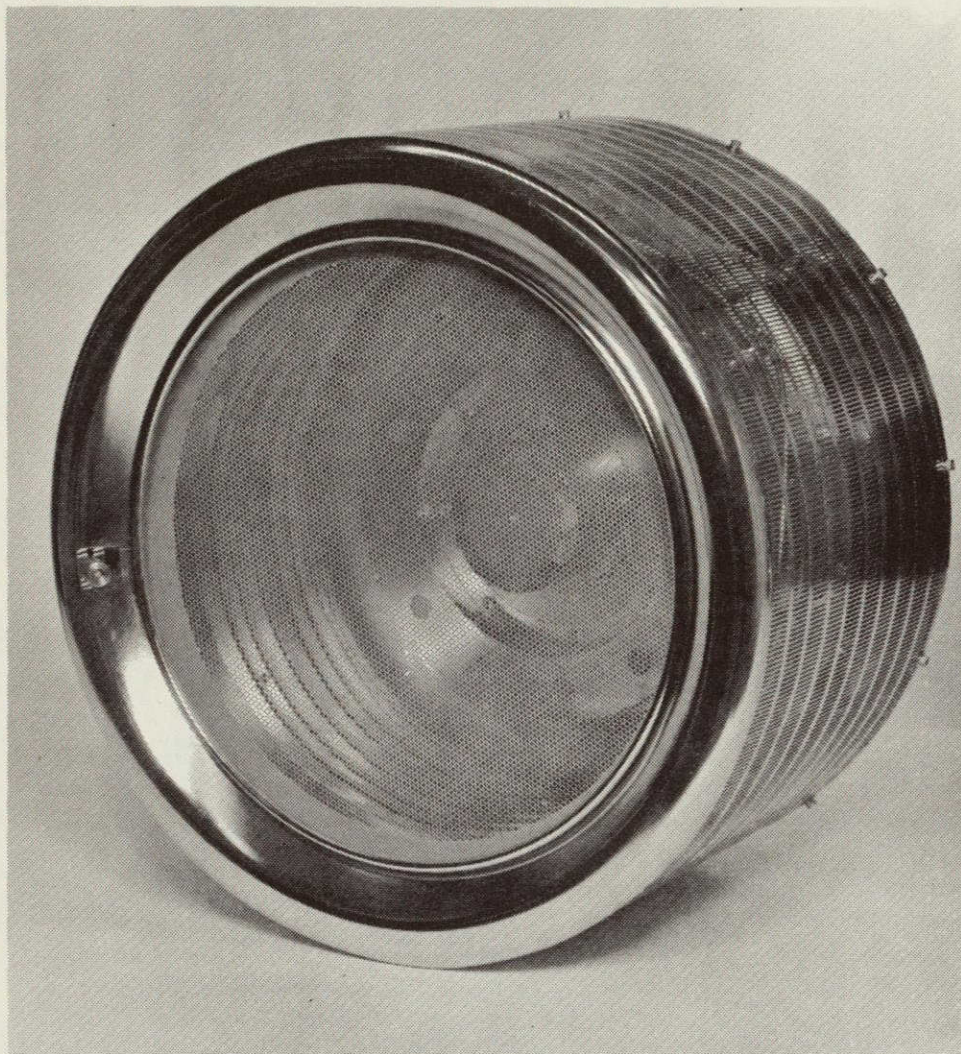


Fig. 54. Task V 30 cm thruster delivered under contract.

M 7055

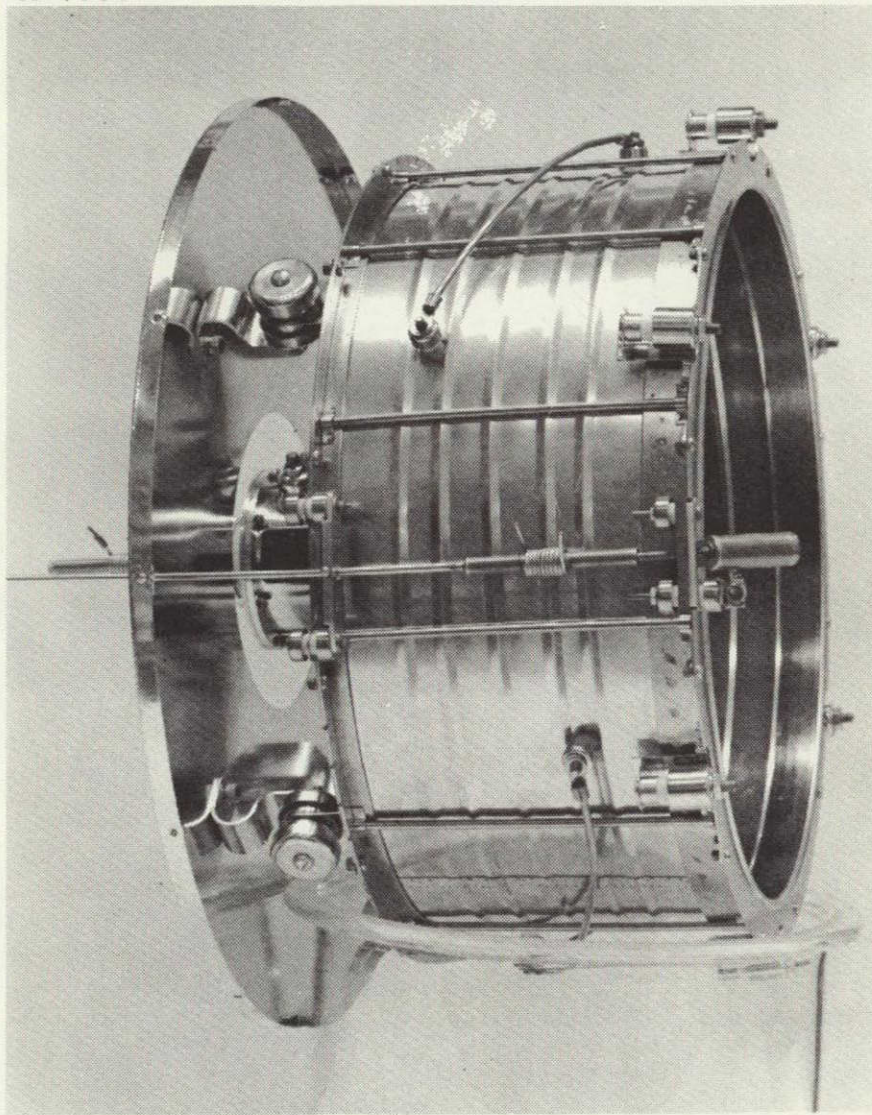


Fig. 55. Task V 30 cm thruster delivered under contract.

TABLE XIII

Specifications for Deliverable Hardware

	High I_{sp} Thruster		Low I_{sp} Thruster	
	Contract Goals	Delivered Hardware	Contract Goals	Delivered Hardware
Over-all diameter, cm	40	40	40	40
Over-all length, cm	—	37.5	—	37
Weight				
Discharge chamber, kg	—	—	—	3.40
Ion optics, kg	—	—	—	0.50
Ground screen, kg	—	—	—	1.60
Total, kg	9.07	6.3	< 9.07	5.50
Beam diameter, cm	—	29	—	29
Beam current, A	1.0	1.0	1.85	1.85
Beam voltage, kV	3.0	3.0	1.0	1.0
Accelerator voltage, kV	2.0	2.0	—	0.4
Effective specific impulse, sec	4650	4500	2750	2847
Total input power, kW	3.5	3.43	2.5	2.4
Power efficiency, %	85	88.1	74	77.1
Mass utilization, %				
Discharge chamber, %	—	—	—	93.4
Total, %	85	88.2	87	90.0

SECTION IV

SUMMARY OF RESULTS AND CONCLUSIONS

This program set out to produce a 2.5 kW mercury ion thruster that would operate efficiently at an effective specific impulse of 2750 sec. These specifications were derived from current mission and system analyses that demonstrate that such a thruster module would be the most useful for a variety of deep space missions of current interest. As a result of these studies the following conclusions may be drawn:

1. The highly efficient discharge chamber design of the SERT-II thruster may be scaled to twice its diameter without loss of efficiency or stability. The addition of an insulated electrode system to such a discharge chamber actually produces a more efficient discharge chamber than the SERT-II unit.
2. It is possible to design both conventional and insulated electrode systems with sufficiently high perveance to extract and focus a 1.85 A ion beam from the above 30 cm discharge chamber at a net accelerating voltage of 1000 V. From the measurements made in this contract it has been demonstrated that the insulated optic has higher perveance and provides more improvement in discharge chamber efficiency than the conventional system.
3. It was believed initially that the primary failure mode of the ion optical system would be due to sputtering damage to the downstream surface by charge exchange ions. Life tests have substantiated the analytical predictions that this type of erosion has been reduced to a value compatible with proposed mission durations. Life tests indicate that the primary failure of the insulated electrode is by local failure of the insulating coating after a few hundred hours of operation. While several mechanisms for this failure may be postulated, none has yet been fully verified. This is an important area for further study.

4. The rapid erosion of early hollow cathodes has been eliminated by a modification of the cathode orifice geometry. Opening the orifice and improving thermal conductivity in this region has permitted the cathode tip to run cooler. No cathode erosion was detectable after 500 hours of operation in the discharge chamber.
5. An electrical isolator has been developed and tested which permits the propellant storage system to be operated at ground potential while the thruster is in operation. The 500 hour life test was conducted in this manner with isolators in both the cathode and main propellant lines. Leakage currents were undetectable on a 10 mA meter throughout the test. No electrical breakdowns in the isolator were observed during any thruster tests.
6. Limited throttling studies were performed to establish the thruster efficiency over a 2:1 power range. These were very encouraging and indicate that more work in this area should produce a thruster with considerable versatility.
7. The thruster performance was sensitive to a number of parameters. A fruitful area for future research is the investigation of the thruster transfer functions and development of a control system to provide for stable operation with the minimum manual adjustment.
8. The final hardware delivered under this contract had the following specifications

Input power	2.4 kW
Electrical efficiency	77.1%
Propellant efficiency	90.0%
Over-all efficiency	69.4%
Effective specific impulse	2846 sec
Net acceleration voltage	1.0 kV
Thrust	0.027 lb.

REFERENCES

1. D. Byers and J. Staggs, J. Spacecraft Rockets 7, 7 (1970).
2. Hughes Research Laboratories Staff, "Discharge Chamber Studies for Mercury Bombardment Thrusters," Final Report, Contract NAS 3-9703, September 1968.
3. North American Rockwell and Hughes Aircraft Company Staffs, "Solar Electric Propulsion Asteroid Belt Mission Study," Final Report, NAS 7-100, January 1970.
4. R. Poeschel, et al., J. Spacecraft Rockets 7, 26 (1970).
5. R.T. Bechtel, "Discharge Optimization of the SERT-II Thruster," NASA TM X52326, 1967; p. 46.
6. J.W. Ward and H.J. King, J. Spacecraft Rockets 5, 1161 (1968).
7. B. Kramer and H.J. King, J. Appl. Phys. 38, 4019 (1967).
8. Hughes Research Laboratories Staff, "Ion Engine Thrust Vector Study," Final Report, Contract JPL 952129, 1969.
9. W.R. Kerslake, private communication.
10. R.L. Poeschel and W. Knauer, "A Variable Magnetic Baffle for Hollow Cathode Thrusters," Hughes Research Laboratories Research Report No. 417, December 1969.
11. R.T. Bechtel, "Performance and Control of a 30 Centimeter Diameter Low Impulse Kaufman Thruster," AIAA Paper No. 69-238, 1969.
12. R.T. Bechtel, G.A. Csiky, and D.C. Byers, "Performance of a 15 cm Diameter, Hollow-Cathode Kaufman Thruster," NASA TMX 52376.
13. D.C. Byers and J.F. Staggs, "SERT II Flight Type Thruster System Performance," AIAA Paper No. 69-235, 1969.
14. W. Knauer, R. L. Poeschel, H.J. King, and J.W. Ward, "Discharge Chamber Studies for Mercury Bombardment Ion Thrusters," NASA CR 72440.

15. V.K. Rawlin and W.R. Kerslake, "Durability of the SERT II Hollow Cathode and Future Applications of Hollow Cathodes, NASA TMX 52532.
16. W. Espe, Materials of High Vacuum Technology, (Pergamon Press, New York, 1966), Vol. 2, p. 114.

APPENDIX

DEVELOPMENT OF ELECTRICALLY INSULATING COATING FOR ION ACCELERATOR GRID

by W.E. Lent

In order to improve the operation of the Kaufman thruster, a high temperature dielectric coating is required on the ion accelerator grid. This coating is required to furnish 2 to 3 kV protection at a maximum operating temperature of 600°C in certain areas. The coating must be strongly bonded to the surface of the perforated molybdenum grid. In addition, the coating should be impervious to mercury plasma and have a smooth surface to minimize corona.

A. DEVELOPMENT OF A GLASS COATING FOR MOLYBDENUM

Initial work on the coating involved development of a glass that would be fused onto molybdenum at a temperature greater than 800°C. It was necessary that this glass have a thermal expansion match close to molybdenum, that it be bubble free, and that it have a high electrical resistivity at the operating temperature. If a voltage breakdown value of 250 V/mil were assumed, the glass coating should give adequate protection at 8 mil thickness. Extensive work was conducted along these guidelines which resulted in basic data for the successful dielectric system.

In the performance of these studies, 54 samples of commercial glasses from Ferro Corporation, Glastex Chemical, and Corning and of HAC's own manufacture were formulated and fired under varying conditions. They matured over a range of temperatures from 1025° to 1775°C. Firing atmospheres were nitrogen, argon, and vacuum in four separate fusion methods.

1. Fusion Methods

a. Strip heating

Strips of molybdenum 1 x 0.01 x 10 cm were coated on one side with each of the candidate glasses. Both ends of each strip were fastened to electrodes

in a bell jar. Firing trials were conducted at temperatures from 800 to 1750°C by passing an electric current through the strips. The effects of nitrogen and vacuum were compared during the tests.

b. Preheated electric furnace

Molybdenum plates 2.5 x 5 x 0.025 cm were coated with the candidate glasses and placed in a quartz tube filled with flowing nitrogen. The coatings were fused by inserting the tube into a preheated globar furnace at 1200 to 1400°C for a short fusion cycle.

c. Electric furnace fusion - long cycle

Molybdenum plates 2.5 x 5 x 0.025 cm were coated with candidate glass on one side and fired from room temperature to 1200 to 1300°C inside an impervious, closed end mullite tube with continuous argon flow. The other end of the tube was sealed to atmosphere remotely from the heating zone and the argon passed in and out of the tube through this seal. Globars around the exterior of the middle of the tube provided the heat source. The argon was allowed to flow during subsequent cooling.

d. Fusion of coatings on molybdenum grids in a gas fired furnace

Both 15 and 30 cm grids were coated on one side with candidate glasses. The grids were placed in sealed cordierite saggers employing alumina powder seals where the saggers joined. An entire sagger assembly was fused from room temperature to 1150 to 1200°C in a gas fired kiln. Argon under pressure was forced into the saggers through mullite tubing which passed through the kiln wall. Argon pressure was measured at the sagger outlet tube to assure positive pressure at all times during firing and cooling.

The first three of these firing methods made it possible to select the best glasses and associated firing technique to coat molybdenum. Unfortunately, neither the 15 nor 30 cm diameter grids could be fired by these methods because of inherent equipment limitations. The fourth method accommodated the large grids but was unsuccessful due to excessive molybdenum oxidation caused primarily by the porosity of the saggers and seals. Consideration of these factors resulted in the observation that firing samples in a sealed sagger to 1200 to 1300°C in a gas kiln is not practical. It was then concluded that a better way would be to put the heater inside a special atmosphere chamber and keep seals as near as possible to room temperature. In order to fire grids up to 30 cm diameter, an induction furnace was designed and constructed with the heating susceptor and sample well insulated and located in the center of a large bell jar. All atmosphere seals on the furnace were maintained close to room temperature. The induction heated susceptor was capable of producing temperatures up to 1700°C. The sequence of furnace operation was as follows:

1. Place the coated cathode on the susceptor and cover with refractory lid.
2. Place the glass dome on its glass base with the joining surfaces vacuum grease coated.
3. Strap down the glass dome with spring loaded nylon web straps.
4. Evacuate the dome with a vacuum roughing pump to > 26 in. Hg.
5. Seal off the pump and bleed in 1.5 in. positive water head.
6. Raise rf power in induction coil until desired fusion temperature is reached. Hold temperature, if required, by regulating rf power.
7. Turn off power and continue to allow argon to flow until dome is cool enough to remove.
8. Turn off argon and remove dome.

This process was ultimately refined to the point that this apparatus could perform a fusion operation on a 15 cm diameter grid at 1100°C and cool to a safe removal temperature in a 2

hour complete cycle. A larger apparatus powered by a 20 kW induction generator was then built for firing 30 cm diameter grids by essentially the same process.

2. Development with Induction Furnace.

The new furnace operated extremely well, providing increased firing speed and decreased oxidation. This necessitated re-evaluation of previously selected glasses and processes under the new conditions. Three parallel studies were made, as described below:

a. Preparation of Molybdenum for Glass Coating

Eight methods for perforated molybdenum surface treatment were investigated using MC-1 glass at 1200°C, for comparison with coatings applied on untreated metal. These methods are described and the results are outlined in Table A-1. The selected method consisted of electropolishing the grid until the corners of the perforations were rounded. The resulting surface to be coated was then lightly sand-blasted to dull the polish.

b. Evaluation of Commercial Glasses

Calculations were made to obtain the expansion coefficients of selected glasses from previous work and of some new commercial glasses. Those considered acceptable had thermal expansion values of 6×10^{-6} /in./in./°C, or less, to approach the value of molybdenum (4×10^{-6} /in./in./°C). Commercial glasses selected were Corning 7052, 7055, O. Hummel 698, Ferro 3249, 3185, 3224, 3225, 3251, 3291, and 3241. All glass coatings were applied with a spray gun to produce dried coatings of two thickness ranges -- 3 to 5 mils and 5 to 7 mils. Samples of each were fired to temperatures of 900, 1000, 1200, and 1400°C for corresponding times at each of these temperatures of 90, 60, 30, and 0 min. Argon at 1.75 in. of water pressure was used for fusion in the induction furnace.

The basic formula used in preparing the coatings was:

	<u>Parts by Weight</u>
Glass Frit (\leq 200 mesh)	70
Enamel Clay	3
Sodium nitrite	0.05
Water to produce a sprayable suspension.	

TABLE A-1

Results of Metal Preparation Studies with MC-1 Glass

Metal Surface Treatment	Single Fired Coat	Thickness, Mils	Two Fired Coats	Thickness, Mils	Three Fired Coats	Thickness, Mils
Untreated	Dark Gray Clear No Bubbles Edge Crawling	3	Med. Gray Clear Few Bubbles Badly Crawled	5.5	Light Gray Slightly Opaque Bubbles No Crawling	9
Dry Bead Blasting	Dark Gray Clear No Bubbles Badly Crawled	2.5	Med. Gray Clear Few Bubbles Badly Crawled	5	Light Gray Slightly Opaque Many Bubble Clusters Slight Crawling	11.5
Wet Bead Blasting	Dark Gray Clear No Bubbles Badly Crawled	5	Med. Gray Clear Few Bubbles Badly Crawling	5.5	Light Gray Slightly Opaque Bubble Clusters Slight Crawling	13
Liquid Honing	Dark Gray Clear No Bubbles Badly Crawled	3	Med. Gray Clear Few Bubbles Slight Crawl	4	Light Gray Slightly Opaque Many Bubbles Slight Crawling	18
Machined Counter-sinking of Perforations	Dark Gray Clear No Bubbles Metallic Areas	2.5	Med. Gray Clear No Bubbles Badly Crawled	5	Light Gray Slightly Opaque Many Bubbles Slight Crawling	20
Electropolishing	Dark Gray Clear No Bubbles Extreme Crawling	4	Med. Gray Clear Few Bubbles Extreme Crawling	9	Light Gray Slightly Opaque Many Bubbles Extremely Crawling	—
Electropolishing followed by Sand Blasting	Dark Gray Clear No Bubbles No Crawling	2.5	Med. Gray Clear Few Bubbles No Crawling	6	Light Gray Slightly Opaque Some Bubbles Very Slight Crawling	10
Electropolishing followed by Oxidation	Dark Gray Clear No Bubbles Slight Crawl	3	Med. Gray Clear Few Bubbles Slight Crawl	4	Light Gray Slightly Opaque Isolated Bubbles No Crawling	10
Electropolishing followed by Etching	Dark Gray Clear No Bubbles Extreme Crawling	4	Med. Gray Clear Few Bubbles Extreme Crawling	7	Light Gray Slightly Opaque Many Bubbles Extreme Crawling	—

The results of firing at 900, 1000, and 1200°C are given in Table A-2. Firing at 1400°C resulted generally in over-fired coatings which, although essentially bubble free, were too thin for grid protection. Coatings MC-4 and 5 (Corning No. 1720 and 7070) did not arrive in time for testing and coating MC-10 burned up at 900°C, eliminating further testing. Therefore, results of these glasses were not reported. It is seen that all of the ten glass coatings were capable of giving good glassy coverage with no apparent thermal mismatch. Each glass gave best results at certain temperatures reported in Table A-3. The best glass frit was Ferro No. 3249 (coating MC-1) fired to 900°C for 30 to 90 min, depending on the mass of the molybdenum. None of the glasses was entirely bubble free. Those that were clearest were also too thin to give adequate protection at 2 kV.

c. Development of Lower Temperature, Low Viscosity Glasses for Molybdenum

It was reasoned that a lower fusion temperature would cause less gas evolution from the molybdenum grid and that a lower melted viscosity would permit bubbles to escape more readily. A glass known to be very viscous, Ferro No. 3249, was selected as the starting formula. This glass contains MgO , CaO , Al_2O_3 , B_2O_3 , and SiO_2 . Systematic studies of variations in the oxide percentages in this system revealed that reducing the SiO_2 content was the most effective means of lowering the viscosity. Continued experiments resulted in the formulation of a new glass with lower viscosity and melting point and a close thermal match to molybdenum. The formula and method of preparation and application of the new glass are discussed at the end of this section.

3. Electrical Tests of Two Selected Glasses

Both MC-1 coating and the coating based on MF-4 glass were applied to 5 cm² perforated molybdenum test samples at various thicknesses, and fired at several temperatures. These were tested electrically for voltage breakdown with the apparatus shown in Fig. A-1.

TABLE A-2

Results of Commercial Glass Evaluation Using the Induction Furnace

Coating Number	Peak Temperature, °C	Time at Temperature, Min	Number of Coats	Type Glass	Results ^a				
					Fired Thickness, Mils	Crawling	Bubbles	Thermal Fit to Molybdenum	Texture
MC-1	900	90	2	Ferro 3249	5	N	N	E	Slightly Underfired
	900	90	3	↓	5	↓	N	↓	G
	1000	60	2		4		F		P
	1000	60	3		7	↓	N	↓	G
	1200	30	2		3	↓	IG	↓	G
MC-2	1200	30	3		7		IG		P
	900	90	2	Corning 7052	6	N	Pits	E	Fa
	900	90	3		20	N	Ext		G
	1000	60	2		11	S	N	↓	G
	1000	60	3		19	N	N		G
MC-3	1200	30	2	↓	7	S	M	↓	Fa
	1200	30	3		16	N	M		Fa
	900	90	2	Corning 7055	7	N	N	E	G
	900	90	3		12	S	F		Fa
	1000	60	2		5	N	N	↓	G
MC-6	1000	60	3	↓	17	N	ML	↓	P
	1200	30	2		9	N	M		G
	1200	30	3		13	N	M		G
	900	90	2	O'Hommel 698	7	N	F	G	G
	900	90	3		11	↓	N	↓	Fa
MC-7	1000	60	2		3		N		G
	1000	60	3	↓	9	↓	N	↓	Fa
	1200	30	2		3	↓	N	↓	VG
	1200	30	3		11		IG		Fa
	900	90	2	Ferro 3185	4	N	M	G	Fa
MC-8	900	90	3		12	↓	F	↓	G
	1000	60	2		3		F		G
	1000	60	3	↓	9	↓	IG	↓	G
	1200	30	2		5	↓	IG	↓	G
	1200	30	3		11		F		Fa
MC-8	1000	60	2	Ferro 3224	4	C	F	G	VP
	1000	60	3		17	C	N	↓	G
	1200	30	2	↓	8	S	M		Fa
	1200	30	3		11	S	F		Fa

$$a_{\text{Key}}$$

E = Excellent

VG = Very good

G = Good

Fa = Fair

P = Poor

VP = Very poor



ML = Many large

Ext = Extreme

IG = Isolated groups

TABLE A-3

Optimum Firing Schedules for Selected
Commercial Glasses on Molybdenum

Coating Number	Commercial Glass Used	Peak Temperature, °C	Time at Peak Temperature, Min
MC-1	Ferro 3249	900	90
MC-2	Corning 7052		
MC-3	Corning 7055		
MC-6	O'Hommel 698		
MC-7	Ferro 3185		
MC-8	Ferro 3224	1200	30
MC-9	Ferro 3225	1000	60
MC-12	Ferro 3241	1000	60
		900	90

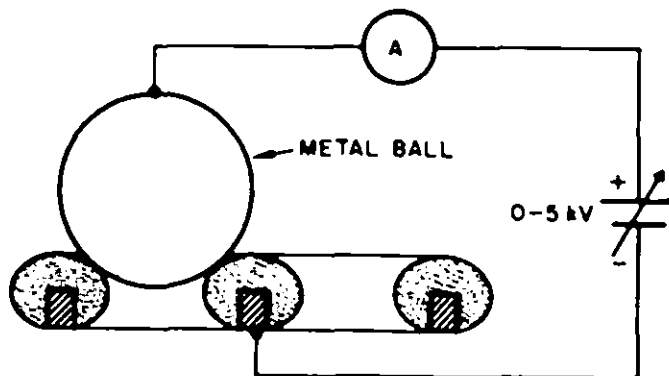


Fig. A-1. Schematic of voltage breakdown test.

It was found that thicker coatings gave the greatest electrical insulation, even though they contained many more bubbles. The most viscous glass, MC-1, at the greatest thickness gave the highest breakdown value of 1.2 kV at 10 mils, or 120 V/mil. It was apparent that at least 18 mil thickness would be necessary for adequate electrical protection. Even the most viscous glasses could not be applied this thick on the 0.63 cm wide webs between the 0.2 cm diameter perforation on 0.288 cm centers. In order to increase the coating thickness, a refractory subcoat was required to act as a supporting, nonflowing framework for subsequent layers of glass. If at least 100 V/mil could be realized with this system, then 20 mils total subcoat and glass thickness would provide the necessary protection. A nonflowing coating system of this type appeared to be a feasible way to attain sufficient thickness on narrow webs between grid perforations.

B. STUDIES OF REFRACTORY COATINGS FOR MOLYBDENUM

Initial trials consisted of 20% of various refractory fillers with 80% of Ferro No. 3249 glass. Mullite, cordierite, calcite, magnorite, alumina, zinc oxide, titania, chrome oxide, barium carbonate, tin oxide, zirconia, and silica were studied as refractory fillers. These materials were fired to 900°C and resulted in general failure as a result of extreme fusion shrinkage cracking. To correct this problem, mullite, as the most promising filler, was again blended with Ferro No. 3249 frit at higher percentages of 50 to 70%. An excellent coating with no fusion cracking and good adherence to molybdenum was

obtained with 70% mullite. Based on these results, the mullite percentage was further increased to allow fusion onto the molybdenum at 1100°C. This higher firing temperature was desirable to assure adherence during subsequent firings of additional glass filler-sealing layers at lower temperatures. In later studies, six other mullites and kyanites were substituted in the formula. These coatings were applied to 1.25 x 2.5 x 0.125 cm solid molybdenum strips. The tests gave higher or perhaps more accurate voltage breakdown values than those on perforated metal. Results are shown in Table A-4. The best refractory coating is MCR-1K1, whose formula is given at the end of this appendix.

C. COATING SYSTEM DEVELOPMENT

1. Study of Coating System Components and Application Sequence

This investigation was concerned with determining the optimum number of coating layers to assure required reliability. The MF-4A coating was selected to melt and fill any remaining pores in the prefired refractory subcoat. MC-1, using Ferro No. 3249 first, was selected as the surface sealant glass. No attempt was made to measure thickness during coating application of any sprayed layer. Each layer consisted of an aqueous slurry sprayed onto the surface until a continuous wet coat was achieved without running. The thickness of each layer was measured after firing. These tests were made on 5 x 5 x 0.63 cm thick perforated molybdenum squares. Voltage breakdown tests were performed using the ball electrode method previously described. Results of these tests are shown in Table A-5.

2. Results and Discussion

The coating system that was developed exceeded the requirements for 2 kV electrical protection. The system is versatile, requiring fewer layers if less protection is needed. Both filler and surface glasses should always be used to prevent mercury plasma diffusion and to minimize surface leakage and corona. It was also found that if an arc-through occurred through an unglazed refractory subcoat, the arcing persisted and the grid was permanently damaged, preventing further use. Arcing through a glazed electrode reduces efficiency, but allows continued operation for a somewhat reduced time. A

TABLE A-4

Effect of Mullite Substitutions in Refractory Subcoating

Type of Material	Subcoat Number	Number of Coats	Voltage Breakdown, kV	Average Voltage Breakdown, kV	Total Dielectric Thickness, Mils	V/Mil	Average, V/Mil
Carborundum Gray Mullite	MCR-1E	1	0.7	1.43	3	230	214
		2	1.3		5	260	
		3	2.3		15	153	
Pryor-Giggey Kyanite	MCR-1F	1	0.6	1.63	2	300	233
		2	1.5		7	214	
		3	2.8		15	186	
Norton Fused Mullite	MCR-1G	1	0.8	2.06	4	200	209
		2	2.1		9.5	220	
		3	3.3		16	207	
Commercial Ores Mullite	MCR-1H	1	0.9	1.67	2.5	360	229
		2	1.4		7	200	
		3	2.7		15	179	
Metco Mullite Powder	MCR-1I	1	0.6	1.53	2	300	253
		2	1.7		5	340	
		3	2.3		19	120	
Virginia Kyanite	MCR-1J	1	0.8	1.63	3.5	228	190
		2	1.5		7	214	
		3	2.5		19	130	
Carborundum Fused White Mullite	MCR-1K	1	0.9	1.96	3	300	297
		2	2.2		7	312	
		3	2.8		10	280	

TABLE A-5

Results of Coating System Study

Coating System Type	Coating Layer Number	Number of Accumulated Layers	Accumulated Fused Thickness, Mils	Voltage Breakdown, kV	Dielectric Strength, V/Mil
Single Refractory Subcoat	MCR-1K1	1	5	0.8	160
	MF-4A	2	5	0.9	180
	(Filler Glass) MC-1	3	8	1.2	150
Two Refractory Subcoats	MCR-1K1	1	5	0.8	160
	MCR-1K1	2	18	1.2	66
	MF-4A	3	18	1.5	84
	MC-1	4	21	1.9	90
Three Refractory Subcoats	MCR-1K1	1	5	0.8	160
	MCR-1K1	2	16	1.0	63
	MCR-1K1	3	24	2.0	84
	MF-4A	4	24	2.2	92
	MC-1	5	26	2.7	104

30 cm diameter grid using the three subcoat layers and glass sealing system was operated for 50 hours at 1750 W of power with no visible effect on the coating.

The spray application method for refractory subcoats also resulted in producing a desirable contour in and around the perforations. The contour is such that the glassed surface extends to the bottom of the perforation from one side, providing protection to the back of the grid. Figure A-2 is a view from the rear of the grid after application and firing of one layer of MCR-1K1. The single layer is starting to coat the inside of the perforation. Three fired layers about 24 mils (at the center of the web) of MCR-1K1 are shown in Fig. A-3. After melting in the filler glass (Fig. A-4) no change in contour or thickness occurs, but porosity is nearly eliminated. Fusion of the surface glass coat produces a glossy high resistivity surface (Fig. A-5). This glass joins with the filler glass to produce an integral continuous glass to the surface of the molybdenum. A cross section of a web protected with two subcoats, filler glass and surface glass, is shown in Fig. A-6. The magnification is 75x, using transmitted light. Note that the coating is smoothly rounded at sharp corners of the web and that there is some glass penetration into a flaw in the metal. Best results are obtained when the top surface of the final subcoat layer is smooth and continuous. Because no movement of a subcoat layer occurs during firing, the freshly sprayed, dried subcoat surface of a grid can be inspected carefully for roughness and continuity. If the sprayed layer on a grid is unacceptable, it may be easily washed off with water, dried, and resprayed. The material is relatively inexpensive, allowing any necessary application adjustments to produce a layer which assures a smooth continuous coat for subsequent hardening. In a separate experiment, coatings of MCR-1K1 were built up on a solid molybdenum surface to 75 mils using 10 individually fired refractory layers and no glass. The top coat was relatively smooth, and the total system showed excellent adherence and no flaking off. Voltage breakdown tests gave a value of 5.6 kV for the total system. Glass fillers and surface glass would have improved this value considerably. This is a significant advantage for future, higher power thruster systems which might require protection up to 10 kV.

M 7049

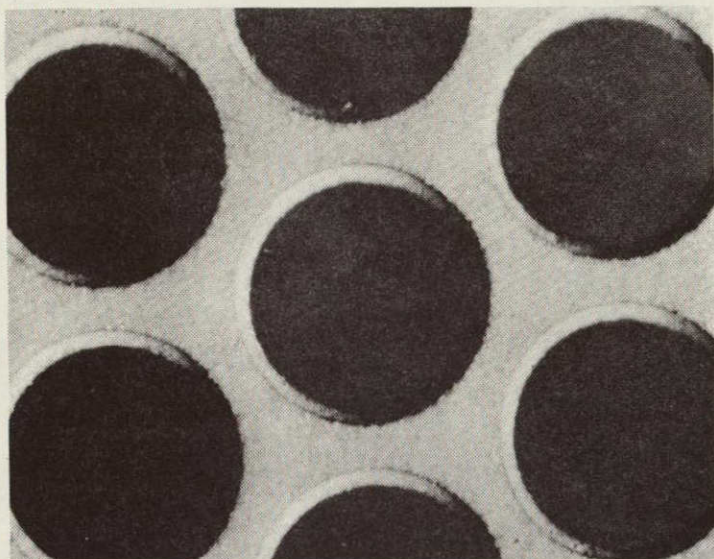


Fig. A-2. One layer of refractory subcoat viewed from back of grid.

M 7050

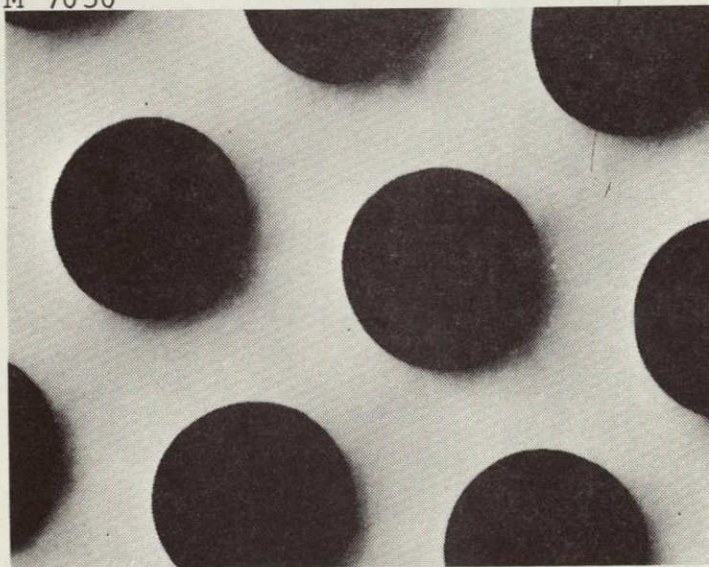


Fig. A-3. Grid coated with three layers of fused refractory subcoat.

M 7051

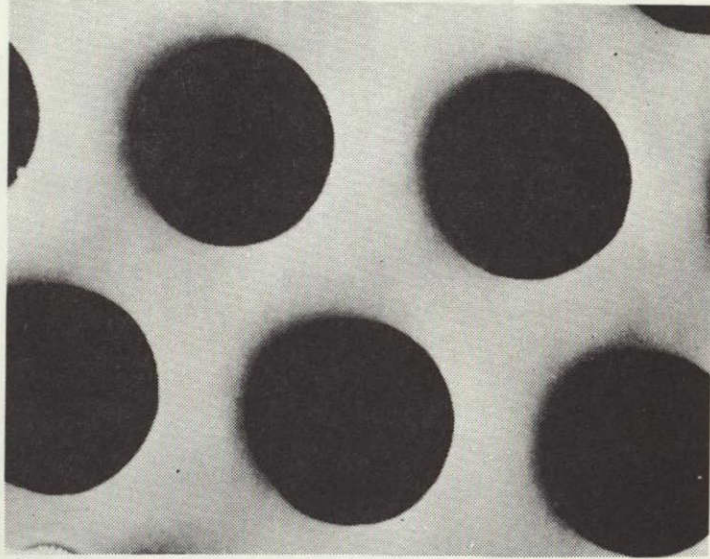


Fig. A-4. Three fired refractory sub-coats after filler glass fusion.

M 7052

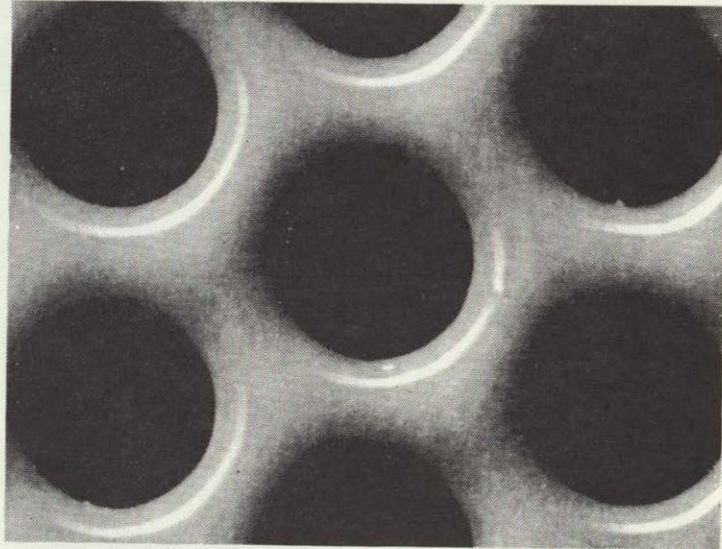


Fig. A-5. Surface of complete coating system after firing of MC-1 surface glass coating.

M7067

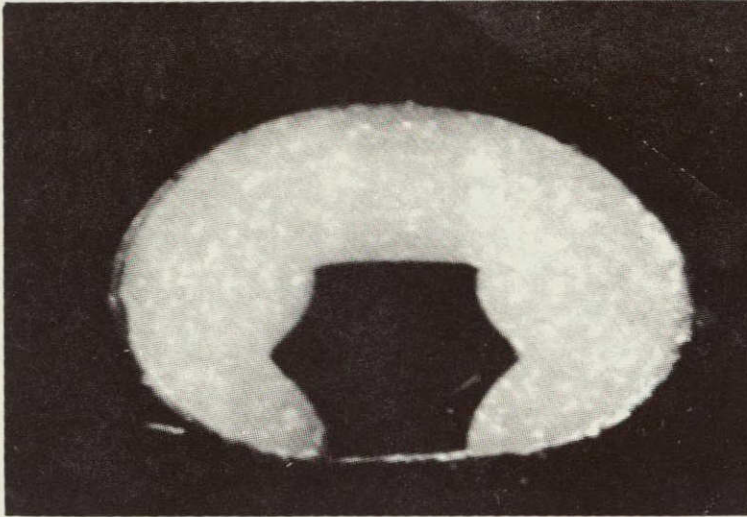


Fig. A-6. Cross section of grid web showing coating system contour.

D. PROCESS FOR ELECTRICAL INSULATING COATING ON MOLYBDENUM

1. Metal Preparation

1. Chemically mill the perforations into the moly-metal disc
2. Power hammer to the desired dished shape
3. Electropolish the surface to be coated
4. Lightly sandblast to dull surface shine
5. Blow surface with high pressure air blast to remove grit
6. Wash disc in Acetone Reagent grade solution
7. Thoroughly rinse with distilled water
8. Dry immediately in drying oven
9. Avoid touching surface of prepared metal until first coat is applied
10. Heat treat at 1150°C for 60 min (repeat 4 through 8).

2. Subcoat Preparation

1. Batch the following formula into a 1 quart porcelain mill containing 2200 g of 1.86 cm diameter alumina stones:

	<u>Grams</u>
Carborundum Co. - 38 F White Fused Mullite	232
Ferro Corporation No. 3249 Frit (200M)	44
Ferro Corporation Green Label Enamel Clay	12
Sodium Nitrite	0.2
Distilled Water	260

2. Grind 8 hours at 90 to 100 rpm
3. Screen slip through 200 mesh screen
4. Store in a glass container with lid
5. Measure specific gravity and viscosity. This should be 1.60 to 1.62 at Zahn No. 2 cap viscosity of 16 to 20 sec. Adjust specific gravity by water content.

3. Application of First Subcoat

1. The MCR-1K1 material is sprayed on the prepared metal surface with a DeVilbiss Model No. D-TGA-501-944F spray gun with a 402F needle and a CU-39-90 air cap. The gun is adjusted and held at a distance from the disc to produce a solid, evenly applied wet coat as the spray traverses the surface in a systematic pattern to produce even coverage. If viscosity of slip is within specified limits, surface tension will prevent closing of the perforations with liquid subcoat.
2. Sprayed disc is air dried in a clean air convection oven at 150°C for 150 min.
3. Careful inspection of dried surface with a low power binocular microscope is performed to evaluate application. Coating must be relatively smooth and free from rough texture because fusion will not change the surface or cause flow. Rough texture is generally caused by too dry spray, dirty spray gun, holding the gun too far from the disc, or by traversing the surface too fast.
4. A sprayed disc with rough areas should be washed with distilled water to remove the coating, dried, and resprayed until an acceptable coating is achieved. Proper thickness of the dried coating should be from 8 to 10 mils, depending on the width of the webs between the holes.

4. Firing of the First Subcoat

1. The acceptable dry coated disc is placed coated side down on a disc of 0.125 x 35 cm diameter molybdenum. This disc has been precoated on both sides with an alumina wash and dried. This coated moly setting plate is placed directly on the 35 cm diameter x 1.86 cm thick graphite susceptor.
2. An insulating brick cover is supported by the refractory sides of the furnace so as to be about 6.3 cm higher than the coated disc.
3. The stainless steel bell jar is placed over the furnace and strapped down with turn buckles.
4. GN_2 is injected into the kiln until 1-1/2 in. water column pressure is obtained on the manometer.
5. Power is applied to the Lepel generator flat copper water cooled coil under the graphite susceptor. Temperature is allowed to rise until 1100°C can be observed on the PT./PT. + 13% RH thermocouple pyrometer placed on the edge of the electrode. This temperature is maintained for 30 min by adjustment of the Lepel output.
6. Power is shut off and the GN_2 is allowed to remain flowing until the temperature reaches a minimum of 200°C. The cover is removed, GN_2 is shut off, and the refractory lid is removed to expose the fused coated specimen.

5. Application and Firing of Second and Third Subcoats

Application of subsequent subcoats is exactly like that of the first coat. Due to the porosity of the first coat, following coats may be thicker (from 8 to 10 mils/layer). This is very desirable as long as surface texture remains relatively smooth. It is desirable to dampen the surface before spraying second or third coats.

After the final coat of mullite is fired, the resultant coating is integral but relatively soft - about the consistency of blackboard chalk. It is possible at this time to ream each aperture with a notched alumina rod held in a hand grinder. This was found to be necessary for coatings more than 0.06 cm thick in order to maintain an acceptable aperture dimension (~ 0.1 cm diameter). When this operation was performed carefully, no damage resulted to the remaining coating.

6. Preparation of Filler Glass

1. Frit (MF-4) - (HAC)

- a. Dry blend the following by tumbling in a glass jar for 4 hours on a roller mill.

	<u>Grams</u>
200 mesh silica	100
(-80M) anhydrous Boric Acid	268.8
Norton No. RA-38-900 alumina	69.2
(-100M MgO (Mollenckredt) dense	63.2
Calcium Carbonate	33.2

- b. Melt the frit in a Denver Fire Clay crucible at 1450°C
- c. Pour molten glass into water to quench
- d. Drain off water and dry frit
- e. Crush to pass 16 mesh screen dry.

2. Filler Glass - MF-4A

- a. Batch the following in a 1 quart porcelain ball mill.

	<u>Grams</u>
MF-4 Frit (-16 mesh)	210
Green label enamel clay	18
Sodium Nitrite	0.3
Distilled Water	50 cc

b. Grind 6 hours at 90 to 100 rpm

c. Screen 200 mesh.

7. Application of Filler Glass

After two (or three) coats of refractory subcoat have been fused onto the disc, spray on a wet coat of MF-4A. This coating may be rough when dried, but will melt during fusion and soak into the subcoat after drying; the glass is brushed off around the edges to expose the disc mounting holes.

8. Firing of Filler Glass

The firing procedure is identical with that for firing a subcoat when sprayed over three layers of subcoat. For a two-layer subcoat system, the temperature should be lowered to 1025°C for 60 min.

9. Preparation of Surface Glass (MC-1)

1. Batch the following in a 1 quart porcelain ball mill

	<u>Grams</u>
Ferro No. 3249 Frit	210
Green label enamel clay	9
Sodium Nitrite	0.15
Distilled Water	135

2. Grind 4 hours at 90 to 100 rpm

3. Screen 200 mesh

10. Application of Surface Glass

Identical to application of filler glass.

11. Firing of Surface Glass

1. The sprayed disc is suspended coated side down, by setting on moly ribbon which contacts the edge only.
2. Firing procedure is identical to the subcoat firings except for the temperature.
 - a. Two subcoat layer systems require 1100°C for 60 min.
 - b. Three subcoat layer systems require 1000°C for 60 min.

12. Removal of Glass from Disc Back

This procedure is performed prior to coating with MC-1 to permit any minor irregularities in the glass to fuse during the final firings. It is repeated if necessary at the conclusion of the coating process.

1. Place the completed disc glass side down on a suitable padded surface. Remove glass on the back by hand (or power) scouring with 100 to 150 grit silicon carbide paper. The contacting paper and backing should be flexible to prevent stress in the disc glass. Light pressure is advisable.
2. Blow away excess grit with high pressure air.
3. Wash in distilled water and dry.

13. Resultant Coating

The coating which results from this method of application appears nearly white, dense and hard. The surface is highly glazed and free from irregularities or imperfections. While small samples have been coated to a thickness of 0.15 cm, a practical maximum thickness for a 30 cm electrode at this time appears to be 0.08 cm.

¹⁷ N70-28290

$$\frac{5}{15} = \frac{1}{3}$$

5081 BSC

Re Installed

REFERENCE BOX 7.E.

CODE	METHOD OF FILLING ORDER
XM	NOT AVAILABLE
RL	REFER TO LIBRARY OF CONGRESS
RG	REFER TO SUPERINTENDENT OF DOCUMENTS
RC	REFER TO COMMERCE DEPARTMENT
XS	REFER TO NATIONAL BUREAU OF STANDARDS
XR	REFER TO OTHER SOURCE

REFERENCE BOX 7.F.

AVAILABLE IN			
PAPER COPY	MICRO- NEGATIVE	BOTH	
A	B	C	NO RESTRICTION
D	E	F	SUBSCRIPTION ONLY
G	H	I	SOLD TO US ADDRESS ONLY
J	K	L	US GOVERNMENT ONLY
		T	AVAILABLE BUT NOT FULLY LEGIBLE
		V	NO STOCK & NOT REPRODUCIBLE
		X	NOT RELEASABLE
		Y	HOLD SALES
		Z	OTHER RESTRICTION

Re-installed
5-15-93

1. CHANGE NO.

2. DATE ISSUED

3. DOCUMENT AFFECTED NO.

4. JOURNAL ISSUE

TITLE

5. AUTHORITY FOR CHANGE ☐ INPUT ☐ DDC ☐ AEC ☐ NASA ☐ ORAL ☐ WRITTEN

6. ISSUED BY

☐ OTHER

NAME:

7. CHANGES

a ☐ DUPLICATE OF:b ☐ SUPERSEDED BY:c ☐ WITHDRAWN FROM NTIS☐ DESTROY DOCUMENT☐ RETURN DOCUMENT & RELATED PAPERS TO:☐ DDC-T ☐d ☐ DISTR/AVAIL CODE:e ☐ FILL FROM PC

MN

f ☐ PUBLIC RELEASABILITYg ☐ OTHER

9. REMARKS

To recipient of this change notice:

NTIS has changed the status of document indicated in box 3.

Please check against your own records to insure agreement.

Any changes in document status should be transmitted to:

Input Section
 National Technical Information Service
 5285 Port Royal Road
 Springfield, Virginia 22151

Telephone 703-321-8517

For explanation of codes in box 7.e. and 7.f. see reverse side.

5 INTERAGENCY

CHANGE IN DOCUMENT STATUS

NTIS-62
(4/71)U. S. DEPARTMENT OF COMMERCE
National Technical Information Service

★ GPO: 1971-425-101